Retrieval Processing System and Performance Analysis for Mesospheric Temperature and Ozone Profiling Based on Solar Occultation Data

Christoph Rehrl

November 2006

Supported by:

Wegener Center
www.wegcenter.at

F F G

The **Wegener Center for Climate and Global Change** combines as an interdisciplinary, internationally oriented research center the competences of the University of Graz in the research area „Climate, Environmental and Global Change". It brings together, in a dedicated building close to the University central campus, research teams and scientists from fields such as geo- and climate physics, meteorology, economics, geography, and regional sciences. At the same time close links exist and are further developed with many cooperation partners, both nationally and internationally. The research interests extend from monitoring, analysis, modeling and prediction of climate and environmental change via climate impact research to the analysis of the human dimensions of these changes, i.e, the role of humans in causing and being effected by climate and environmental change as well as in adaptation and mitigation. The director of the center, hosting about 35 researchers, is the geophysicist Gottfried Kirchengast, the lead partner and deputy director is the economist Karl Steininger. (more informationen at www.wegcenter.at)
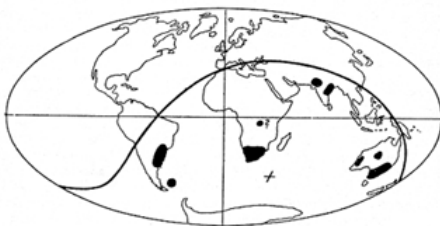
Alfred Wegener (1880-1930), after whom the Wegener Center is named, was founding holder of the University of Graz Geophysics Chair (1924-1930) and was in his work in the fields of geophysics, meteorology, and climatology a brilliant, interdisciplinary thinking and acting scientist and scholar, far ahead of his time with this style. The way of his ground-breaking research on continental drift is a shining role model — his sketch on the relationship of the continents based on traces of an ice age about 300 million years ago (left) as basis for the Wegener Center Logo is thus a continuous encouragement to explore equally innovative scientific ways: *ways emerge in that we go them* (Motto of the Wegener Center).

Wegener Center Verlag • Graz, Austria

Kontakt: Dr. Christoph Rehrl
christoph.rehrl@uni-graz.at

Retrieval Processing System and Performance Analysis for Mesospheric Temperature and Ozone Profiling Based on Solar Occultation Data

Dissertation

zur Erlangung des akademischen Grades

eines Doktors der Naturwissenschaften

vorgelegt von

Mag. Christoph Rehrl

Wegener Zentrum für Klima und Globalen Wandel (WegCenter)
und
Institutsbereich Geophysik, Astrophysik und Meteorologie (IGAM), Institut für Physik,
Karl-Franzens-Universität Graz

Acknowledgments

Abstract

This thesis develops and demonstrates the performance of a realistic forward model and retrieval algorithm for ozone and temperature sounding by the Sun Monitor and Atmospheric Sounder (SMAS) instrument. The SMAS sensor concept employs the solar occultation technique and is primarily aiming at mesospheric profiles. The SMAS sensor provides self calibrating normalised intensity data, which allow to accurately derive profiles of molecular and atomic oxygen, molecular nitrogen, and ozone and temperature.

This work focused on occultation data between 185 nm and 250 nm to compute transmission data for an ozone and temperature retrieval algorithm in the mesosphere. A processing system is presented and used to calculate atmospheric profiles from the solar radiation. This includes a mathematical description of the measurement as well as the retrieval, including the numerical solution of the Abel integral equation. The retrieval was performed with an optimal estimation technique by incorporation of *a priori* (first guess) data. The input for this are simulated measurements (superposed with noise) and *a priori* temperature and density profiles, complemented by statistical models of the uncertainties of the *a priori* and measurement information. The moderately non-linear radiative transfer problem was solved by a Best Linear Unbiased Estimator (BLUE) algorithm, which is an iterative inversion algorithm employing a Taylor series expansion about the first guess profile, and stops after a minimisation in a cost function.

The climatological background model CIRA-86 was used to supply *a priori* temperature and molecular oxygen information, accounting for latitudinal and seasonal variations of the atmosphere. The ozone *a priori* information was derived from AFGL-TR-86 data (FASCODE model). In terms of measurement channels, SMAS comprises a small set of wavelength channels selected to include the ozone and molecular oxygen absorption bands for limb transmissions over the entire mesosphere, providing a maximum possible information from the measurements.

An end-to-end retrieval performance analysis was carried out for the developed retrieval processing system, which was found to yield mesospheric temperature and ozone profiles with < 2 K and $< 5\%$ accuracy, respectively, at ~ 2 km vertical resolution. These very encouraging results for mesospheric temperature and ozone sounding fulfil the target requirements carried out for the SMAS occultation sensor concept. They promise a new quality level of much needed global atmospheric profiling of the mesosphere in the context of climate change monitoring and research.

Zusammenfassung

In dieser Arbeit werden ein realistisches Vorwärtsmodell und ein dazugehöriger Retrieval-Algorithmus für Temperatur- und Ozonbestimmung mit Hilfe eines sogenannten Sun Monitor and Atmospheric Sounder (SMAS) Instrumentes vorgestellt. Das SMAS Sensor Konzept verwendet die Sonnenokkultationsmethode und erzeugt primär Dichte- und Temperaturprofile im Höhenbereich der Mesosphäre. Der SMAS Sensor liefert selbst-kalibrierte normierte Intensitätsdaten, welche mit hoher Genauigkeit in vertikale Höhenprofile für molekularen und atomaren Sauerstoff, molekularen Stickstoff, Ozon und Temperatur umgerechnet werden können.

Für das Ozon- und Temperatur-Retrieval werden in dieser Arbeit primär Intensitätsdaten im Wellenlängenbereich zwischen 185 nm und 250 nm verwendet. Ein zugehöriges Datenverarbeitungssystem zur Berechnung der gewünschten atmosphärischen Dichte- und Temperaturprofile aus diesen solaren Intensitätsdaten wird vorgestellt. Das bedeutet eine mathematische Beschreibung des Messvorganges und Retrievals, inklusive der numerischen Lösung einer Abel-Integralgleichung. Das Retrieval basiert auf der sogenannten "optimal estimation" Technik. Die Input-Daten zur Erzeugung dieser simulierten Messwerte (überlagert mit realistischen Messfehlern) sind sogenannte *a priori* (geschätzte) Temperatur- und Dichteprofile. Diese Daten beinhalten statistische Fehler, sowohl in den *a priori* Profilen als auch in den Messdaten. Das resultierende moderat nicht lineare Strahlungstransferproblem wurde mit Hilfe eines Best Linear Unbiased Estimator (BLUE) iterativen Inversions-Algorithmus gelöst. Dieser basiert auf einer Taylor Reihenentwicklung um das angenommene Startprofil. Der Algorithmus wird abgebrochen, nachdem ein Minimumwert in einer sogenannten Kostenfunktion erreicht wird.

Zur Erzeugung der von der Jahreszeit und geographischen Breite abhängigen *a priori* Temperaturprofile wurde das CIRA-86 Klimamodel verwendet. Die Ozon *a priori* Information wurde aus den AFGL-TR-86 Daten (FASCODE Modell) abgeleitet. Um die maximale Information aus den Messdaten zu erhalten wurden in dieser Simulationsstudie die verwendeten Wellenlängenkanäle so gewählt, dass eine komplette Abdeckung des Absorptionsbereiches von molekularem Sauerstoff und Ozon in der Mesosphäre gegeben ist.

Eine end-to-end Retrieval Analyse wurde durchgeführt, welche Temperatur- und Ozonprofile mit einer Genauigkeit < 2 K beziehungsweise $< 5\%$ bei einer vertikalen Höhenauflösung von ~ 2 km lieferte. Diese sehr ermutigenden Ergebnisse erfüllen zur Gänze die an das SMAS Sensor Konzept gestellten Anforderungen und versprechen eine neue Qualität an globalen mesosphärischen Daten zur Beobachtung und Erforschung von Klimaänderungen.

Abbreviations and Acronyms

ACLISCOPE	Atmosphere and Climate Sensor Constellation Performance Explorer
AFGL	Air Force Geophysics Laboratory
AIM	Aeronomy of Ice in the Mesosphere
ATMOS	Atmospheric Trace Molecular Spectroscopy Experiment
ASA	Austrian Space Agency
BIRA	Belgisch Instituut voor Ruimte-Aëronomie
BLUE	Best Linear Unbiased Estimator
BMVIT	Bundesministerium für Verkehr, Innovation und Technologie
CCD	Charge-Coupled Device
CFC	Chlorofluorocarbons
CHAMP	Challenging Minisatellite Payload (a German satellite mission)
CIRA	Cooperative Institute for Research in the Atmosphere
CNRS	Centre National de la Recherche Scientifique
COSPAR	Committee on Space Research
DARA	Deutsche Agentur für Raumfahrtangelegenheiten
DLR	Deutsches Zentrum für Luft- und Raumfahrt
ECMWF	European Centre for Medium Range Weather Forecast
EGOPS	End-to-end GNSS Occultation Performance Simulator
ENVISAT	Environmental Satellite
ERS	European Remote Sensing Satellite
ESA	European Space Agency
ESL	Expert Support Laboratory
EUV	Extreme Ultraviolet
EUMETSAT	European Organisation for the Exploitation of Meteorological Satellites
FASCODE	Fast Atmospheric Signature Code
FIPM	Frauenhofer Institute for Physical Measurement Techniques
FMI	Finnish Meteorological Institute
GRACE	Gravity Recovery and Climate Experiment
GFZ	Geo Forschungs Zentrum Potsdam
GOME	Global Ozone Monitoring Experiment
GOMOS	Global Ozone Monitoring by Occultation of Stars

GNSS	Global Navigation Satellite System
GPS	Global Positioning System
HCFC	Hydrochlorofluorocarbon
HFC	Hydrofluorocarbon
HRTP	High Resolution Temperature Profiles
IGAM	Institut für Geophysik, Astrophysik und Meteorologie
IASB	Institut d'Aéronomie Spatiale de Belgique
IASI	Infrared Atmospheric Sounding Interferometer
IMK	Institut für Meteorologie und Klimaforschung
ISSA	International Space Station Alpha
LEO	Low Earth Orbit
LIDAR	Light Detection and Ranging
METOP	Meteorological Operational Satellite (of EUMETSAT)
MIPAS	Michelson Interferometer for Passive Atmospheric Sounding
MPIM	Max-Planck-Institut für Meteorologie
MSIS	Mass Spectrometer Incoherent Scatter
MUV	Middle Ultraviolet
NIVR	Nederlands Instituut voor Vliegtuigontwikkeling en Ruimtevaart
NLC	Noctilucent Cloud(s)
ODC	Ozone Depleation Chemical
PI	Principal Investigator
PMC	Polar Mesospheric Cloud(s)
PSC	Polar Stratospheric Cloud(s)
POEM	Polar-Orbit Earth Observation Mission
RO	Radio Occultation
RMS	Root Mean Square
SA	Service d'Aéronomie
SAM	Stratospheric Aerosol Measurement
SATU	Star Acquisition and Tracking Unit
SCIAMACHY	Scanning Imaging Absorption Spectrometer for Atmospheric Chartography
SCOTEP	Standing Committee on the Solar Terrestrial Energy Programme
SFA	Steering Front Assembly
SMAS	Sun Monitor and Atmospheric Sounder
SME	Solar Mesospheric Explorer
SNOE	Student Nitric Oxide Explorer
SOFIE	Solar Occultation for Ice Experiment
SPA	Sun Pointing Assembly
SPOT	Satellite/Systéme Probatoire/Pour l'Observation de la Terre
TIGER	Thermospheric Ionospheric Geospheric Research
UV	Ultraviolet
UVVIS	Ultraviolet and Visible
VFC	Voltage to Frequency Converter
WGS84	World Geodetic System (1984)

Contents

Introduction

The Earth atmosphere as a climate subsystem is an important part of the terrestrial climate system. It is the medium which enables life on Earth and works as transition zone of the Earth's surface to space. A change in the atmospheric composition, especially due to the increasing anthropogenic emissions of greenhouse gases, which are the driving forces in global warming, will influence the thermal structure of Earth's atmosphere. The atmospheric composition is of major importance for the climate system such as for the radiation budget of Earth. Changes in the atmospheric composition are leading to a global change of its climate.

The Earth's atmosphere cannot be seen as an isolated system, in contrary it interacts with the land mass, the ice sheets, and the oceans. The understanding of actual physical and chemical processes of the Earth atmosphere is of crucial importance to daily life and to future conditions of this planet. Observations of the atmospheric state with high quality and long-term stability are fundamental for climate system analysis, especially for atmospheric analysis and modeling.

Important key parameters influencing the climate system are the fundamental atmospheric variables temperature and ozone. Ozone is a critical key constituent of the atmosphere, as well it is influencing the biological system of the Earth. Ozone is a toxic gas in the troposphere but it is the main absorber of solar ultraviolet radiation in the middle atmosphere. The ozone layer protects the Earth and its biosphere from this harmful UV irradiance. Changes in the stratospheric ozone concentration lead to a changing temperature distribution. Decreasing ozone densities lead to lower temperatures and have therefore an impact on the climate system. The ozone concentration is governed by several production and loss processes, some importantly started by man-made chemicals containing chlorofluorocarbons. But not only these parameters drive the climate system, many other processes exists, which are connected with temperature change.

Observations of these key parameters are essential for climate system monitoring. Atmospheric observations can be measured in various ways. Measurements can be made *in situ*, where observations are taken at the exact instrument position, or by remote sensing techniques. Methods which furnishes information from a distance are generally called remote sensing, defined as the acquisition of information of an object, without coming into physical contact with it. This means that the instrument making the measurement is far from the point at which the measurement is being made. Spaceborne sounding for receiving the needed atmospheric information is a subclass of these methods, the solar occultation technique can be used to obtain a part of this necessary information about the Earth atmosphere. And spaceborne sounding holds a very great potential for observing the Earth atmosphere.

The solar occultation technique is basically a Sun-to-satellite limb sounding concept, where the solar intensity in the middle ultraviolet wavelength region (185 nm to 250 nm

band) is monitored in several wavelength channels by a satellite tracking the Sun in limb geometry during occultation by the Earth's atmosphere. A large advantage of this concept is the self-calibrating nature of the Sun Monitor and Atmospheric Sounder (SMAS) occultation sensor concept, whereby the effects of instrument degradation over time can be essentially neglected. These normalised intensity data can be related to the number densities of the absorbing species, and furthermore, to height profiles of atmospheric parameters such as pressure and temperature. Measurements are carried out within an altitude range of about 50 km to 100 km. In a sequential inversion process, starting with a spectral inversion of transmission data to molecular oxygen and ozone columnar content profiles, followed by a spatial inversion via Abelian transform, vertical number density profiles as well as temperature profiles are obtained. The retrieval is accomplished in this work by an optimal estimation retrieval scheme, a so called Best Linear Unbiased Estimator (BLUE). The resulting profiles over low, mid, and high latitudes show errors of less than 5% for ozone, and of less than 2 K for temperature, respectively, for almost all high levels of interest.

In Chapter one, a short overview about the atmospheric composition and structure is given, especially about the thermal structure. This includes an overview of the middle atmosphere as well as a discussion of the ozone properties, its production, and its loss in this altitude region.

Chapter two summarises the basic atmospheric radiative transfer concept, including an overview about the fundamental processes like absorption, emission, and scattering of radiation by gases. Also a short description of the Sun as emitter of radiation and the interaction properties of the Earth's atmosphere is given. The Chapter completes with an overview about the ultraviolet absorption characteristics of molecular oxygen and ozone.

A brief overview about the techniques of remote sensing is given in Chapter three. The solar occultation method, its principle, and its importance for temperature and ozone sounding in the mesosphere is summarised in this Chapter, followed by a discussion about the advantages and disadvantages of the solar occultation method amongst other techniques of remote sensing.

The SMAS sensor concept is discussed in detail in Chapter four. Here the SMAS sensor system is described and information on the scientific promise for such a sensor is given. Due to the accurate fundamental data products as produced by the SMAS experiment, the sensor concept can be an enhancement to other atmospheric sensing missions.

In Chapter five, the determination of the atmospheric parameters on SMAS data is discussed. An end-to-end SMAS data processing system developed in this work is presented and used to calculate atmospheric profiles from solar occultation data. This includes the mathematical description of the measurement, the forward modeling, and the retrieval, including the numerical solution of the Abel integral equation, which furnishes the atmospheric profiles from the columnar measurements. The retrieval was performed with an optimal estimation technique by incorporation of *a priori* data. A brief error statistic study is also included.

In the last Chapter retrieval performance analysis results based on the new processing system for a set of four months (covering the four seasons) and three latitude regions are presented. A concise summary and conclusion Section completes the work.

1   The Atmosphere

The Earth's atmosphere is the medium enabling life on the surface of the planet and, furthermore, the atmosphere acts as the transition zone between Earth and space. Like other planetary atmospheres, the Earth's atmosphere figures centrally in transfers of energy between the Sun and the planet's surface and also from one region of the globe to another. These transfers primarily keep up the thermal equilibrium and determine the planet's climate. The Earth's atmosphere is dynamic, with changes occurring due to changes of solar illumination, season, latitude, and solar activity.

1.1   Composition and Structure of the Atmosphere

The atmosphere is the relatively thin gaseous envelope surrounding the planet. It is held around the Earth by gravitational attraction. This gaseous mixture is nearly uniformly distributed over the Earth's surface. Almost the entire mass of the atmosphere (more than 99%) is found below an altitude of only about 30 km. In spite of its relatively small mass and thickness, the atmosphere is the central component of the climate system. The Earth's temperature results from the balance of solar energy that reaches the Earth and that leaves the planet. Solar radiation which is not reflected by clouds and snow is absorbed by the Earth's surface and the atmosphere. The atmosphere absorbs a major part of the energy emitted by the surface and re-emits a further part of this energy, but at a lower temperature. This heating by the Sun is primarily responsible for the motion of the atmosphere, but it is a more complex process under the influence of rotation.

Solar radiation, clouds, ocean currents, and atmospheric circulation together determine the Earth climate in a complex and chaotic way. In a general view, the atmosphere is divided into lower, middle, and upper regions. The lower part has been studied over many years by meteorological programs. The developments in rocket and satellite techniques in the last decades have led to the investigation of the middle and upper atmosphere. The region which extends from about 10 km to 100 km altitude is generally called the middle atmosphere. Observations of this region are not as advanced as that of the lower and upper atmosphere respectively.

The atmosphere is generally described in terms of layers which are different in thermal structure, pressure, composition, and stability. The layers are characterised by specific vertical temperature gradients and called *spheres*. The boundary between connecting layers is called the *pause*. Starting from the surface, the layers are defined, corresponding to their thermal structure, as the *troposphere*, *stratosphere*, and *mesosphere* . The region located above the mesosphere (from about 90 km upward) is called *thermosphere*, the temperature increases to reach maximum values that are strongly dependent on the level of solar activity. The Earth's atmosphere is primarily a mixture of gases. These gases are

Constituent	Molecular weight	Content (fraction of total molecules)
Nitrogen (N_2)	28.02	0.7808 (75.51% by mass)
Oxygen (O_2)	32.00	0.2095 (23.14% by mass)
Argon (A)	39.95	0.0093 (1.28% by mass)
Water vapor (H_2O)	18.02	0-0.04
Carbon dioxide (CO_2)	44.01	380 ppmv
Ozone (O_3)	48.00	10 ppmv
Neon (Ne)	20.18	18 ppmv
Helium (He)	4.00	5 ppmv
Krypton (Kr)	83.80	0.5 ppmv
Hydrogen (H)	1.01	0-12 ppmv

Table 1.1. Composition of the Earth's atmosphere and summary of the most concentrated and relevant atmospheric gases below 100 km (after [*Salby* (1995)]).

molecular nitrogen (78% of volume), molecular oxygen (21% of volume), and several inert gases (helium, neon, argon, xenon, and krypton), as indicated in Tab. 1.1. The remaining 1% of the atmospheric composition consists of water vapor, carbon dioxide, and ozone, along with other minor constituents.

There are also a number of trace gases, but in relatively small and in most cases highly variable amounts because they are created and destroyed in particular regions. These trace species, like ozone and water vapor, play a key role in the radiative energy balance of the Earth. Gases are produced by chemical processes within the atmosphere, human and biological activities, volcanic exhalation, and radioactive decay. In the same way they are removed from the atmosphere by chemical reactions. The average lifetime of gas molecules can range from seconds to millions of years, depending on their reactivity and the efficiency removal process. The description of the atmosphere is, furthermore, complex because the atmosphere supports a wide spectrum of motions. The important atmospheric gases are listed in Tab. 1.1, arranged according to the amount of their atmospheric occurrence. This chemical composition remains constant up to an altitude of about 100 km (cf., e.g., [*Salby* (1995)]).

Molecular nitrogen and molecular oxygen dominate the total number density of the atmosphere up to 100 km. The global-mean density decreases with altitude approximately exponentially. So the mean molecular weight of air varies little with altitude. This feature is the reason why the three layers up to the *mesopause* are called *homosphere*. The ratios of various gaseous constituents at any level result from molecular diffusion and mixing due to turbulent motions. As the atmosphere reacts like a fluid system, a wide spectrum of motions exist (from eddies of a few meters to circulations having dimensions of the Earth itself). The mobility of these fluid systems makes their description complex. Figure 1.1 shows the mean constituents of the middle atmosphere (in a logarithmic density scale). For the homosphere, turbulent air motions result to a well mixed atmosphere, atmospheric composition tends to be independent of height. In the homosphere the mean free path is short, so the time required for the vertical separation of the heavier and lighter constituents by molecular diffusion is many orders of magnitude longer than the time required for turbulent fluid motions.

Above 100 km and below 500 km the molecular diffusion yields a separation of the
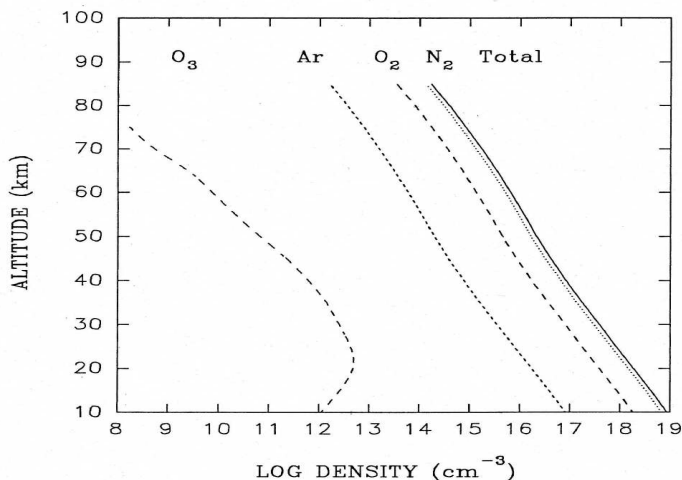
Figure 1.1. Atmospheric composition (adapted from [*Oceanic et al.* (1976)]).

constituents into heavier and lighter ones. The mean molecular weight of air in this region therefore varies with altitude; for this reason the region is known as the *heterosphere*. The density of lighter gases drops off more slowly than that of the heavier gases. The level of transition from turbulent mixing to molecular diffusion is called the *turbopause* (is equivalent to *homopause*).

Fore more details about the atmospheric composition, climate, and atmospheric motions see for instance, [*Salby* (1995), *Peixoto and Ooort* (1992), *Seinfeld and Pandis* (1998)]. This introduction to atmospheric physics is mostly based on [*Salby* (1995)].

1.2 Hydrostatic Equation and Ideal Gas Law

Because of the Earth's gravitational field, the atmosphere exerts a permanent downward force on the Earth's surface. The description of the atmospheric pressure can been seen as a good approximation behaving like the ideal gas law (see, e.g., [*Andrews* (2000)])

$$pV = R^*T = \frac{m}{M}R^*T = mRT \ , \tag{1.1}$$

where p, T, and M denote the pressure, absolute temperature, and molar mass of the gas, m and $n = m/M_m$ correspond to the mass and molar abundance per volume V, respectively. The basic assumption of a perfect gas is, that its constituents have only physical interactions due to brief collisions; molecular forces can be neglected. The ideal gas law corresponds to the equation of state for a pure (single-component) gas. The universal gas constant R^* is recast to the specific gas constant R per unit mass through

$$R = \frac{R^*}{M} \ . \tag{1.2}$$

For a mixture of gases follows from *Dalton's law* the equation of state for the *partial* pressure p_i of the ith component

$$p_i V = m_i R_i T \ , \tag{1.3}$$

5

where R_i is the specific gas constant of the ith component. Dalton's law relates the properties of a mixture with the properties of the individual components. The partial pressure p_i is the contribution to the total pressure of the ith component in isolation at the same volume and temperature as the mixture. Therefore the pressure of a mixture of gases is equal to the sum of their partial pressures $p = \sum_i p_i$, where p is the *total* pressure of the mixture.

The Earth's atmosphere is a fluid and is always in vertical and horizontal motion. The heating by the Sun is the main driving force, but also the rotation of the Earth itself and heterogeneous surface conditions influence this motion. If the atmosphere is considered as a layer above the Earth's surface, gravity and the pressure gradient are the most important forces. The upward force acting on a parcel of air (small vertical accelerations are ignored) is normally very close in balance to the downward force due to the Earth's attracting gravitational field, this results in a decrease of pressure with height. The velocity for vertical transportation of particles reach a maximum of 10 m/s and particles which have sufficient energy can escape from the uppermost atmospheric layer, the so called *exosphere*. The exosphere is extended from an altitude of 500 km upwards. Neglect the atmospheric short scale fluctuations, the Earth atmosphere yield to a hydrostatic equilibrium, which is the balance between upward and downward forces. An ideal equilibrium appears if no vertical motions are observed.

Newton's second law of motion applied to a vertical column of air between a level with pressure p and a level with an infinitesimally higher pressure $p + dp$ produce a balance between the pressure acting on the column and the weight of that column

$$p\, dA - (p + dp)\, dA = \rho g\, dV \ , \tag{1.4}$$

where ρ corresponds to the density and g is the acceleration of gravity. The balance of forces in the vertical direction requires that

$$
\begin{aligned}
-dp &= \rho g\, dz \\
\frac{dp}{dz} &= -\rho g \ .
\end{aligned}
\tag{1.5}
$$

Equation 1.5 is known as the *hydrostatic equation*, which is a very good approximation for the description of variation of atmospheric pressure with height. The atmospheric motion due to vertical displacements of air and their time derivatives are small compared to the forces in Eq. 1.5. So the hydrostatic equation denotes that the pressure at any level is equal to the weight of the atmospheric column of unit cross-sectional area above that level.

If the pressure at height z is $p(z)$, then the equation of state can be converted to the following expression:

$$-\int_{p_0}^{p} dp^{'} = \int_{z_0}^{z} \rho g\, dz^{'} \ . \tag{1.6}$$

Integration from the reference altitude z_0 with pressure p_0 to an altitude z yields to

$$\frac{p}{p_0} = \exp\left[-\int_{z_0}^{z} \rho g\, dz^{'}\right] \ . \tag{1.7}$$

Using the following form of the ideal gas law, equivalent to Eq. 1.1 but not dependent on the dimension of the system,

$$p = \rho R T \ , \tag{1.8}$$
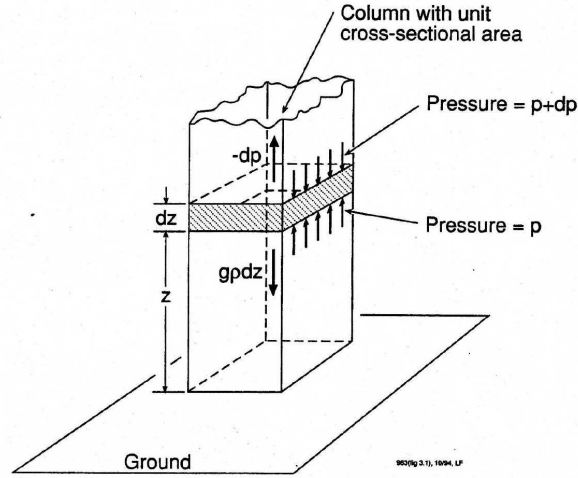
Figure 1.2. Hydrostatic balance for an incremental atmospheric column of unit cross-sectional area dA and height dz, p and $p + dp$ are the isobaric pressures (adapted from [*Wallace and Hobbs* (1977)]).

results to a form for the hydrostatic equation

$$\frac{p}{p_0} = \exp\left[-\int_{z_0}^{z} \frac{dz'}{H(z')}\right] \ , \tag{1.9}$$

where

$$H(z) = \frac{RT(z)}{g} = \frac{kT(z)}{mg} \tag{1.10}$$

is the pressure *scale height* (m is the molecular mass and k is Boltzmann's constant) and p_0 is the surface pressure. The scale height is the height over which the pressure or the concentration falls by a factor e. It represents the characteristic vertical dimension of the mass distribution in the atmosphere and varies from 8 km near the surface to 6 km in the very cold regions of the Earth's atmosphere. The typical profiles of the global-mean pressure and density, both decrease with altitude approximately exponentially are shown in Fig. 1.3. Furthermore, this plot shows the temperature profile of the middle atmosphere. Thus the distribution of any atmospheric constituent can be characterised by its concentration, $n_i(z)$, and also by its scale height $H_i(z)$. Equivalent descriptions can be found as long as the temperature T is a function of height z as well the number densities of the individual species are well mixed. This is not valid for short-lived species like ozone (chemically created and destroyed on short time scales) or water vapor (may occur fast phase transitions). Equation 1.9 can be approximated by an isothermal atmosphere if a constant T,g, and a mean molecular mass with an exponential decrease of pressure is used and we obtain

$$p(z) \approx p(z_0)e^{-(z-z_0)/H} \ . \tag{1.11}$$

The vertical distribution of the total number density can be represented analogously to

7
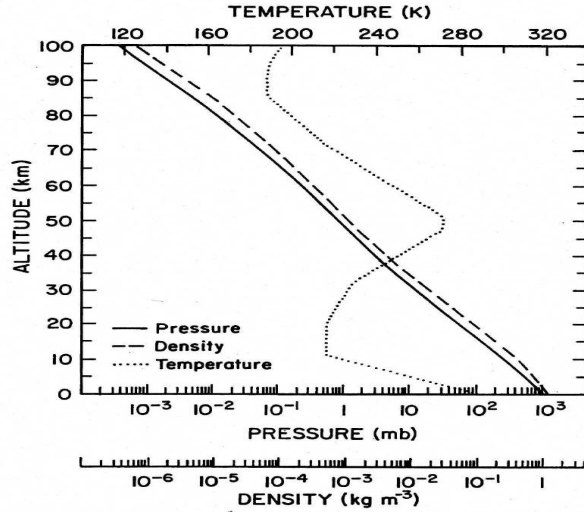
Figure 1.3. Global-mean pressure (solid), density (dashed), and temperature (dotted), as functions of altitude (adapted from [*Oceanic et al.* (1976)]).

the pressure by the following equation:

$$n(z) = n_0 \exp \left[-\int_{z_0}^{z} \frac{dz^{'}}{H(z^{'})} \right] \; , \qquad (1.12)$$

where n_0 is the defined density value at some reference altitude. As shown in Fig. 1.3, pressure and density decrease with about the same rate from the surface. Pressure decreases from $p_0 = 1013$ hPa by a factor of 10 for each 15 km of altitude. Also the mean density decreases with altitude from a surface value of about $\rho_0 = 1.2$ kgm^{-3} at the same rate.

The Earth's atmosphere arranges itself into a vertically layered medium. Therefore horizontal motion keeps the physical properties stable along constant pressure levels on a global scale. These horizontal motions perform over a large scale compared to the atmospheric scale height.

1.3   Thermal Structure

A possible classification of the Earth's atmosphere is its subdivision through its thermal structure, commonly described as a series of several layers, defined by their thermal characteristics. The atmosphere as an envelope of gas surrounding the Earth undergoes many changes as altitude increases.

This thermal structure determines the dynamical properties of individual regions. As noted at the beginning of this Chapter, the several layers are called *spheres* and the boundary between several layers is called *pause*. The simplest description of the atmospheric thermal structure by a vertical profile is summarised in Tab. 1.2.

The troposphere extends from the surface up to the *tropopause* at an approximate altitude of 18 km in the tropics, 12 km at midlatitudes, and 6 km to 8 km near the poles. The temperature and location of the tropopause vary with latitude and season and the

Region	Properties
Troposphere	This layer extends from the surface up to about 8 km to 18 km where the temperature minimum is located and is called tropopause. The temperature decreases with height. A fast vertical mixing is found.
Stratosphere	Here the temperature increases with height up to the stratopause near 50 km altitude. It exists a slow vertical mixing.
Mesosphere	This region extends from the stratopause up to about 80 km to 90 km altitude (mesopause) where the lowest temperature can be observed. The temperature decrease and the vertical mixing is fast.
Thermosphere	The temperature rises continuously from the low value of the mesopause due to absorption of short wavelength (EUV) solar radiation by O_2 and N_2. Strongly dependent on the level of solar activity. A fast vertical mixing exists.
Exosphere	In the exosphere the kinetic temperature has risen to become a constant. The exospheric temperature can be in the range of 500 K to 2000 K. Gas molecules with sufficient energy can escape from the Earth's gravity field.

Table 1.2. Temperature layers of the atmosphere (from [*Huffmann* (1992)]).

mean temperature decrease with increasing altitude. The decrease of temperature is often called the *lapse rate*. The bottom layer of the Earth's atmosphere (which the troposphere represent) exhibits a global-mean lapse rate $-dT/dz$ of about 6.5 Kkm^{-1}. The tropopause is characterised by a sharp change of the lapse rate. The temperature decreases from about 280 K at the surface with an average constant lapse rate up to a minimum at the tropopause (corresponds to a pressure of about 200 mb). This region contains most of the 'weather' and is primarily driven by surface heating. The troposphere contains about 85-90% of the mass of the atmosphere, further this range is characterised by a strong vertical mixing. This layer is often dynamically unstable with fast vertical exchanges of mass and energy being associated with convective activity. In the global scheme of things, the time constant for vertical exchanges is in the order of several weeks. Above the tropopause the stratosphere begins, and the second atmospheric region becomes very stable. The temperature first remains nearly constant and with increasing altitude, the temperature increases (with negative lapse rate) up to a maximum of about 270 K at the level of the *stratopause*, located near 50 km (correspond approximately to 1 mb of pressure). This layer contains about 90% of the atmospheric ozone. The with-height-increasing temperature of the stratosphere reflects ozone heating, which primarily results from the absorption of solar UV radiation by ozone molecules. The stratosphere is dominated by radiative processes and involves only weak vertical motions. The main layers from the Earth's surface upwards are shown in Fig. 1.4.

The region from the stratopause up to its upper limit (the mesopause) of about 85-90 km (corresponds to 0.01 mb) is called the mesosphere. Here the temperature again decreases with altitude up to a minimum of about 190 K, and dynamical instability occurs often. In the mesosphere ozone heating diminishes, convective motions and radiative
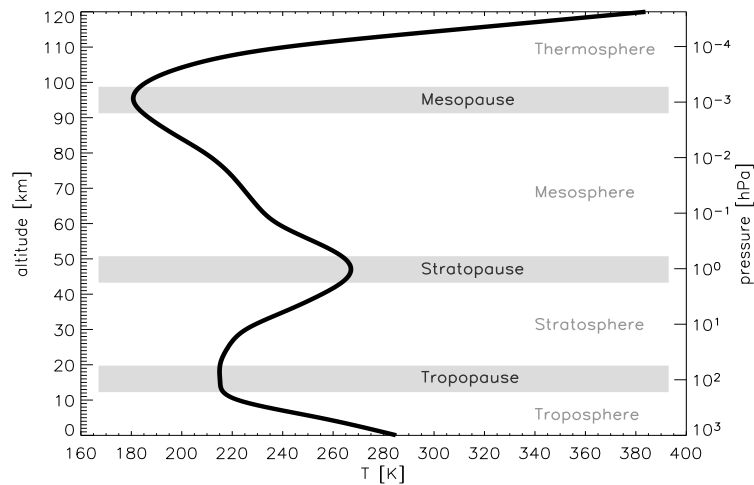
Figure 1.4. Vertical temperature distribution throughout atmospheric layers, such as the troposphere, the stratosphere, the mesosphere, and thermosphere. The temperature gradient changes its sign at the transition from one layer to another (adapted from [*Retscher* (2004)]).

processes are both important in this region and a rapid vertical mixing exists. The region from the tropopause to the mesopause is called the *middle atmosphere*.

Above the mesopause, temperature increases very rapidly with altitude in the so called thermosphere due to absorption of x-ray and extreme-ultraviolet radiation from the Sun. This region is strongly influenced by variations of solar activity and vertical exchanges associated with dynamical mixing become negligible.

1.4 The Middle Atmosphere

Stratosphere and mesosphere are both part of the middle atmosphere, which is commonly marked as the region from the tropopause (8-18 km) to the homopause. The homopause is the level of transition from turbulent mixing to molecular diffusion (approximately at 110 km). In this part of the atmosphere turbulent motions keep the constituents well mixed, ionisation plays only a minor role. Above the middle atmosphere molecular diffusion begins to dominate over eddy mixing, so the constituents become separated vertically according to their molecular masses. The mixing by fluid motions in the middle atmosphere tends to produce uniform mixing ratios for all gaseous constituents of the atmosphere. The primary constituents in the stratosphere and mesosphere (also for the whole middle atmosphere) are diatomic nitrogen N_2 and oxygen O_2. They account together for 98.65% of the total mass of the dry atmosphere. Both gases as well as the noble gases (argon, helium, krypton, neon, and xenon) exhibit long lifetimes against chemical destruction. Minor constituents such as ozone, carbon dioxide, or water vapor playing an important role due to there influence of the transmission of solar and terrestrial radiation in the atmosphere - ozone and carbon dioxide are key parameters of biochemical cycles. Only carbon dioxide is well mixed in most of the middle atmosphere, as opposed to water vapor and ozone; the latter species are highly variable in space and time

The inert gas argon accounts for 1.28%, so less than 0.1% of the total mass are accounted for by a myriad of other species, the so called *trace species* (cf.

10

[*Wallace and Hobbs* (1977)]). Only constituents with significant sources or sinks have spatially and temporally varying mixing ratios, but for the most of these species is the vertical variability much greater than horizontal and temporal variability. The three primary constituents have no significant sources or sinks in the stratosphere and mesosphere, which means that their mass fractions are nearly constant with altitude.

1.4.1 Temperature Distribution and Dynamical Structure

The standard model of the mean temperature profile of the middle atmosphere (including stratosphere and mesosphere) is shown in Fig. 1.4. The mean vertical temperature distribution can be explained in terms of absorption and emission of solar and terrestrial radiation. Water vapor and clouds are the primary infrared emitters and they are responsible for the temperature minimum in the troposphere. The temperature peak in the stratopause is caused by the absorption of solar ultraviolet radiation particularly by ozone (the large amount of ozone is responsible for the large radiative heading rate in the stratosphere) and to a lesser part by molecular oxygen. Radiative cooling is incidental trough infrared emissions associated with the vibrational relaxation of CO_2, water vapor, and ozone. The minimum in the mesopause is caused by the large decrease of the ozone concentration, which reduces the absorption of the solar ultraviolet radiation.
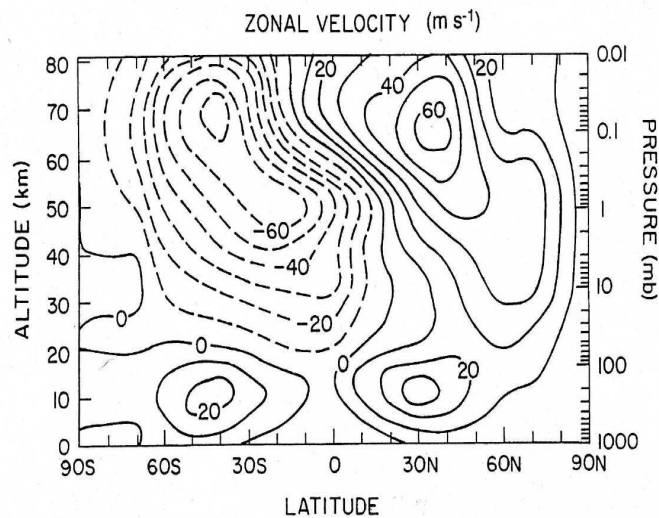
Figure 1.5. Mean zonal wind distribution in the middle atmosphere (adapted from [*Salby* (1995)]).

In the field of atmospheric dynamics it is usual to separate between zonal mean motions and fluctuations about the zonal mean. These fluctuations are called the *eddies* and any such fluctuation can be described in terms of waves. Without such eddy motions, stratosphere and mesosphere would be close to radiative equilibrium at all latitudes. The mean global average temperature at each altitude in the stratosphere and mesosphere is approximately in radiative equilibrium. Eddy motions are responsible for local departures from the equilibrium, especially near the mesopause for both winter and summer, and in the winter stratosphere. As shown in Fig. 1.5, the stratospheric and mesospheric zonal mean flow first weakens with altitude and then intensifies with opposite sign in the two hemispheres. The zonal mean wind is approximately in thermal balance with the

temperature field, thus the vertical part of the wind field is proportional to the meridional temperature gradient [*Fleming et al.* (1988)]. The balance between the net radiative drive (corresponds to the sum of solar heating and infrared heating or cooling) and the heat transport plus local temperature change (produced by eddy motions) is responsible
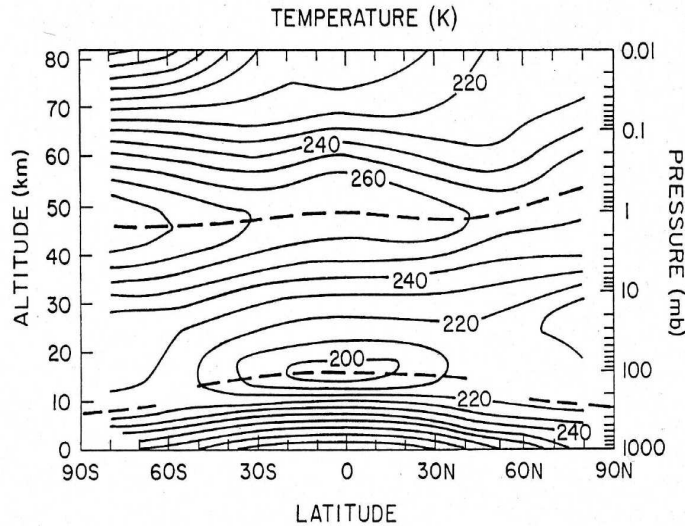
Figure 1.6. Temperature structure during northern winter as function of latitude and altitude (adapted from [*Fleming et al.* (1988)]).

for the overall latitudinally dependent temperature distribution of the stratosphere and mesosphere. These heat transport and the local temperature changes are often called the *dynamical* heating or cooling (cf., [*D.G. Andrews* (1987)]). Figure 1.6 shows the longitudinally averaged solstice mean temperature and Fig. 1.5 shows the to zonal-mean circulation, which is closely related to thermal structure.

The net radiative heating distribution has a strong seasonal dependence. Characteristic for the lower stratosphere in the summer hemisphere is the cold equator and the warmer pole, while for the winter hemisphere a temperature maximum above middle latitudes occurs. The colder region of the stratosphere at the winter pole is highly variable. So the maximum heating is at the summer pole and the maximum cooling at the winter pole. As result exists in the stratosphere a monotonic temperature gradient between the warm summer pole and the cold winter pole. For the equinox is the maximum heating at the equator and cooling at both poles.

The opposite situation is therefore at the mesosphere, where temperature again decreases with altitude. Here the summer pole is cold and the winter pole is warm, therefore the horizontal temperature gradient is reversed. The colder summer pole results by the perpetual daylight and increases steadily to warmest values over the winter pole. The temperature above the winter pole results from the perpetual darkness.

From this differential heating results a circulation in the meridional plane which balances this heating and is often called the *diabetic circulation*. Certainly this circulation is primarily driven by eddy forcing and not by radiative heating directly. The meridional circulation consists of solstice of rising motions near the summer pole. Therefore a meridional drift into the winter hemisphere results, and sinks near the winter pole. Furthermore, the *Coriolis* torque exerted by this drift tends to generate a mean zonal *westerly* flow into

the winter hemisphere and *easterly* flow in the summer hemisphere (approximately in geostrophic balance with the meridional pressure gradient). For the equinox, the radiative drive generates a weak diabetic circulation, rising in the equatorial region, and a pole-ward drift into the spring and autumn hemisphere. For both hemispheres, the Coriolis torque generates a weak mean zonal westerly drift. For more details about the diabatic circulation see, cf., [*Dunkerton* (1978), *Geller* (1983), *Brasseur and Solomon* (1984)].

Compared with a radiative equilibrium distribution (cf. [*Fels et al.* (1980)]), there are a few features of the climatological temperature distribution, which are not qualitatively in accord with the distribution of radiative sources and sinks. The summer polar mesopause is much colder than radiative equilibrium. Further, the winter polar temperatures are above radiative equilibrium throughout the entire middle atmosphere. Therefore, dynamical processes play an essential role for the observed temperature and the zonal wind distributions. Also there exists an evident inter-annual variability in the middle atmosphere (especially in the winter hemisphere).

To produce a stable climatology of the mean zonal temperature distribution (just as for the wind distribution), it is necessary to observe the stratosphere and mesosphere for many years, because there are not sufficient data available. For the stratosphere are only in the last decades adequate observation data available, and for the mesosphere is the data base still unsatisfactory.
For further investigations about the stratosphere and mesosphere see, cf., [*Wallace and Hobbs* (1977), *D.G. Andrews* (1987), *Brasseur and Solomon* (1984)].

1.4.2 Polar Mesospheric Clouds and Climate Change

Polar mesospheric clouds (PMCs), otherwise known as noctilucent clouds (NCLs), form near 82 km altitude at high latitudes during summer in both hemispheres. They form over the summertime polar caps when temperatures fall below 125 K. They occur as thin layers at this altitude, which is close to or at the mesopause. The PMCs can be viewed with naked eye and appear in reflected sunlight against the dark twilight sky. First satellite UV observations of mesospheric clouds were made with the Solar Mesospheric Explorer (SME) [*Thomas* (1984)]. The clouds consists of tiny water ice particles controlled by temperature and humidity, and formed through the microphysical processes of nucleation, condensation, and sedimentation [*Thomas* (1991)].

Mesospheric temperature and humidity respond to changes in carbon dioxide and methane, which are gases that are increasing due to human activity. Increasing levels of those gases lead to a cooler temperature and more water vapor in the mesosphere. These greenhouse gases (such as carbon dioxide and methane) warm the lower atmosphere, but radiate this heat into space in the thin upper atmosphere. As the carbon dioxide level rise a colder upper atmosphere can be expected. The mesopause temperature reaches a seasonal minimum in the summer, when the clouds are brightest. The appearance and brightness of PMCs are well correlated with this seasonal minimum mesopause temperature. Further exists a solar cycle variation dependence. The clouds are only formed about four weeks before and eleven weeks after the summer solstice.

Methane is broken up by solar UV radiation, the released hydrogen atom can react with oxygen to form water vapor. As the methane level rise, more water vapor will be created. Thats the reason why PMCs can be seen more frequently and over larger geographical areas over the past four decades. PCLs are one of the few visible indicators of global change, the number of PCLs sightings has increased by 100% during the last 35 years

[*Gadsen* (1997)]. While these clouds have little effect on Earth's radiation budget, the fact that they are increasing is probably an indicator of long-term global climate change.

More details about PMCs can be found in [*Gadsen and Schroder* (1989)].

1.5   Ozone in the Middle Atmosphere

Ozone is a reactive oxidant gas, naturally produced in trace amounts in the Earth's atmosphere and is important both radiatively and chemically. For this reason the determination of global ozone budgets and related temperature distributions plays a key role for understanding the Earth's climate system and in supporting life at the Earth. Anyway, ozone is one of the ultimate key parameters on global climate. Ozone absorbs the harmful ultraviolet radiation (i.e., UV-B) emitted by the Sun, therefore ozone makes life on Earth's surface possible. This is known since many years, but some of man's activities lead to stratospheric pollution and to a significant reduction in ozone amounts in a few decades. Ozone, which is produced by O_2 photolysis, absorbs solar ultraviolet radiation, which heats the stratosphere and hence affects the atmospheric temperature and is central in the highly coupled chemical, radiative, and dynamical processes of the middle atmosphere. Therefore critical studies of the ozone layer are fundamental aspects of middle atmospheric science.

First observations showed a ozone concentration within a layer between about 20 km to 40 km. Sidney Chapman [*Chapman* (1930)] proposed the first theory for the presence of ozone, he suggested that ozone is formed by UV photolysis of molecular oxygen. But these photochemical mechanism alone deliver a higher ozone mixing ratio than the observed. Paul Crutzen [*Crutzen* (1970)] and H. Johnston [*Johnston* (1971)] recovered in the early 1970s the correlation between odd-nitrogen constituents in determing the balance of ozone in the middle atmosphere.

In 1985 a unexpected strong decline in the ozone density was observed over Antarctica during southern hemisphere winter, first published by [*Farman et al.* (1985)]. Changes of about 50% in total column abundance of ozone during the last decade were found in the lower stratosphere. These so called ozone hole remains for several months with a minimum of column ozone around October. Anyway, the ozone loss can be measured as well in the northern hemisphere. The ozone hole is connected with the chemistry of chlorofluorocarbon, a relatively inert species in the lower atmosphere. Industrially manufactured chlorofluorocarbons become a major threat to the ozone layer.

1.5.1   Ozone Distribution

The ozone layer protects the Earth and its biosphere from harmful UV solar radiation. Atmospheric ozone absorbs solar radiation between 240 nm and 290 nm (UV-C) almost completely and reduces the solar irradiation on Earth between 290 nm and 320 nm (UV-B), which is a strong biologically active wavelength region. A reduction in stratospheric ozone therefore leads to a increasing level in UV-B at the ground (approximately 1% decrease in stratospheric ozone leads to 2% increase in UV-B at the ground). Heating of the middle atmosphere results by absorption of solar UV and visible radiation, and of Earth emitted infrared radiation. These factors contribute to the characteristic temperature profile of the middle atmosphere. Furthermore results the stability of the stratosphere due to the with altitude increasing temperature. Figure 1.7 shows typical vertical profiles of the ozone concentration according to observations at different latitudes.

Most of the total ozone concentration in a vertical column are found at altitudes below 35 km, therefore the principle share of the Earth's atmospheric ozone (about 90%) is found in the stratosphere. The maximum molecular concentration of stratospheric ozone occurs near between 22 km to 25 km, and the maximum mixing ratio (molecules of O_3 /molecules of air) near 35 km, corresponds to a mixing ratio of more than 10 ppm. This follows, since the amount of O_2 availability for reactions with atomic oxygen decreases approximately exponential with increasing altitude. The basic shape in these profiles with a pronounced maximum is a typical characteristic of any gas whose concentration depends on the equilibration between O_2 photolysis (conforms production) driven from the solar irradiation and a gaseous density decreasing with with increasing altitude. This layer is
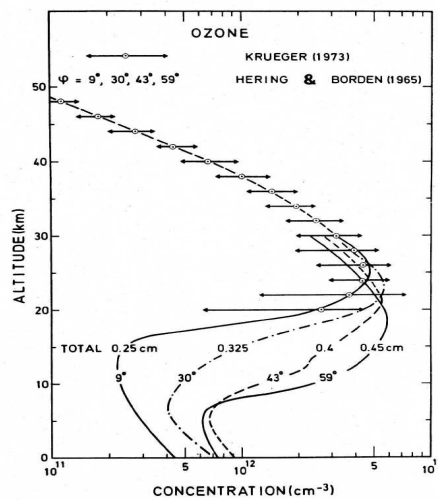
Figure 1.7. The mean vertical distribution of the ozone concentration according to observations at different latitudes, including variations in the total column abundance (adapted from [*Brasseur and Solomon* (1984)]).

sometimes called the *Chapman layer*, and absorbs virtually all of the solar UV radiation of wavelengths between 240 nm and 290 nm. The middle atmosphere temperature profile is the result of the absorption of solar radiation by ozone.

The major part of the ozone production occurs above 30 km, otherwise the observed distribution of the total ozone shows a large molecular concentration below. Not only the local chemical production and loss affects the global ozone distribution, as well as the transport by the meridional, zonal, and vertical winds. A large poleward and downward atmospheric motion in the stratosphere during winter activates these circulation [*Bowman and Krueger* (1985)]. Therefore a strong poleward ozone transport in the stratospheric winter vortex results (possible total ozone amounts up to 500 units in the late winter and early spring - about the definition of a unit see at the end of these Paragraph) in the north polar regions. In the south polar regions are the spring values less than in the northern polar regions. So the time mean and seasonal variability of the total ozone concentration primarily depend on latitude. Thus, the seasonal variation in the stratosphere is dominated by the annual harmonic, there exists a single maximum at most latitudes and heights in the spring.

Further exists in the upper mesosphere a semiannual cycle with a large peak at the

spring equinox, and a secondary maximum at the autumn equinox, and minima at the solstice. The photochemistry alone cannot account for this variability, there must exist a seasonal variability in dynamical processes that influence transport near the mesopause [*D. G. Andrews* (1987)].

The highest ozone column concentration can be found at high latitudes in winter and early spring, the lowest values are located in the tropics. Due to the higher solar irradiation at lower latitudes most of the ozone is produced in this region of the Earth atmosphere, ozone is reallocated from equatorial domain with high ozone production rates to higher latitudes with lower production. Traveling weather systems at the middle and high latitudes also affects the lower stratosphere, so that strong ozone oscillations over a few days can result. In general there is an increase of the total ozone amount from the equator to high latitudes in both hemispheres, but with larger amounts in the northern hemisphere. The relative magnitude of chemical and transport lifetimes shows a significance of transport, approximately lies the time scale for stratospheric ozone deportation at about three month. In general ozone is produced above 25 km, transported to and stored in the middle and lower stratosphere below 25 km, and destroyed at the ground. The depth of the Chapman layer defines the horizontal variation of total ozone, modified by the force of stratospheric transports.

Since the photolysis rate depends on the number of photons reaching the ozone molecules, a diurnal cycle exist. At night when there is no solar radiation the photolysis rate drops to zero. Otherwise the photolysis rates for a given altitude are faster at noontime due to the relatively shorter path lengths than at sunrise or sunset.

The total column density of ozone corresponds to the total amount of O_3 integrated from the surface of the Earth to the top of the atmosphere it is usually expressed in terms of *Dobson units* (DU). One DU is the thickness, measured in units of millimeter, that the ozone column would occupy at standard pressure and temperature (1013 mb and 273 K). The maximum of the total column ozone values ranges from 290 DU to 310 DU over the globe, so the averaged total atmospheric ozone overhead is equivalent to a column at standard pressure and temperature of about 3 mm thickness. The vertical dimension of the ozone layer over the equator (where the tropopause is near 17 km height) is about 250 units and its thickness increases rapidly to about 300 units at midlatitudes (the tropopause drops to about 10-12 km).

1.5.2 Ozone Production and Loss Chemistry

The increase of temperature between the tropopause and the stratopause results by the absorption of solar radiation less than 300 nm through ozone - in the absence of ozone there would be no stratosphere. The first plausible model for the existence and also for the vertical structure was formulated by by the British scientist Sidney Chapman in 1930 [*Chapman* (1930)]. He proposed the continuously production of ozone in the atmosphere by a cycle including molecular oxygen. Since the fifties a multiplicity of additional chemical reactions were introduced, like the presence of mesospheric water vapor, the stratospheric HO_x radicals, of nitrogen compounds, and of chlorine compounds.

The production of ozone involves fast interactions between short wavelength UV from the Sun and molecular oxygen in the upper stratosphere. The so called *Chapman mechanism* starts with the photo-dissociation of molecular oxygen by solar ultraviolet radiation of wavelengths ν less than 242 nm according to the reaction

$$O_2 + h\nu \longrightarrow O + O \tag{1.13}$$

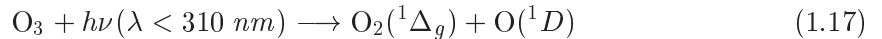$$O + O + M \longrightarrow 2O + M \;, \tag{1.14}$$

where h corresponds to *Planck's constant* and M is another molecule which is needed to carry off excess energy and momentum liberated by the combination of either atomic oxygen. The highly reactive atomic oxygen thus combined with ground-state molecular oxygen forms ozone in the thermolecular reaction

$$O_2 + O + M \longrightarrow O_3 + M \;, \tag{1.15}$$

which is a subsequent recombination reaction between atomic and molecular oxygen in the presence of another molecule M (M is usually another O_2 or N_2 since these two molecules comprise around 99% of the atmosphere). This particular reaction proceeds a very fast rate and it is the only reaction of ozone production in the stratosphere and even the troposphere. Ultraviolet radiation dissociate ozone created by Eq. 1.14, into molecular and atomic oxygen in either their ground state

$$O_3 + h\nu(\lambda > 310 \; nm) \longrightarrow O_2(^3\Sigma_g^-) + O(^3P) \tag{1.16}$$
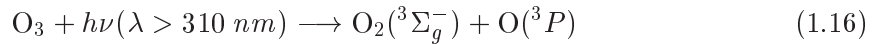
or in their first excited state

$$O_3 + h\nu(\lambda < 310 \; nm) \longrightarrow O_2(^1\Delta_g) + O(^1D) \tag{1.17}$$

in which atomic oxygen almost immediately recombines to new ozone. Additionally, ozone can react with atomic oxygen to generate two molecules of O_2

$$O + O_3 \longrightarrow 2O_2 \;. \tag{1.18}$$

This is the simplest and a very effective way of description the ozone photochemistry. The constituents creep in a closed cycle whereas each reaction above possess different characteristic times and no net loss of components is involved.

Equations 1.15, 1.16, and 1.17 are *fast* reactions (in the order of minutes) and convert O rapidly into O_3, while Eqs. 1.13, 1.14, and 1.18 are *slow*. This means, while O is produced by 1.13 the reactions 1.15, 1.16, and 1.17 cycle many times before reaction 1.18 can take place. So there is a rapid exchange between O_3 and O. The reactions of Eqs. 1.16 and 1.17 does not actually destroy ozone, because O produced by 1.16 and 1.17 recombines almost immediately with O_2 in Eq. 1.15 to produce O_3 again, while large reservoir of O_2 remaining essentially unchanged. The reactions 1.15, 1.16, and 1.17 constitute a closed cycle, so no net loss of the components results. Because reactions 1.15, 1.16, and 1.17 are much faster than reactions 1.13 and 1.18, the O and O_3 species can be considered to be indistinguishable within the timescales of reactions 1.13 and 1.18. Grouping them together leads to the concept of odd oxygen O_x, so called because O and O_3 have odd numbers of oxygen atoms in them. The chemical lifetime of odd oxygen is short compared with that of its individual members or molecular oxygen.

Reaction 1.14 is to slow to be important in the stratosphere, but for the upper mesosphere is it a major reaction. Considering the ozone photolysis, atomic oxygen can be produced in two different forms, the ground state $O(^3P)$ (basically for absorbing radiation greater than 310 nm), or in the first excited state $O(^1D)$ (for wavelengths below 310 nm). Considering the upper part of the middle atmosphere, molecular oxygen photolysis can furnish also $O(^1D)$ atoms in the following way

$$O_2 + h\nu(\lambda < 175.9 \; nm) \longrightarrow O(^1D) + O(^3P) \;, \tag{1.19}$$
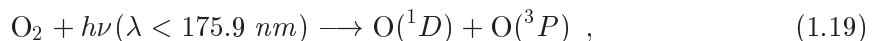
$O(^1D)$ rapidly switch over into the ground state $O(^3P)$ by collision with N_2 or O_2. Both molecules are largely present in the atmosphere, and nearly all $O(^1D)$ ends up as $O(^1P)$.

Recapitulating, the presence of sunlight and energetic photons reaching the upper atmosphere, oxygen molecules were constantly disassociated and freeing oxygen atoms. These atoms react with molecular oxygen on very short timescales and form ozone. So in spite of fast photolysis of ozone, the creation of ozone is fast too. On average the local amount of ozone does not change very strong which can be seen to be in photochemical equilibrium. This steady-state condition is only produced by reaction 1.13 and 1.14 and dissolved by reaction 1.18. The two reactions 1.13 and 1.14 allude to the photolysis of molecular oxygen in the Herzberg continuum at wavelengths between 242 nm to 200 nm, whereas reactions 1.16 and 1.16 show the absorptive acting of ozone in the Hartley and Huggins band near 310 nm. The cycle above shows, that the only result is the absorption of solar radiation, hence ozone absorbs UV radiation very efficiently.

Rates of Production and Destruction of Odd Oxygen

Basically the photolysis rate of the odd oxygen family depends on each of the following parameters, altitude, longitude, season and the time of day. These parameters implicitly depend on the solar zenith angle. The photolysis rate is proportional to the density of the gas (e.g., O_2 and O_3) and the photolysis rate coefficient. In general, the ozone absorption cross sections and the number of incident photons at the necessary wavelengths control the photolysis. For atmospheric investigations a quantitative term of the photodissociation rate of a molecule A is necessary, and given, omitting transport, by

$$\frac{dn(\text{A})}{dt} = -J(\text{A})n(\text{A}) \ , \tag{1.20}$$

where $n(A)$ represents the molecule concentration and $J(A)$ is the photodissociation rate. The inverse of J represent the lifetime of the molecule against photolysis.

Considering the reaction in Eq. 1.18, the destruction rate of ozone follows by

$$\left.\frac{d[\text{O}_3]}{dt}\right|_{-} = -j_3[\text{O}_3] \ , \tag{1.21}$$

responds to a Lagrangian derivative of the ozone number density, j and k accord to the destruction and production coefficients, respectively. From Eq. 1.15 follows the rate of the ozone production, given by

$$\left.\frac{d[\text{O}_3]}{dt}\right|_{+} = k_2[\text{O}_2][\text{O}][\text{M}] \ . \tag{1.22}$$

This allows a description of the net ozone production

$$\left.\frac{d[\text{O}_3]}{dt}\right|_{\pm} = k_2[\text{O}_2][\text{O}][\text{M}] - j_3[\text{O}_3] \ , \tag{1.23}$$

and for the recombination of atomic oxygen and ozone (described by reaction 1.18) follows the production and destruction rate of odd oxygen,

$$j_2[\text{O}_2] = k_3[\text{O}][\text{O}_3] \ . \tag{1.24}$$

Considering the equation above, and again omitting transport, the continuity equation for the odd oxygen family can be written as

$$\frac{d[O_3]}{dt} + j_3[O_3] + k_3[O][O_3] = k_2[O_2][O][M] \ . \tag{1.25}$$

In the state of photochemical equilibrium the continuity equation can be written as

$$j_3[O_3] = k_2[O_2][O][M] \tag{1.26}$$

and for the ratio of the odd oxygen members follows

$$\frac{[O]}{[O_3]} = \frac{j_3}{k_2[O_2][M]} \ . \tag{1.27}$$

With increasing altitude the availability of the third body, i.e. molecular nitrogen or oxygen, decreases, therefore the ratio of atomic oxygen to ozone increases. The consequence is a favored concentration of atomic oxygen at higher reaches of the atmosphere and on the other side ozone at lower heights.

Continuative studies showed a qualitative agreement of the Chapman cycle with the observed vertical ozone profile but the total amount of the ozone number density obtained was too high. Basically is the Chapman mechanism a good approximation to reflect the general shape of the vertical distribution and chemistry of ozone, otherwise these mechanism overestimates the real ozone density in the upper stratosphere, and underestimates ozone in the lower stratosphere, respectively. The mechanism in the Chapman's scheme leads to a ozone destruction rate which is too slow for the amount of destruction required to explain the observed values [*D. G. Andrews* (1987)]. Additional reactions need to be added, especially processes that destroy ozone [*Brasseur et al.* (1999)]. The photodissociation of reservoir species can furnish free radicals, which are able to destroy ozone in a catalytic way. Therefore the direct loss process for odd oxygen, a relatively slow process, can be extended by introducing several catalytic mechanism of the form

$$\begin{aligned} X + O_3 &\longrightarrow XO + O_2 \\ XO + O &\longrightarrow X + O_2 \ , \end{aligned} \tag{1.28}$$

where X denotes the catalyst (accord to a free radical) which does not get consumed in the reaction. This reaction or catalytic cycle go on well even if the abundance of the catalyst is of several orders of magnitude lower than the ozone concentration. Important cycles which contribute in relevant way to the ozone destruction are formed by hydrogen, nitrogen, chlorine, and bromine and become illustrated in the following Paragraph.

HO$_x$ catalytic loss

Hydrogen is transported into the middle atmosphere in form of methane (CH$_4$) and water vapor (H$_2$O) molecules and the free radicals OH and HO$_2$ are produced by photolysis of H$_2$O, H$_2$, and CH$_4$. The height dependence of each of the following cycles results from the variation in concentration of the considered chemical species. This cycle is important to mesospheric ozone (at altitudes above 40 km) and was the first catalytic process to be identified [*Bates and Nicolet* (1950)].

For altitudes above 40 km the reactions that destroy odd oxygen are

$$H + O_3 \longrightarrow OH + O_2$$
$$OH + O \longrightarrow H + O_2$$

(1.29)

and

$$OH + O \longrightarrow H + O_2$$
$$H + O_2 + M \longrightarrow HO_2 + M$$
$$HO_2 + O \longrightarrow OH + O_2 \ ,$$

(1.30)
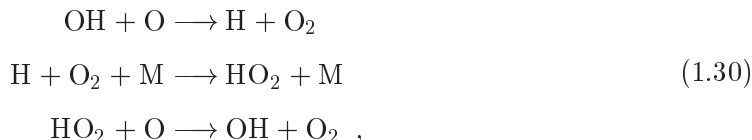
whereby two odd oxygens transfered into an even oxygen. Below about 40 km the ratio of [O] to [O_3] decrease and for this atmospheric region follows

$$OH + O_3 \longrightarrow HO_2 + O_2$$
$$HO_2 + O \longrightarrow OH + O_2 \ .$$

(1.31)

Below about 30 km no atomic oxygen is involved in the reaction and the major catalytic cycle is of following form

$$OH + O_3 \longrightarrow HO_2 + O_2$$
$$HO_2 + O_3 \longrightarrow OH + 2O_2 \ .$$

(1.32)

NO_x catalytic loss

The loss of odd oxygen can occur through catalytic cycles involving nitrogen species in the form of reactive nitrogen, denoted by NO_x, includes nitric oxide (NO) and nitrogen dioxide (NO_2). The main source of middle atmospheric NO_x species is the photolysis of nitrous oxide. Nitrous oxide is produced by natural sources, like living organisms as well as industrial processes. The role played by NO_x was identified around 1970 by P.J. Crutzen [*Crutzen* (1970)] and J.E. Johnston [*Johnston* (1971)].

Two main catalytic cycles exist by which NO_x may participate in the destruction of ozone. The first one is given by

$$NO + O_3 \longrightarrow NO_2 + O_2$$
$$NO_2 + O \longrightarrow NO + O_2 \ ,$$

(1.33)

which is the dominant nitrogen cycle in the middle atmosphere. This cycle is able to destroy a multiplicity of ozone molecules by one nitric oxide due to the un-change of NO and NO_2 in this closed cycle. The second cycle is of major importance in the lower stratosphere with a higher ozone abundance and ozone gets destroyed via

$$NO + O_3 \longrightarrow NO_2 + O_2$$
$$NO_2 + O_3 \longrightarrow NO_3 + O_2$$
$$NO_3 + h\nu \longrightarrow NO + O_2 \ .$$

(1.34)
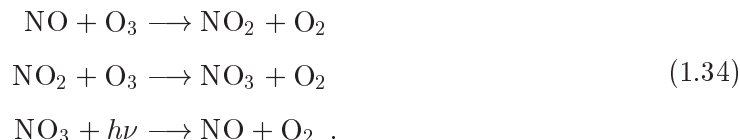
In the same way as we denoted the odd oxygen family, a family of chemicals forming odd nitrogen NO_x can be designed which reacts with other families like odd oxygen or odd chlorine.

20

Cl$_x$ catalytic reactions

Since the development of chlorofluorocarbons (CFCs) in the 1930s, chlorine has played an increasingly important role in determining the ozone concentration in the middle atmosphere. Catalytic cycles involving chlorine are the third recovered processes in ozone destruction [*Molina and Rowland* (1974)]. Naturally reactive chlorine is produced by destruction of methyl chlorine CH$_3$ due to photolysis and by reaction with OH radicals. The amount of the natural source of chlorine accounts for about 15% of the present atmospheric chlorine concentration, the residual contribution originates from man made sources. The CFC gases are photodissociated in the stratosphere and form the highly reactive chlorine radical Cl.

The CFCs photodissociate by

$$CFCl_3 + h\nu \longrightarrow CFCl_2 + Cl$$
$$CF_2Cl_2 + h\nu \longrightarrow CF_2Cl + Cl$$

(1.35)
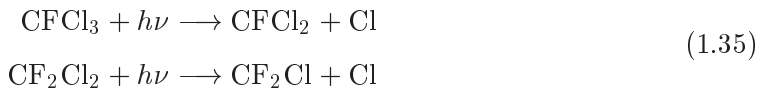
and release active chlorine. This radical is able to destroy several ozone molecules on a small time scale due to its highly reactive character. The principal chlorine catalytic cycle destroying ozone in the middle atmosphere is given by

$$Cl + O_3 \longrightarrow ClO + O_2$$
$$ClO + O \longrightarrow Cl + O_2 \ .$$

(1.36)

Reactions with other species in varying time scales are forming the odd chlorine Cl$_x$ family. Odd chlorine is able to interact with odd nitrogen, this combination has a high potential of atmospheric ozone decomposition.

Br$_x$ catalytic reactions

The fourth cycle with high potential for ozone depletion includes bromine which and shows a reaction cycle similar to chlorine. Bromine accounts for significant ozone loss (about 20-40%) inside the Antarctic ozone hole. The sources of bromine are both, anthropogenic and natural. Reactive bromine exists in form of bromine (Br) and bromine monoxide (BrO). Bromine species like Br and BrO have not a stable reservoir, because they are very easily photolysed, even by visible light, and hence have very short lifetimes. Therefore, bromine is more efficient in ozone destruction than chlorine. The major reactions are given by

$$BrO + ClO \longrightarrow Br + Cl + O_2$$
$$Br + O_3 \longrightarrow BrO + O_2$$
$$Cl + O_3 \longrightarrow ClO + O_2 \ .$$

(1.37)
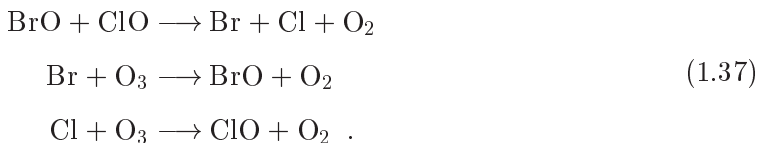
Due to coupling of the chlorine and bromine cycles the effectiveness in ozone destruction enhance up to about 50 times more than chlorine.

1.5.3 The Ozone Hole

The chlorofluorocarbons (CFCs) are a family of chemical compounds developed back in the 1930's as safe, non-toxic, non-flammable alternative to dangerous substances for purposes of refrigeration and spray can propellants. By the early 1970s CFCs become the omnipresent trace gases in the lower atmosphere. The CFCs have a lifetime in the atmosphere on the order of 100 years. With the Montreal Protocol that Deplete the Ozone Layer in 1987, CFCs were eliminated from the market and replaced by hydrofluorocarbons (HFCs) and hydrochlorofluorocarbons (HCFCs). One of the elements that make up CFCs is chlorine. The ultraviolet radiation breaks down CFCs, freeing the chlorine. Under the proper conditions, this chlorine has the potential to destroy large amounts of ozone. This has indeed been observed, especially over Antarctica. As a consequence, levels of genetically harmful ultraviolet radiation have increased.

The destruction of ozone is accelerated by certain trace gases containing nitrogen, hydrogen, bromine, and chlorine. These are referred to as ozone depletion chemicals (ODCs). The most commonly known ozone depletion chemicals are the CFCs. Over the last 30 years man-made CFCs have been the main cause of stratospheric ozone depletion. CFCs however, are not the only ozone-depleting chemicals. Other ODCs include the methylhalides, carbon tetrachloride (CCl4), carbon tetrafluoride (CF4), and the halons which contain bromine instead of chlorine. Such compounds are called halocarbons.

In the mid 1970s Molina and Rowland showed that man-made CFCs have no sink in the troposphere and due to their stabile composition diffuse nearby unchanged to the middle atmosphere, where they photolyse and free chlorine radicals [*Rowland and Molina* (1975), *Molina and Rowland* (1974)]. By means of early model results, a moderate decrease of the ozone concentration with the increased use of man-made chemical was expected. However, in 1985 an unexpected decrease in ozone was discovered over Antarctic during austral spring [*Farman et al.* (1985)]. Changes of about 50% of the total ozone density during the last decade were found to occur in the lower stratosphere, but only in during the spring season. These spring depletion of ozone over Antarctica came to be known as the *ozone hole*.

During winter near the poles a circumpolar vortex (called the polar vortex) builds up due to Earth's rotation and poleward flux of air. Due to the lack of solar heating in winter, very low temperatures can be observed (below 190 K). The vortex in the southern polar region is approximately zonal and much more stable compared to that in the northern polar region. The strong zonal circulation isolates the stratospheric air inside the vortex from the outside air. As a consequence the chlorine chemistry can occur in near isolation. Thus, the ozone hole can expend over a large portion of the vortex. The northern polar vortex often breaks down through planetary wave activity, therefore the temperature do not reach values which increase the formation of aerosols and their associated large scale ozone destruction.

2 Atmospheric Radiation

Atmospheric radiation as one of the building block subjects of the atmospheric sciences, linking the fields of chemistry, aerosol and cloud physics, thermodynamics to global climate and climate change. The interactions between radiation and the atmosphere determine the distribution of radiant energy on all scales. This provides the fundamental understanding of the radiative forcing of climate, for example, and significant advances of understanding of this forcing have emerged over the last few years. Equally forms a fundamental understanding of atmospheric radiation the basis for most of the remote sensing methods currently used to observe the atmosphere. Remote sensing has also become a tool in climate research over the last few years with the application of satellite data in studies of fundamental climate processes.

2.1 Solar Radiation

Basically the Sun is the emitter of all the energy that reaches the Earth. The absorption and processing of this radiant energy by the Earth and its atmosphere are fundamental for the Earth's climate, both at a global and local scale. The atmosphere plays a very important role in the energy balance of the Earth, atmospheric absorption of solar radiation is a relevant and important driving force. A part of the incoming solar radiation is absorbed, scattered, and reflected by various atmospheric gases, aerosols, and clouds, the residual part is absorbed by the Earth's surface. Only a small part is reflected by the surface. Therefore the atmosphere controls the amount of solar radiation that actually reaches the surface of the Earth and further controls the amount of outgoing terrestrial radiation that escapes into space. This outgoing radiation results from the fact that all bodies having a temperature above absolute zero emit radiant energy over a wide range of wavelengths.

The averaged temperature on Earth is almost constant, therefore the system Earth-atmosphere is approximately in thermal equilibrium and the net energy must vanish. So the amount of the absorption of solar radiation must be balanced by emission to space from the planet's surface and atmosphere of terrestrial radiation. The absorption of the solar radiation is concentrated in the visible region of the electromagnetic spectrum and is called the *short wave* radiation. On the other hand the terrestrial radiation is concentrated in the infrared (IR), called *long wave* radiation. Absorption and scattering by various constituents of the atmosphere affect the solar radiation. Radiation absorbed by the atmosphere is directly added to the heat budget, the scattered radiation is partly returned to space and partly continues its path through the atmosphere, where it is again scattered and absorbed. For the climate system the ultraviolet, visible, and near infrared regions are the most important regions of the electromagnetic spectrum.

2.1.1 The Structure of the Sun

The physical and chemical structure of the solar atmosphere determines strongly the production of solar radiation. The atmosphere of the Sun and most of its interior are made mostly of hydrogen and helium. Hydrogen constitutes 73% of the atmospheric mass, while helium constitutes 25%, leaving only 2% for heavier elements including oxygen, carbon, nitrogen, neon, iron, silicon, magnesium, sulfur, and calcium. For both, atmosphere and interior, hydrogen averages at 70.5%, helium at 27.5%, and all other elements at 2%. The Sun is a gaseous sphere and the gas, made of the elements mentioned above, is either neutral or ionised depending on the atmospheric parameters at different locations.

The nuclear chain reaction in the core of the Sun, which steady converts four hydrogen atoms into one helium atom, is responsible for the solar temperature. The amount of energy released in nuclear fusion causes a reduction of the Sun's mass. It is estimated that only 5% of the Sun's total mass has been converted from hydrogen to helium in its lifetime thus far. The temperature of the Sun decreases from a central value of about 8×10^6 K to about 5800 K at the surface. The density within the Sun falls off very rapidly with increasing distance from the center. The central density is about 160 gcm^{-3}, and at the surface, it is about 10^{-7} gcm^{-3}. The average density is about 1.4 gcm^{-3} and approximately 90% of the Sun's mass is contained in the inner half of its radius. A schematic diagram of the solar interior and atmosphere is shown in Fig. 2.1.

Due to the extremely high temperatures in the core region of the Sun, collisions between atoms are sufficiently violent to eject electrons from their orbits. Only the tightly bound inner electrons of heavy atoms will be retained. The photons emitted by nuclear fusion can pass through the inner part of the Sun without being absorbed by the electrons. Closer to the surface, the temperature decreases and the heavier atoms such as iron begin to recapture their outer electrons. These outer electrons are relatively weak bounded to the nucleons and can be easily separated by absorption of photons. Therefore, the flow of photons coming from the interior region is blocked by the availability of the absorbing atoms, a sharply drop of the temperature at some depth below the surface results. Thus, a layer of relatively cool gas covers the hotter interior and the consequence is a heating of the gas at the bottom of the cool outer layer by the hot gas in the interior. The result of that heating is a strong large-scale upward and downward movement of gases in the so called *convection zone*, which extends from a depth of about 1.5×10^6 km to the surface of the Sun. It is believed, however, that energy is transferred to the outer convective layers mainly by electromagnetic radiation, undergoing a series of absorption and emission processes. Near the surface the energy is transported partly by convection and partly by electromagnetic radiation. This results because of the substantial blocking of radiant energy by the absorption of heavier components near the surface. Above the surface, energy is again transferred by means of electromagnetic radiation. The solar output provides electromagnetic, particle, and plasma energy to the Earth as shown in Tab. 2.1. It is a fact that the electromagnetic radiation is by far the largest solar energy source for the Earth and hence the mostly influential for its weather and climate processes.

The boundary between the atmosphere and the interior of the Sun is a region about 1000 km thick, called the *photosphere*. This layer is relatively thin compared to the Sun's radius. Most of the radiation that reaches the Earth's atmosphere is emitted in the photosphere and is further responsible for the visible band in the solar radiation. The existence of the photosphere is due to a drop in the *opacity* of the gas in this region. A gas is called opaque when propagating photons can only move short distances before being
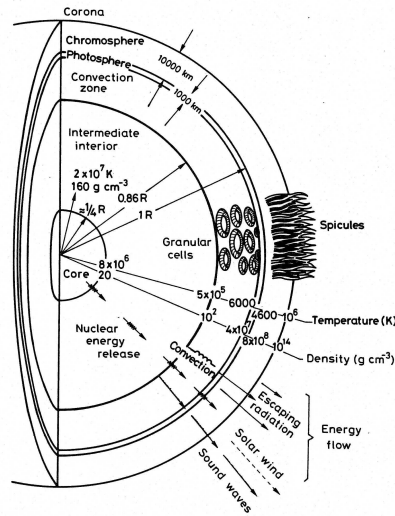
Figure 2.1. A cross section of the Sun illustrating the solar interior and atmosphere. The solar interior includes the core with a temperature of 8×10^6 K, the radiation zone, and the convective zone. The solar atmosphere includes the photosphere, the chromosphere, and the corona. Adapted from [*Brasseur and Solomon* (1984)].

deflected. As a result of these many scatterings a modification and randomisation of the average wavelength of the radiation follows, associated directly to the temperature of the gas. Transparent gas represents the opposite situation: scattering and absorption occurs seldom, the light can propagate over large distances without deflection. While the interior of the Sun is opaque, its atmosphere is largely transparent. The transition between opaque and transparent layers is what defines the 'surface' of the Sun. The capacity of the gas to scatter radiation drastically dimmish at the base of the photosphere.

The solar spectrum is approximately that of a black body (see further Section 2.1.2) at the temperature of 5800 K, this corresponds to the temperature of the gas at the base of the photosphere. The light originated at the Sun's interior is scattered many times below the photosphere, but from the base of this layer upward it is almost free to travel without deflection, therefore the spectrum keeps almost unchanged. The gas becomes colder with increasing altitude, the temperature actually drops to about 4200 K. The emission of the photosphere is a continuum, but as light passes through the transparent and colder gas of the upper photosphere, dark lines appear in the solar spectrum. A set of several hundred dark lines in the bright background of the continuous solar spectrum results. This phenomena was first observed by Fraunhofer in the early 19th century and these lines are called *Fraunhofer lines*. The dark lines correspond to specific wavelengths (according to the atomic transition frequencies) at which the various elements absorb and reemit the light passing through the gas in the Sun's outer atmosphere, where the temperature is as low as 4000 K to 5000 K (see, e.g., [*White* (1970)]).

The photosphere is far from being a homogeneous surface, characterised by a uniform distribution of granules over the solar disk. The granules are regions 1500 km wide on average and they have lifetimes of 5-10 min, and are observable in visible light. At the center of a granule the temperature of the photosphere is few hundreds Kelvin degrees higher than at its edge. Granulation is due to the convection operating below the photosphere, the granules are simple bubbles of hotter gas coming from the interior and results

25

probably by strong convective processes in and below the photosphere. In these columns hot gas rises with a velocity of several kilometers per second (this can be confirmed by Doppler shift measurements [*Bray et al.* (1984)]). The hot gas then cools at the top of the column and sinks down in the darker regions surrounding each granule. Thus, granulation just represents the tops of convection currents that are transferring heat from below the solar surface to the surface.

Source	Energy (Wm^2)	Solar cycle change (Wm^2)	Terrestrial deposition altitude
Solar radiation			
Total irradiance	1366	1.3	Surface, troposphere
UV 2000-3000 Å	15.4	0.16	0-50 km
UV 0-2000 Å	0.15	0.15	50-500 km
Particles			
Solar Protons	0.002		30-90 km
Cosmic rays	0.000007		0-90 km
Solar wind	0.0003		About 500 km

Table 2.1. Magnitude and variability of the solar sources of terrestrial energy. Data taken from [*Council* (1994)].

Furthermore, transient phenomena such as *sunspots* and *faculae* influence the variability of the solar emission at short wavelengths in the photosphere. Sunspots appear as relatively darker patches in the photosphere because they are cooler (around 4000 K) than the surrounding sphere. The lower the temperature, the weaker the blackbody emission of the photosphere. Sunspots are associated with the strong magnetic fields that exist in the interior but the reason why sunspots are cool is not entirely understood, but one possibility is that the magnetic field in the spots inhibits convection underneath them [*Hoyt and Schatten* (1997)]. They are irregular and have an average size of about 10,000 km but range up to areas that cover more than 150,000 km. The spots are usually found in pairs, or in complex groups, oriented along the direction of the Sun's rotation. Small spots persist for several days or a week, while larger ones exists for several weeks. The number of sunspots appearing on the solar disc is highly variable and ranges from a few to a maximum of about 150, and varies with a period of 11 years, the so called *sunspot cycle*. The period is not constant, but varies between about 9.5 years and 12.5 years [*Mursuly and Ulrich* (1998)]. During each cycle, sunspots migrate from high latitudes to the equator. Sunspots never appear near the Sun's poles, but they are almost entirely confined to the region between the equator and 40° latitude. Each spot is composed of a central dark line, called *umbra*, surrounded by a lighter region, called *penumbra*. Faculae (the word facula is actually Latin for 'little torch') are bright granular structures on the Sun's surface that are slightly hotter than the surrounding photosphere. A sunspot always has an associated faculae, which appear before and disappear after the sunspot in the same place. These are also magnetic areas but the magnetic field is concentrated in much smaller bundles than in sunspots. While the sunspots tend to make the Sun look darker, the faculae make it look brighter.

The region above the photosphere is called the *solar atmosphere*, characterised by rare and transparent solar gases. Further the solar atmosphere can be divided into two layers, called the *chromosphere* and the *corona*. The chromosphere is the layer of the solar

atmosphere adjacent to the photosphere and extending outward to a high of approximately 2000 km where the corona starts. The chromosphere is far from tranquil. Every few minutes, small solar storms erupt, expelling jets of hot matter known as *spicules* into the Sun's upper atmosphere. Its boundary is defined by an increase in the atmospheric temperature with altitude (in contrast with the decrease seen in the photosphere). In about 2000 km, the temperature of the chromosphere increases from about 4000 K to 25,000 K. At this higher temperature hydrogen emits light that gives off a reddish color (H-alpha emission), this color is the origin of its name (*chromos* meaning 'color'). The chromospheric emission spectrum is composed predominantly of emission lines, mostly by hydrogen, helium, and calcium; the visible emission is weak.

Above the chromosphere lies the corona, which extends outward for several solar diameters without any boundary. The corona is irregularly shaped, very hot and extremely diluted. It can reach temperatures of few million Kelvins, and a density 10-12 that of the photosphere. A continuously stream of gas called *solar wind* flows out of the corona into the solar system. The emission spectrum of the corona contains a number of weak emissions lines and its free electrons scatter photospheric light. The emission is strong in the X-rays because of the extreme temperature of the gas.

Furthermore, transient phenomena appears in the solar atmosphere. So called *solar flares* and *prominences* occurs in the chromosphere and corona. They are associated with the sunspot groups, and part of the same physical phenomena. Flares are localised eruptions that can emit great amounts of energy. Prominences assume different shapes and appear typically as arcs of gas following the magnetic field lines associated with the sunspot groups. They extend into the corona and sometimes some of the gas completely escapes the Sun's gravity, a phenomena called *coronal mass ejection*.

2.1.2   The Sun as a Black Body

For understanding the concept of absorption and emission processes the laws of blackbody radiation are essential. This is a basic concept in physics and special for radiative processes. A black body is by definition a perfect absorber and emits the possible maximum amount of energy at a given temperature. Therefore it reflects no radiation and appears perfectly black. Its an object that absorb all electromagnetic radiation that falls onto it, no radiation passes trough it and none is reflected. Emission by a black body is the contrary of absorption. In practice no material has been found to absorb all incoming radiation. At a particular temperature the black body would emit the maximum amount of energy possible for that temperature. This value is known as the black body radiation. The maximum wavelength emitted by a black body radiator is infinite. It also emits a definite amount of energy at each wavelength for a particular temperature, so standard black body radiation curves can be drawn for each temperature, showing the energy radiated at each wavelength. All objects emit radiation above absolute zero.

Black Body Radiation Laws

In 1900 Planck devised a theory of blackbody radiation which gave good agreement for all wavelengths. In this theory the molecules of a body cannot have arbitrary energies but instead are quantised. Planck postulated that the energy is quantized and can undergo only discrete transitions, therefore the radiant energies can only have discrete values, which

can be expressed by

$$E = h\nu \ , \tag{2.1}$$

where h is Planck's constant and ν the oscillator frequency. Further he derived a relationship between the spectrum of intensity $B_\lambda(T)$, emitted by a population of molecules at absolute temperature T, which can be expressed by the *Planck function*

$$B_\lambda(T) = \frac{2hc^2}{\lambda^5 (e^{\frac{hc}{k\lambda T}} - 1)} \ , \tag{2.2}$$

where $h = 6.626 \times 10^{-34}$ Js is the Planck constant, $k = 1.3805 \times 10^{-23}$ JK^{-1} is the Boltzmann constant, and $c = \lambda\nu$ corresponds to the velocity of light, with the wavelength λ and the frequency ν of the electromagnetic radiation. The Planck and Boltzmann constants have been determined through experimentation. The Planck function establish a connexion between the emitted monochromatic intensity to the frequency and temperature of the emitting body. The resulting spectrum is called the Planck or black body spectrum and shows a single maximum at wavelength λ_m. Its radiant intensity increases with temperature and the wavelength of the maximum intensity decreases with increasing temperature. The intensity for $\lambda < \lambda_m$ decreases sharply, on the other side for $\lambda > \lambda_m$ exists a relatively wide band toward longer wavelengths. Furthermore, the black body radiation is isotropic, so the intensity is independent of the direction.

Approximately, the Sun can be described as a black body with a single emission temperature, but practically it is not a very good characterisation. A better description can be obtained by adopting a equivalent temperature which varies with frequency [*Coulson* (1975)].

By integration of the Planck function over the entire electromagnetic spectrum, it is possible to obtain the total radiance (or intensity) of a black body, this can be expressed by

$$B(T) = \int_0^\infty B_\lambda(T) \, d\lambda' \sim T^4 \ . \tag{2.3}$$

The integration over all angles and wavelengths leads to the total flux (energy per unit time) and Eq. 2.3 becomes the *Stefan-Boltzmann law*

$$F(T) = \pi B(T) = \sigma_{SB} T^4 \ , \tag{2.4}$$

where σ_{SB} is the Stefan-Boltzmann constant ($\sigma_{SB} = 5.67 \times 10^{-8}$ Jm^{-2}s^{-1}K^{-4}). As can seen in the equation above, the emitted energy flux $F(T)$ (energy per unit area and per unit time) is proportional to the fourth power of the absolute temperature.

The wavelength λ_{max} of maximum intensity follows by setting the derivative of Eq. 2.2 (with respect to λ) equal to zero, i.e.,

$$\frac{\partial B_\lambda(T)}{\partial \lambda} = 0 \tag{2.5}$$

and for the wavelength of the maximum results *Wien's displacement law*

$$\lambda_{max} T = A = const \tag{2.6}$$

(with λ in μm follows A=2898 μmK). Wien's displacement law states that for blackbody radiation the wavelength of the maximum intensity is inversely proportional to the temperature. By the aid of this property, the temperature of a black body can be determined from the wavelength of maximum radiation.

The previous three fundamental laws deal with the intensity emitted by a black body, which is dependent on the emitting wavelength and the temperature of the medium. A medium under thermodynamic equilibrium absorbs radiation of a particular wavelength, and at same time also emits radiation of the same wavelength. This means, that the emissivity ϵ_λ (defined as the ratio of the emitting intensity to the Planck function) of a medium in thermodynamic equilibrium is equal to its absorptivity A_λ (defined as the ratio of the absorbed intensity to the Planck function) and hence follows *Kirchhoff's law*

$$\epsilon_\lambda = A_\lambda \ . \tag{2.7}$$

This law states that in thermodynamical equilibrium and at a given wavelength the ratio of emissivity to absorptivity do not depend on the nature of the substance, but only depends on wavelength and temperature:

$$\frac{\epsilon_\lambda}{A_\lambda} = f(\lambda, T) \ . \tag{2.8}$$

This was first realised by the German physicist Kirchhoff in 1860. For a black body, the absorption reaches a maximum and in the same way reaches the emission a maximum value. Thus follows

$$A_\lambda = \epsilon_\lambda = 1 \tag{2.9}$$

for all wavelengths.

In general, real bodies not only absorb radiation, they also reflect a part of the incident radiation and transmit the remainder and can be defined as a *gray body* and be described by

$$A_\lambda = \epsilon_\lambda < 1 \ . \tag{2.10}$$

The ratios of the absorbed, reflected, and transmitted radiation are again functions of temperature and wavelength.

2.1.3 The Solar Spectrum

The radiation emitted by the Sun accords, in a first approximation, to the emission of a black body at a temperature of about 6000 K. The solar spectrum covers wavelengths ranging from gamma rays to radio waves. Due to nonquantised electronic transitions, the bulk of the energy is carried by the continuum. The single most important contributer is hydrogen, both in the neutral state and as negative ions. In the ionisation process the atom may absorb more than the energy required to remove the electron. This additional energy can be implemented as supplying kinetic energy to the redundant electron and is not quantised. As a consequence the absorption is not selective but rather continuous. These ionisation occurs on the shorter wavelength region of the ionisation frequency. In the visible and infrared, the solar spectrum is essentially a continuum [*Stix* (1989)].

The most important solar radiation part which affects the climate system of the Earth is in the ultraviolet, visible, and near infrared region of the spectrum. In fact 99% of the solar radiation reaching the Earth has a wavelength between 0.1 μm and 4.0 μm with 9% in the ultraviolet (below 400 nm) and the remainder part is in the visible (49%) and near infrared (42%) wavelength region [*Houghton et al.* (1984)].

The radiation emitted from the Sun's photosphere shows a maximum intensity in the visible region of the spectrum. The spectrum of radiation can be described as an

ensemble of electromagnetic waves which travels trough a vacuum at the speed of light. The electromagnetic waves cover a continuous range of wavelengths and the totality is called the *electromagnetic spectrum*. The infrared emission is actually a considerable degree higher and is more closely approximated to a 7000 K black body. On the other hand is the intensity of ultraviolet (UV) radiation reaching the Earth atmosphere somewhat less than that from a 6000 K black body, thats due to absorption by atoms and molecules in the Sun's photosphere. The solar output shows more a cooler temperature of 5100 K between 200 nm and 250 nm, and 4600 K between 130 nm and 170 nm. Figure 2.2 gives the spectral distribution of the solar radiation at the top of the atmosphere, at sea level, compared against the emission spectrum of a black body with a temperature of about 6000 K.
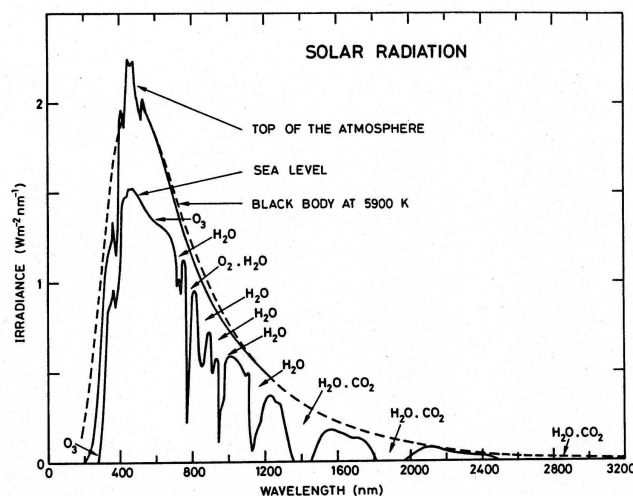

Figure 2.2. The spectrum of solar short wave radiation in the UV, visible, and infrared wavelength region outside the Earth's atmosphere, at sea level, and for a black body approximation (dashed line) for average atmospheric conditions for the Sun at zenith. At the sea level the according major absorbing species are denoted. The figure is adapted from [*Brasseur and Solomon* (1984)].

The spectrum at top of the atmosphere closely resembles the spectrum given by Planck's formula. In the wavelength region from 120 nm to 300 nm exists a superposition with absorption lines upon the continuum which increases with shorter wavelength. The source of solar emission changes from the photosphere to the chromosphere as the wavelength increases from 300 nm to 120 nm. This means that the effective emitting height of the solar continuum moves upwards in the solar atmosphere and the absorption lines superimposed on the continuum absorb increasingly more energy.

The emitted solar short wavelength radiation is therefore inversely related to the solar altitude from where it is emitted. Radiation with wavelengths of > 180 nm are emitted by the photosphere, wavelengths less than 180 nm are emitted by the chromosphere, and the very energetic components with wavelengths less than 50 nm originate in the corona.

At wavelengths shorter than 208 nm occurs a sharp increase in the solar flux, this can be associated with the Al I ionisation edge. Other less distinctive ionisation edges and their related continua in the solar atmosphere are due to other elements like H, Mg, Fe, Se, and C. Below the aluminum edge, the importance of the solar emission lines increases

30

rapidly. On the other side, the absorption lines from the spectrum below 150 nm becomes more and more negligible. Less than 140 nm, the emission by chromospheric and coronal lines begins to dominate the emission in the continuum [*Brasseur and Solomon* (1984)]. A characteristic emission occurs at 121.6 nm, the *Lyman-α* emission, which corresponds to transition from from the excited state of hydrogen.
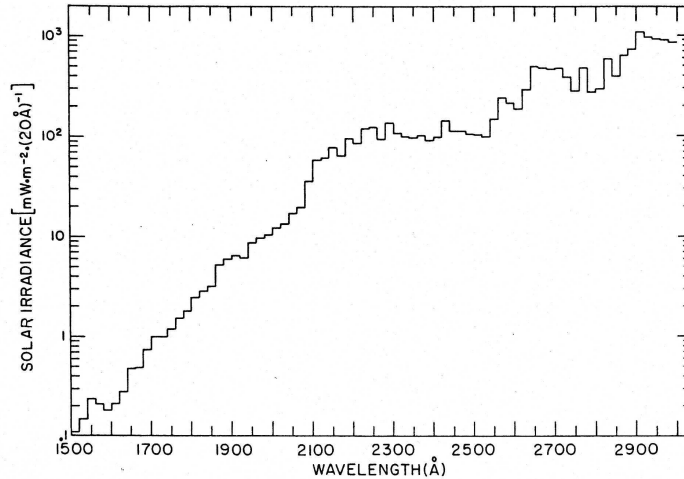

Figure 2.3. Spectral irradiance in the ultraviolet between 1500 Å and 3000 Å (adapted from [*Hall et al.* (1985)]).

The solar output varies in many regions of the electromagnetic spectrum, but in the visible band exists a small variability. For the ultraviolet radiation is the variability primarily in the extreme (EUV) and far ultraviolet (FUV), in the middle (MUV) and near ultraviolet (NUV) is the variability less than for the EUV and FUV. The solar variability is dominated by the 27-day rotation cycle of the Sun and the sunspot activity, respectively. Observations of the variability over these cycle show that the amplitude of variation decreases rapidly with wavelength [*Lean et al.* (1982)]. Figure 2.3 shows the quiet Sun flux between 1500 Å to 3000 Å arriving at the top of the Earth's atmosphere. The flux is given as summed over 20 Å intervals. There exists a large change in flux across this range, dropping about four orders in magnitude from 300 nm to 150 nm. The rotation cycle leads to variations of several percent in the UV < 250 nm and of under 1% for wavelengths longer than 250 nm [*Bertaux et al.* (1986)]. Furthermore, the activity changes between the 11-year cycle extremes are noticeable, but by a relatively small amount. The variation between the extremes in terms of the solar constant (see the Section below) is of order 0.1%. These variability decreases sharply with increasing wavelength under consideration of the inverse relationship between solar altitude and the emitted wavelength.

An excellent assessment of the actually best measurements is given by [*Rottman* (1990)], high resolution measurements of the UV solar spectrum are given by [*Hall and Anderson* (1991), *Schmidtke et al.* (1991)]. The solar variability and a more complete discussion of the solar output can be found in [*Frohlich* (1977), *Stix* (1989)]. The solar variability itself has been reviewed by [*Lean* (1991), *Lean* (1987)].

2.2 Solar Radiation in the Earth's Atmosphere

Observations of the Sun over many years shows that the intensity of the emitted radiation has not changed substantially. A quantity to describe the emitted energy is the so called *solar constant*, which is defined as the amount of solar radiation incidence (covering the entire solar spectrum) per unit area and per unit time on a surface normal to the direction of propagation of the radiation. The exact value and the magnitude of the fluctuations of the solar constant are not yet known exactly. For the Earth, the solar constant is further situated at the Earth's mean distance from the Sun. At top of the atmosphere, the value of the solar constant is about $1367 \, \mathrm{Wm^{-2}}$, which corresponds to an effective solar temperature of 5780 K. The Earth's system captures this energy and the corresponding energy is on the average $342 \, \mathrm{Wm^{-2}}$ [*Frohlich* (1977)]. The Earth atmosphere absorbs this energy, mainly due to molecular oxygen, ozone, and water vapor. The absorption of solar radiation by ozone is responsible for the heating of the stratosphere.

On top of the atmosphere the distribution of the observed solar radiation depends on the geometry of the Earth, its rotation, and its elliptical orbit around the Sun. Therefore it is a function of the eccentricity of the orbit, the longitude of the perihelion, and further a function of the angle of the Earth's axis to the plane of the ecliptic. The penetration of solar radiation and its atmospheric interaction yields to a formation of characteristic layers, whose altitudes are independent of the intensity of the radiation. The layers are strongly dependent on the physical behaviour of the atmospheric medium, the solar zenith angle, and the wavelength of the radiation.

After the solar radiation enters the atmosphere, absorption and scattering by atmospheric constituents attenuates it as it passes through the atmosphere. The absorbed radiation is directly contributed to the heat budget of the Earth, whereas the scattered radiation is partly reflected to space and partly continuous its way trough the atmosphere, where it undergoes further scattering and absorption. The maximum of depletion of the solar radiation tends to occur at high latitudes were the path length trough the atmosphere is longest, and the minimum of depletion occurs in the intertropical region were the path length is shortest. The nature and concentration of the absorbing gases and particles determine the amount of attenuation. The penetration of solar radiation into Earth's atmosphere depends on the absorption by each constituent. The absorption behaviour of the minor constituents depends on the wavelength, therefore the penetration depth is dependent on the shape of the spectrum.

Furthermore, the pathlength through which the solar beam passes affects the intensity. The pathlength depends on the angle of incidence of the solar radiance, which depends on time, latitude, and date.

2.2.1 Absorption and Scattering

Absorption

The atomic and molecular structure of a gas defines the absorption and emission of radiation in gases according to the specific wavelength of the radiation. Any isolated molecule (just as atoms) possesses a certain amount of energy and can only absorb in certain discrete energy states and can only undergo discrete changes between these states. The quantum theory also requires that energy transmitted by electromagnetic radiation exists in discrete units. Radiation occurs only when the atom makes a transition from one

state with energy E_k to a state with lower energy E_j, and the atom emits a photon of energy as given in Eq. 2.1. The lowest energy state is called the *ground state*, and when an electron of an atom absorbs energy due to a collision and descend into a large orbit, the atom is said to be in an *excited state*. Electrons can be removed from an orbit if a characteristic amount of energy is absorbed. This amount referred to the ground state is called the *ionisation potential*. Contains the atoms or molecules more than one electron, the ionisation potential usually refers to the electron that requires the energy for removal. The amount of energy to dissociate the atoms is called the *dissociation potential*.

Thus if a molecule changes from a state of lower energy to one of higher, it has to absorb the necessary quantised energy given by $h\nu$, where ν is the frequency of radiation. These feature can be described in quantum-mechanical terms by $E_k - E_j = h\nu$. It follows that an isolated molecule interacts only with radiation having certain discrete wavelengths. If the molecule absorbs radiant energy, the electrons can go to a higher discrete orbit under consideration of their selection rules. Further exist additional, lesser energy amounts. These results from change of the electronic state, called *electronic energy*, from the vibration of the individual atoms about their mean position in the molecule (the atoms of a molecule are bounded by certain forces such that the individual atoms can vibrate about their equilibrium positions relative to one another), called *vibrational energy*. Furthermore from the rotation of the molecule about its center of mass (a molecule can rotate, or revolve, about an axis trough its center of gravity), called *rotational energy*. Radiation can permit only a certain configuration of electron orbits within the atom, further certain frequencies of vibration and vibration amplitudes, and certain rotation states. The sum of these three energy states identifies each possible combination of electron orbits, vibration, and rotation.

For each chemical element or combination exists a characteristic absorption and emission spectrum, which shows the frequencies of absorption and emission respectively. These properties can be described in terms of a line spectrum, which consists of a finite number of narrow absorption or emission lines. So for each particular atmospheric gaseous species exists a spectrum, the atmospheric absorption spectra therefore consist of all these lines. If the radiation which penetrate the gas cannot excite the atoms or molecules, the energy will not be absorbed or emitted. Molecular gases absorb in bands which consists of a large number of closely spaced spectral lines. The molecular spectra are much more complex than those for individual atoms because they have more degrees of freedom. Also are the quantized vibrational and rotational energy transitions much smaller than those in the electronic transitions. Only for diatomic molecules with an oscillating electric dipole moment exist rotational or vibrational spectra. A dipole moment results, if the effective centers of the positive and negative charges have nonzero separation. Molecules with permanent electric dipole moments, such as H_2O and O_3, interact strongly with electromagnetic radiation due to their asymmetrical charge distribution. Linear molecules, such as N_2 and O_2, are inactive because of their symmetrical charge distribution, otherwise they have weak magnetic dipole moments that allow radiative activities. Electronic transitions are stimulated by radiation in the ultraviolet and visible wavelength region. So their absorption (and emission) spectra are due to electronic transitions with vibration-rotation features superimposed. Vibrational and rotational transition occur at IR wavelength, transitions between electronic levels due to UV and visible radiation. Molecular oxygen and ozone meanly interacts in these wavelength range.

Rotational energy changes are relatively small, therefore pure rotational lines occur

in the microwave and far-infrared spectra. Changes in the vibrational states are generally much larger than the minimum changes in rotational energy. Thats the reason why vibrational transitions never occur alone but are coupled with simultaneous rotational transitions. This coupling rise to a group of lines known as vibrational-rotational band. Because of the high energy which is required for the transition, the absorption and emission usually occurs in the ultraviolet of visible spectrum. Atoms can produce line spectra, molecules can have two additional types of energy, leading to more complex band structures in their spectra.

Considering *Heisenbergs uncertainty principle*, the individual lines in the absorption spectra of an isolated molecule have finite widths. Monochromatic emission is practically never observed. Energy levels during energy transitions are usually slightly changing (due to both, external influences, and the loss of energy in emission), therefore follows the non-monochromatic emitted radiation, and spectral lines of finite widths can be observed. Furthermore, the *Doppler broadening* within the gas expands the width of the lines, the amount depends upon the velocity of the gas molecules, which is directly proportional to the square root of the absolute temperature. This line broadening is associated with random motions of the gas molecules due to the difference in thermal velocities of atoms and molecules. The perturbation due to reciprocal collisions between the absorbing and non absorbing molecules tends to a broadening of the spectral lines. The interactions between the electrostatic force fields of individual molecules during collisions result to a *collision broadening*, where the amount depends upon the frequency of molecular collisions, which is directly proportional to the pressure of the gas (for more details about line broadening see for instance, [*Mitter* (1993), *D.G. Andrews* (1987)]). In the altitude region extending from 20 km upwards, effective line shapes are determined by both collision- and Doppler broadening processes.

The absorption behaviour of various molecules depends on their molecular structure. Molecules with diatomic structure like N_2 or O_2 have two nuclei, those can only move toward and away from each other during vibration. Hence diatomic molecules have one vibrational mode, noted as symmetric stretch. Due to the symmetrical charge distribution diatomic molecules lack a permanent dipole moment which can acquire oscillating momentum during vibration. Thats why diatomic molecules show little radiative activity in the visible and infrared wavelength region.

Triatomic molecules with a linear symmetric assembling like CO_2 or NO_2 show three vibrational modes, one for symmetric stretch, one for bending motion, and one for antisymmetric stretch. The outcome of this linear symmetry is the absent of permanent electric dipole moment. Due to vibrational symmetry, the vibration mode is radiatively inactive at its fundamental. The triatomic structure for O_3 or H_2O molecules forms an isosceles triangle and has tree fundamental vibration modes.

Diatomic and linear triatomic molecules show three equal moments of inertia and two degrees of rotational freedom. Asymmetric top molecules features three unequal moments and three degrees of rotational freedom. Molecules with larger complexity features additional degrees of freedom.

Scattering

Considering the denser layers of the atmosphere, solar radiation is diverted or scattered from its direction of propagation due to the presence of large concentrations of particles,

such as air molecules, aerosols, and clouds. Aerosols are defined as suspensions of liquid or solid particles in the air, their mean radius ranges from about 10^{-4} μm to 10 μm [*Houghton* (1985)].

Scattering is the process, when a particle in the path of an electromagnetic wave extracts energy from this incident wave and reradiates that energy in all directions. The frequency of the scattered radiation does not change, but its phase and polarization may change substantially from those of the incident radiation. The particles act as a new source of radiation, scattering occurs for particles of all sizes. Scattering of solar radiation does not lead to a conversion of radiant energy into heat as does absorption.

The ratio of the particle size to the wavelength of the incident radiation determines the relative intensity of the scattered light. *Rayleigh scattering* occurs when this ratio is small; the scattered light is distributed equally in the forward and backward directions. This theory generally describes the scattering of unpolarized light by air molecules. Rayleigh scattering is important when the scattering cross section becomes comparable to the absorption cross section. Approximately the scattering cross section varies as the inverse fourth power of the wavelength ($\sim \lambda^{-4}$), the shorter the wavelength the more radiation will be scattered.

Due to the strong absorption behaviour of molecular oxygen and ozone for wavelength regions less than about 250 nm in the atmosphere follows a reduction and modification of the effects of Rayleigh scattering. For larger particles an increasing part of the light is concentrated in the forward direction, this case is called *Mie scattering* and the distribution of scattered light intensity with scattering angles becomes very complex.

In the Earth's atmosphere the particles which are responsible for scattering cover a range of sizes from gas molecules ($\approx 10^{-10}$ m, equivalent to Rayleigh scattering) to large raindrops and hail particles ($\approx$ cm, basically Mie scattering). In general can the change in direction of the incident radiation be explained for large particles by geometrical optics. In the Earth's atmosphere are three scattering processes important: reflection and scattering from the underlying surface and troposphere (including clouds and aerosols), molecular scattering (in essence Rayleigh scattering), and scattering by aerosols (particularly volcanic aerosols; in essence Mie scattering). Up to the stratosphere, scattering is the dominant radiative transfer process, with scattering from aerosols, clouds, and larger particles.

A more detailed discussion about atmospheric absorption and scattering can be found in e.g., [*Brasseur and Solomon* (1984), *Salby* (1995)].

2.2.2   Spectral Regions of Photochemical Importance in the Atmosphere

For the Earth's climate is the absorption of radiation by gases one of the most important aspects. The principle absorbers and ionisation limits are shown in Fig. 2.4. The Figure shows the altitude at which vertically incident solar radiation is decreased to e^{-1} of its value outside the atmosphere. The minor constituents of the atmosphere are responsible for the most pronounced absorption of both, solar and terrestrial radiation (not only nitrogen (N_2) and molecular oxygen (O_2) contributes). Water vapor (H_2O) and carbon dioxide (CO_2) absorb much of the long-wave terrestrial radiation. The most important absorbing gases in the atmosphere are oxygen (O_2), ozone (O_3), water vapor (H_2O), and carbon dioxide (CO_2), and their oxides (N_2O, NO_2), and methane (CH_4). The absorption spectra are quite complex, but as seen in Fig. 2.4, exist regions of absorption in which the absorption is so strong that no solar energy reaches the surface of the Earth. Absorption by ozone and molecular oxygen is responsible for removal of virtually all of the incident

solar radiation shorter than 290 nm. Molecular oxygen absorbs only the radiation at wavelengths less than 242.4 nm. Ozone primarily absorbs between 200 nm and 300 nm, but also to some extent in the visible and infrared wavelength region.

On the other side exist so called *optical windows* (spectral regions where the absorption by the atmosphere is quite weak) in the spectra, because absorption is not strong from 300 nm to 800 nm, about 40% of the solar energy is concentrated in the region between 400 nm and 700 nm. In this region the atmosphere is essentially transparent. From 800 nm to 2000 nm, terrestrial long-wave radiation is absorbed in a complicated way mostly by water vapor, but also by CO_2 and other trace gases. The fact, that molecules absorb in particular regions of the spectrum can be determined only by quantum mechanical calculations, according to the optical properties of the medium. In the atmosphere above 20 km, radiation with wavelengths shorter than 300 nm, (ultraviolet and X-rays) is mainly absorbed by O_2, O_3, O, and N_2. The very intense Lyman α line emission at 121.6 nm can reach the upper part of the middle atmosphere due to theirs positioning in an optical window in this wavelength region (effectively dissociate water vapor, carbon dioxide, and methane). Radiation with wavelengths shorter than 100 nm is almost completely absorbed above 100 km by molecular and atomic oxygen, and by molecular nitrogen. Ionization due to extreme ultraviolet and X-rays occurs at very high levels, the ionization forms and maintains the so called *ionosphere*.
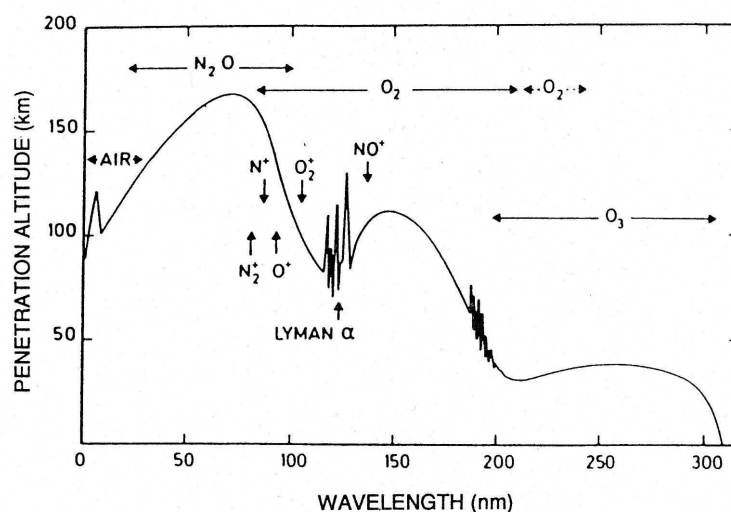

Figure 2.4. Altitude at which the solar irradiance decreases to e^{-1} of its value outside the Earth's atmosphere for vertical incidence. The solar flux is attenuated by a factor $1/e$. The principle absorbing species and thresholds for photoionisation are indicated (adapted from [*Salby* (1995)]).

For the region below 40 km, the absorption of solar radiation due to ozone and molecular oxygen is of major importance. Ozone forms the stratosphere and mesosphere by photochemical processes, the maximum concentration can be found between 20 km and 30 km height. A depletion of the stratospheric ozone would result in an increase of the ultraviolet radiation at the Earth's surface, including incalculable consequences for the biosphere. From this absorption properties follows the abrupt cutoff at wavelengths at about 300 nm of the solar radiation entering the troposphere. In the troposphere, the absorption of solar radiation is rather weak and mainly occurs in the visible and near

infrared (0.55 μm $< \lambda < 4.0$ μm) wavelength region due primarily to H_2O, CO_2, and clouds. In the lower atmosphere, the aerosol absorption behaviour has to be considered. Aerosols heat the troposphere by the absorption of solar energy.

Wavelength	Atmospheric absorbers
121.6 nm	Solar Lyman α line, absorbed by O_2 in the mesosphere; no absorption by O_3.
100 - 175 nm	O_2 Schumann-Runge continuum. Absorption by by O_2 in the thermosphere; can be neglected in the mesosphere and stratosphere.
175 - 200 nm	O_2 Schumann-Runge bands. Absorption by O_2 in the mesosphere and upper stratosphere.
200 - 242 nm	O_2 Herzberg continuum. Absorption by O_2 in the stratosphere and weak absorption in the mesosphere. Weak absorption by O_3 in the Hartley band.
242 - 310 nm	O_3 Hartley band. Absorption in the stratosphere leading to the formation of $O(^1D)$.
310 - 400 nm	O_3 Huggins bands. Absorption in the stratosphere and troposphere leading to the formation of $O(^1P)$.
400 - 850 nm	O_3 Chappius bands. Absorption in the troposphere features photodissociation at the surface.

Table 2.2. Spectral regions of photochemical importance in the atmosphere.

Table 2.2 shows the different spectral regions of photochemical importance in the UVVIS wavelength region for molecular oxygen and ozone. Ozone absorbs at longer wavelengths than oxygen thus can penetrate to lower altitudes. The *Hartley* band (see Section 2.5.4) is the primary ozone absorption region and lies between 200 nm to 310 nm. The Hartley band merges the *Huggins* bands at 310 nm to 400 nm. Further absorbs ozone in the visible wavelength region between 400 nm to 850 nm, which are the *Chappius* bands and these are importance in troposphere and lower stratosphere.

The Hartley and Chappius bands features continuous spectra, the Huggins bands contain a spectrum of diffuse lines. The *Herzberg* continuum is situated at wavelengths of 200 nm to 242 nm, where O_2 is dissociated into two ground-state oxygen atoms. At shorter wavelengths, the *Schumann-Runge* bands specify the absorption spectrum, where O_2 is vibrational excited. A detailed discussion about the Schumann-Runge absorption system is given in Section 2.5.1. Wavelengths shorter than 175 nm are absorbed in the Schumann-Runge continuum, where O_2 is dissociated into two oxygen atoms, one electronical excited. Absorption at shorter wavelengths features an irregular banded structure that eventually merges into the ionisation continuum at wavelengths shorter than 102 nm.

2.3 Radiative Transfer

The Earth-atmosphere system reflects about 30% of the incoming solar radiation at the top of the atmosphere and absorbs the remaining part. A major part of the solar irradiation is absorbed by the Earth's surface, approximately 70% by the ocean and 30% by land. Considering a climatological period of time (a year or longer), the global-mean temperature

of the Earth-atmosphere system is relatively constant. Therefore the solar energy absorbed in the Earth-atmosphere system must be reemitted into space to accomplish approximately the global thermal equilibrium.

2.3.1 The Global Radiation Balance

The solar radiative energy constitutes the basic driving force for atmospheric circulations. Its the ultimate source of energy that drives weather and climate in the Earth atmosphere. The absorption of solar radiation by the atmosphere and surface leads to heating of the climate system. The most important external factor for the Earth's climate is the total incoming solar radiation. The solar incoming energy is mainly absorbed in the atmosphere by molecular oxygen, ozone, and water vapor. The residual part of solar radiation that is not absorbed in the atmosphere or backscattered to space reaches the Earth's surface.

The energy is mostly provided in the ultraviolet, visible, and near-infrared wavelength region (wavelength between 0.2 μm and 4.0 μm). The short wave (SW) energy flux at top of the atmosphere normal to the incident ray direction can be characterised by the solar constant (see Section 2.2), which is approximately equal to 1370 Wm^{-2}. The total incoming energy captured by the Earth's system is on the average 342 Wm^{-2}, of which about 31% (equal to 107 Wm^{-2}) is returned to space by clouds and Earth's surface (24% due backscattering by clouds, air molecules, and particles, the remaining 7% due to reflection at the Earth's surface). This amount of backscattered solar radiation without changes in wavelengths is called albedo. About 25% (87 Wm^{-2}) of the incoming energy
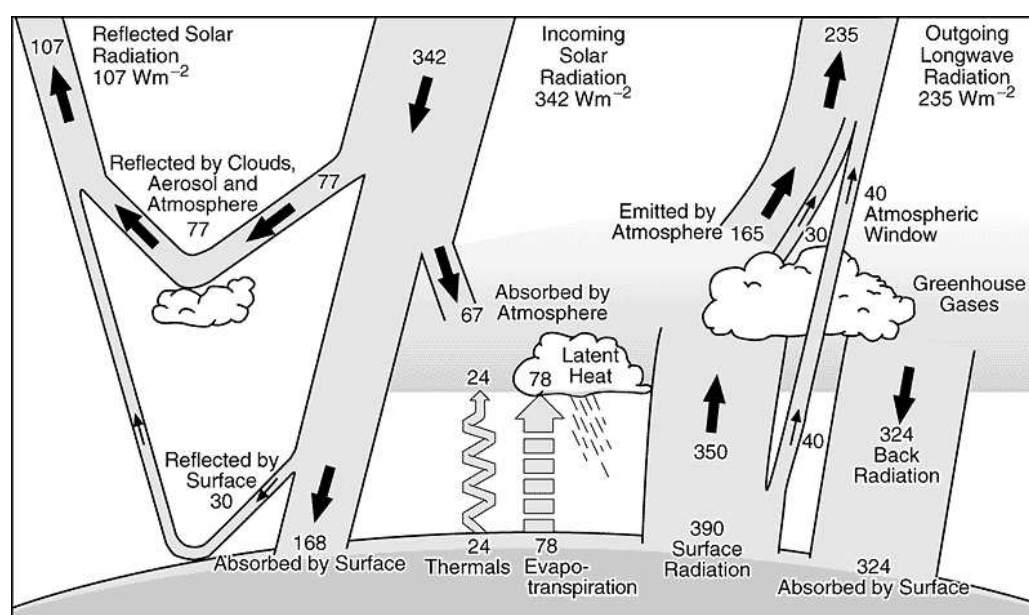

Figure 2.5. Schematic diagram of the global radiation budget in the climatic system. The diagram shows the interaction of solar radiation with the Earth atmosphere. The incoming solar radiation is partially reflected by the atmosphere, about half of the amount of energy is absorbed by the Earth's surface. Adapted from [*Brasseur and Solomon* (1984)].

is absorbed within the atmosphere, by ozone in the middle atmosphere, and by clouds and water in the troposphere. The remaining energy 43% or 148 Wm^{-2} is absorbed by the Earth's surface. At the wavelengths of solar radiation, atmospheric emission is

negligible, therefore only absorption needs to be considered. Figure 2.5 approximately describes the global energy budget of the Earth system. All the processes shown in the figure are responsible for the temperature structure of the atmosphere and also determine the temperature at the surface.

The solar energy absorbed by the Earth is reradiated as infrared radiation. This energy is mostly absorbed by clouds and atmospheric particles such as water vapor and carbon dioxide. These two gases are able to carry a large fraction of that energy (mostly in the 12 μm to 20 μm region) in the lowest region of the atmosphere. The atmosphere shows a relatively weak absorption behaviour in the wavelength region between 8 μm to 12 μm (called the atmospheric window), therefore terrestrial radiation is able to propagate into space. As a consequence of these weak absorption, any gas with strong absorption properties in this spectral region is relatively efficient in trapping terrestrial radiation.

With the principle of conservation of energy, it is possible to calculate the heating or cooling of an atmospheric layer due to the change in net solar and terrestrial radiation with height. The resulting thermal effects can be studied by using mathematical models, generally by solving the radiative transfer equation (see Section 2.3.3). From this examinations follows a net cooling of the atmosphere by the long-wave radiation component at the order of 2.5 K per day. The averaged heating of the atmosphere by absorption of solar radiation is only of the order of 0.5 K per day, and therefore, it does not compensate the cooling by long-wave radiation. The maintenance of a steady state in the atmosphere is only possible through the transfer of sensible heat (enthalpy) and latent heat (evaporation-condensation) from the Earth's surface to the atmosphere.

The concentration of some of the absorbers (cf. ozone) varies strongly with height, so the solar and terrestrial radiation fluxes are also strongly height dependent. The short-wave solar radiation dominates the net radiation balance in the daytime, on the other hand at night the long-wave radiation flux dominates. Water vapor is responsible for the net radiative cooling in the troposphere. The absorption of ultraviolet radiation by ozone in the Huggins and Hartley bands is the principle source of heat in the stratosphere, a smaller extent results due to the absorption of long-wave terrestrial radiation in the 9.6-μm band. Therefore results a heating rate of about 12 K per day near the stratopause, with a maximum of about 18 K per day near the summer pole. The ozone concentration determines these numbers. The long-wave heating is only possible because of the low concentration of ozone in the troposphere.

Above about 75 km to 80 km, the absorption of molecular oxygen in the Schumann-Runge bands is responsible for the heating of the atmosphere. Except in the polar regions exists a net heating rate near 2 K per day, but there is a strong net cooling, up to 10-15 K per day, in the winter polar region between the stratopause and mesopause, and a weaker heating, up to 5 K per day, in the summer polar lower mesosphere [*Kiehl and Solomon* (1986)]. These facts exert a strong control on the seasonal varying temperatures and zonal winds. In the stratosphere and lower mesosphere the dynamical contributions to the global-mean heating are small at any level, therefore the global-mean net radiative heating is small throughout this region. In the middle and upper mesosphere these dynamical processes are larger, but still small contributions to the net heating rate.

At 100 km results a heating rate of about 10 K per day, but there exists a large variation with latitude and season. Ultraviolet radiation is responsible for the dissociation of molecular oxygen, forming atomic oxygen. At altitudes above 80 km extends the lifetime of atomic oxygen to near one day, and the energy which is absorbed by O_2 photolysis is

stored as chemical energy. This energy is released as thermal energy when the oxygen atom recombines. Much of this chemical energy is released in high latitude winter due to horizontal and vertical transport. This process and the adiabatic heating are a result of downward vertical velocities, both together lead to the warm mesopause temperature observed in winter.

The contribution to the heating rate through the absorption of molecular oxygen in the Herzberg continuum in the middle atmosphere is weak, thus contribution can be neglected relative to the effects of ozone in the stratosphere. Some O_2 bands also exist at wavelengths longer than 760 nm in the visible wavelength region. Noctilucent clouds, forming in the upper mesosphere and polar stratospheric water ice clouds, have also a small influence on heating in the middle atmosphere. Noctilucent clouds occur during the summer near the mesopause, furthermore are these clouds an indicator of water-vapor condensation in the upper mesosphere. But these clouds have only a minor effect on the radiative balance [*Pollack and McKay* (1985)].

The cooling in the middle atmosphere by radiative emission is principally due to the 15 μm band of carbon dioxide. For the stratosphere and mesosphere results a cooling rate of about 2 K per day. The maximum of the cooling rate is found at the winter mesopause, where the temperature is relatively warm. A further contribution to infrared cooling in the middle atmosphere is the emission in the 9.6 μm band of ozone. The infrared emission at 80 μm by water vapor in the middle atmosphere is relatively weak.

2.3.2 The Greenhouse Effect

Radiative active gases, called *greenhouse gases*, absorb a small fraction of solar energy, but these gases are very effective in absorbing as well as emitting long wave radiation. Greenhouse gases have very small volume mixing ratios (like water vapor and carbon dioxide less than 0.1%) and absorb effectively the infrared radiation coming from the Earth's surface and atmosphere. Typical absorbing bands of greenhouse gases are the 9.6 μm band of O_3 and the 15 μm band of CO_2. As well the atmospheric window and other gases such as water vapor and CH_4 are noticeable. The net effect of these greenhouse gases is the reduction of the amount of radiative energy emitted to space, otherwise they features an increase of radiative energy provided to the lower atmosphere and surface system.

From the terrestrial energy emitted by the surface (about 390 Wm^{-2}), only 40 Wm^{-2} escapes directly to space in the atmospheric window (corresponds to 12% of the incoming solar radiation). The remaining amount of energy (around 310 Wm^{-2} or 90%) is absorbed in the troposphere by water vapor, CO_2, O_3 and other greenhouse gases as mentioned above. Also clouds and aerosols are responsible for absorption of the terrestrial radiation. At least, 335 Wm^{-2} (denotes 98%) is emitted back to the surface, while 195 Wm^{-2} (or 57%) is emitted to space. The difference between radiative emission at the surface and the total infrared emission to space represents the *greenhouse effect*.

The largest contribution to the greenhouse effect is provided by water vapor and CO_2, and other trace gases like CH_4, N_2O, O_3, CFCs, HCFCs, and HFCs. The greenhouse gases therefore retain heat within the atmosphere, which is called the natural greenhouse effect. The natural greenhouse effect is responsible for the observed global mean temperature ($\sim 15°$C). The increase of concentration of man made greenhouse gases like CFCs, HCFCs, and HFCs features additional heating. The opacity of the atmosphere increase and the altitude where radiation is reemitted back to space is higher. As a result of these increasing

opacity, the temperatures at higher altitudes are lower and less energy is emitted, this leads to a rise in radiative forcing. This effect is called the *enhanced greenhouse effect*. For a stable climate, a balance between incoming and outgoing radiation is required.

2.3.3 Radiative Transfer Equations

Solar radiative energy is the basic driving force for atmospheric motions and the most important external factor for the Earth's climate. At the wavelengths of solar radiation, atmospheric emission is negligible, therefore only absorption needs to be considered. For wavelengths of terrestrial radiation, absorption and emission are equally important and must be considered simultaneously. To understand the absorptive behaviour of the atmosphere, the analysation of the transfer of terrestrial radiation through an absorbing and emitting medium is necessary. This means the description of the radiative transfer with its three dimensional dependence on wavelength and directionality. For an atmospheric radiative transfer theory it is helpful to make two approximations. First, the curvature of level surfaces due to the sphericity of the planet is negligible for many applications. The second one is, that the properties of the medium and the radiation field depend only on the vertical coordinate. Together, these conditions comprise the plane-parallel approximation.

The monochromatic radiation or intensity in a given medium passing through the pencil of light is given by $\mathbf{I}_\lambda = I_\lambda \hat{\boldsymbol{\Omega}}$, depending on wavelength λ. The intensity (or radiance) represents the amount of energy dE traversing a surface dA with unit normal $\mathbf{n}$ per unit time dt in a pencil of solid angle $d\Omega$ inclined at an angle Θ (see Fig. 2.6) relative to the normal to the surface and can be written as

$$\mathbf{I}_\lambda = \frac{dE}{dt\,dA\,d\Omega\,\cos\Theta}\,\hat{\boldsymbol{\Omega}}\;.\tag{2.11}$$

The monochromatic radiance is defined at each point $\mathbf{s}$ in space and for each direction $\hat{\boldsymbol{\Omega}}$
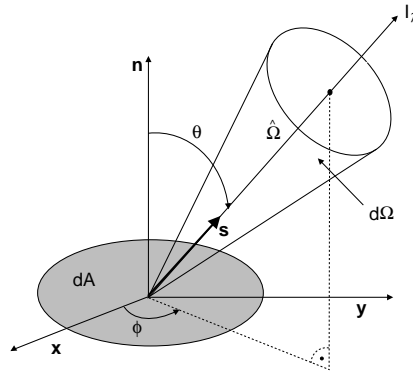

Figure 2.6. Geometry of a pencil of light in direction Ω traversing the surface element dA with unit normal $\mathbf{n}$. The angle Θ denotes the inclination of the beam. Adapted from [*Retscher* (2004)].

of the beam of light. Integrating $\mathbf{I}_\lambda$ normal to the surface with positive $\mathbf{n}$ direction over all solid angles $d\boldsymbol{\Omega}$ defines at each point $\mathbf{s}$ the net radiant flux $F_\lambda(\mathbf{s})$ crossing a plane surface and can be written as

$$F_\lambda(\mathbf{s}) = \int_{4\pi} I_\lambda(\mathbf{s}, \boldsymbol{\Omega}')\,d\boldsymbol{\Omega}'\tag{2.12}$$

and is expressed in Wm^{-2}. Multidimensional radiation is called diffuse, and if the radiation arrives along a single direction, like incoming solar radiation, it is termed parallel beam radiation. For a plane parallel atmosphere at altitude z, the net flux can be separated into its upward propagating $F_\lambda^\uparrow$ and downward propagating $F_\lambda^\downarrow$ components such that the net flux can be written as

$$F_\lambda(z) = F_\lambda^\uparrow(z) - F_\lambda^\downarrow(z) \ . \tag{2.13}$$

The monochromatic radiance represents the spectral density of the radiance at wavelength λ. Absorption and emission are not monochromatic, therefore the radiance has to be integrated over a finite wavelength interval

$$F(z) = \int_\lambda F_\lambda(z)\, d\lambda' \ . \tag{2.14}$$

The attenuation of a beam of light depends on the density and the absorption characteristics of the medium trough which it passes. Energy can also be scattered into, out of, or emitted into the solid angle. Absorption and scattering constitute the net extinction of energy passing trough the pencil of radiation.

Beer-Bougert-Lambert's Law

Electromagnetic radiation can interact basically with matter through absorption, scattering, and emission. A pencil of radiation is attenuated proportional to the density and absorbing characteristics of the medium through which it passes. So the probability of absorption by a molecule depends on the behaviour of the molecule and the wavelength of the incoming radiation. The incident radiation can also be scattered out of this beam. So both, absorption and scattering, constitute the net extinction of energy passing through a pencil of radiation. Further intensifies energy emitted or scattered into this beam from other directions the flow of energy through the pencil of radiation.

For a beam of monochromatic radiation of unit cross-sectional area with intensity I_λ, passing through an absorbing medium, the intensity after traversing a layer of thickness ds in the direction of propagation, $I_\lambda + dI_\lambda$, is increment changed by

$$dI_\lambda = -n\sigma_\lambda I_\lambda\, ds \ , \tag{2.15}$$

where σ_λ is the extinction cross section (referenced to an individual particle and has the dimension of area) and n the number density of the gas. This equation is known as the *Beer-Bougert-Lambert's law* and characterises the decrease of spectral radiance, which is proportional to the mass of absorbing and scattering material encountered along the ray path. This relation states that radiance decreases monotonically with increasing path length through the layer. The cross section describes the effective absorbing area of an increment of mass for the wavelength λ. The extinction coefficient σ_λ consists of an absorption $\sigma_{a\lambda}$ and a scattering part $\sigma_{s\lambda}$

$$\sigma_\lambda = \sigma_{a\lambda} + \sigma_{s\lambda} \tag{2.16}$$

and generally depends on temperature and pressure. It measures the characteristic distance over which energy is attenuated. The extinction coefficient can be derived from measurements or calculated from quantum mechanic processes.

Another measure to describe this principle can be expressed in terms of the specific extinction cross section $\hat{\sigma}_\lambda$, which has units of area/mass. The fractional energy absorbed from a pencil of radiation is proportional to the mass traversed by the radiation, therefore results

$$dI_\lambda = -\rho\hat{\sigma}_\lambda I_\lambda \, ds \ , \tag{2.17}$$

where $\hat{\sigma}_\lambda$ is equivalent to the effective area of that mass and ρ is the density of the medium.

By integration of Eq. 2.15 along the path of radiation defines the emergent intensity

$$I_\lambda(s) = I_\lambda(0) \, \exp\left[-\int_0^s n(s') \, \sigma_\lambda(s') \, ds' \right] \ . \tag{2.18}$$

The number density n depends on the path s against the change in density over altitude in a real atmosphere. The radiance decreases monotonically with increasing path length through the layer.

For the intensity inside a pencil of radiation follows, that the intensity exponentially decreases with the optical path length or also called *optical thickness*

$$\tau_\lambda(s) = \int_0^s n(s')\sigma_\lambda(s') \, ds' \ , \tag{2.19}$$

which is a measure of the depletion that the beam of radiation has experienced as a result of its passage through the layer, weighted according to the density and extinction cross section of the medium. In penetration downward through a layer of unit optical thickness, the intensity of the monochromatic radiance of the incident beam is diminished by a factor e. A medium is called optical thick if the total optical thickness is greater than one, the radiation is absorbed before it can traverse the medium. Otherwise, if the optical thickness is much smaller than one, the medium is called optical thin and the radiation traverse the medium with little attenuation.

For monochromatic radiation results the so-called *transmissivity* or also called *transmission function* Tr_λ of the medium at a given wavelength

$$Tr_\lambda(s) = \frac{I_\lambda(s)}{I_\lambda(0)} = \mathrm{e}^{-\tau(s)} \ , \tag{2.20}$$

which describes the fraction of incident radiation remaining in the pencil at a given distance. From this equation follows, that the transmissivity decreases exponentially with increasing optical thickness. On the other side, the monochromatic *absorptivity* a_λ determines the fraction of incident radiation that has been absorbed from the pencil of radiation, therefore it follows

$$a_\lambda(s) = 1 - Tr_\lambda(s) = 1 - \mathrm{e}^{-\tau(s)} \ . \tag{2.21}$$

The absorptivity approaches unity exponentially with increasing optical thickness.

Schwarzschild Equation

The basic equation of radiative transfer can be obtained due to an extension of Beer-Bougert-Lambert's law. Including that the gas along the ray path is also emitting radiation of wavelength λ, an extra term J_λ has to be added in Eq. 2.15 and an expression of the

energy balance in each unit volume of the medium follows. The equation of radiative transfer can be written as

$$\frac{dI_\lambda}{n\sigma_\lambda \, ds} = J_\lambda - I_\lambda \ . \tag{2.22}$$

The equation above describes the radiative transfer in general form for a layer bounded by two infinite parallel planes of a horizontally stratified medium. Both, extinction and emission are characterised by Eq. 2.22. For the atmosphere, the source function J_λ expresses the incoming radiation due to either scattering from all directions, to solar radiation, or to thermal emission by atmospheric molecules. The importance of these contributions varies with the spectral range of interest.

In the case of a plane-parallel atmosphere, where local thermodynamic equilibrium conditions apply and in the absence of scattering, the source function in the radiative transfer equation is equal to the black body monochromatic radiance, given by the Planck function (Eq. 2.2)

$$J_\lambda = B_\lambda(T) \ . \tag{2.23}$$

The equation of radiative transfer therefore reduces to the so called *Schwarzschild equation*

$$\frac{dI_\lambda}{n\sigma_\lambda \, ds} = B_\lambda - I_\lambda \ , \tag{2.24}$$

where σ_λ then equals the absorption cross section $\sigma_{a\lambda}$. The first term in the right-hand side of Eq. 2.24 denotes the increase in the radiant intensity arising from blackbody emission of the material, whereas the second term represents the reduction of the radiant intensity due to absorption. The Schwarzschild equation shows the theoretical possibility of determination of the intensity of radiation at any point of the atmosphere if the distribution of absorbing mass and the absorption coefficients are known.

The solution of the equation of radiative transfer can be expressed formally when the optical thickness τ_λ is inserted into Eq. 2.22

$$\frac{dI_\lambda}{d\tau_\lambda} + I_\lambda = J_\lambda \ . \tag{2.25}$$

By integration of Eq. 2.25 from 0 to $\tau_\lambda(s)$ follows

$$I_\lambda e^{\tau_\lambda} = \int J_\lambda e^{\tau_\lambda'} d\tau_\lambda' + C \tag{2.26}$$

and including the boundary condition $I_\lambda(s_0) = I_\lambda(0)$ yields to

$$I_\lambda(s) = I_\lambda(0)e^{-\tau_\lambda} + \int_0^{\tau_\lambda} J_\lambda(\tau_\lambda') \, e^{-(\tau_\lambda - \tau_\lambda')} \, d\tau_\lambda' \ . \tag{2.27}$$

The first term in Eq. 2.27 describes the absorption attenuation of the radiant intensity by the medium, according to an exponential decrease with the path length of the incident intensity $I_\lambda(0)$, and is essentially equivalent to Beer-Bougert-Lambert's law. The second term represents the emission contribution from the medium along the path from 0 to s.

2.3.4 Chapman Theory

When solar radiation penetrates into the Earth's atmosphere, the photons undergo collisions with atmospheric molecules and therefore, these solar photons are absorbed and scattered. The amount of absorption by a molecule depends on the nature of the molecule and the wavelength of the incoming radiation. The Beer-Bouguert-Lambert law describes this absorption of incident intensity passing through a medium. The solar radiation penetrates the Earth's atmosphere at an angle of incidence, the local zenith angle χ, which depends on the local time, season, and latitude.

Furthermore, the rate of photodissociation and the production of heat directly depend on the rate of energy deposition in the atmosphere by absorption. The penetration of solar radiation and its interaction with the atmosphere leads to the formation of layers whose characteristic altitude is independent of the intensity of the incident radiation, but strongly dependent on the nature and concentration of the absorbing gas, the solar zenith angle χ, and the wavelength of radiation. Therefore, for polychromatic radiation several absorbing layers are found at different altitudes, because there exist regions of strong absorption by one or more absorbing gases corresponding to different wavelengths. This was first presented by Sydney Chapman in 1931. The attenuation of solar radiation in the atmosphere depends on the solar zenith angle, therefore the Beer-Bouguert-Lambert law can be written as

$$I_\lambda(z,\chi) = I_\lambda(\infty)\exp(-\tau_\lambda(z,\chi)) \ , \tag{2.28}$$

where z corresponds to the altitude and $I_\lambda(\infty)$ represents the solar intensity outside the Earth's atmosphere. Neglecting the curvature of the Earth for the variation of the path of the incident radiation gives

$$ds = dz\sec\chi \ , \tag{2.29}$$

where dz is a unit of altitude. Therefore, the variation of monochromatic radiation can be written as

$$I_\lambda(z) = I_\lambda(\infty)\exp\left[-\sec\chi\int_z^\infty n(z')\sigma_{a,\lambda}dz'\right] \ . \tag{2.30}$$

In practice an expression should be used which accounts for the combined effects of several absorbing gases. In the middle atmosphere dominates absorption of ultraviolet radiation by molecular oxygen, or ozone, or both. With regard to the zenith angle of the incident solar radiation the optical thickness then reads

$$\tau_\lambda(z,\chi) = \sec\chi[\tau_\lambda^{O_2}(z,\chi) + \tau_\lambda^{O_3}(z,\chi)] \ , \tag{2.31}$$

where $\tau_\lambda^{O_2}$ and $\tau_\lambda^{O_3}$ is the optical thickness of molecular oxygen and ozone, respectively. When the solar zenith angle exceeds 75 degrees (sunrise or sunset), the effect of the Earth's curvature can no longer be neglected and the secant must be replaced by the so called Chapman function $Ch(\chi)$. This function not only depends on the zenith angle χ but also on the altitude at which the absorption occurs. The Chapman function represents the ratio of the total amount of the absorbing species along the zenith angle (χ with respect to the vertical) versus the amount of total of the absorbing species in the vertical. The definition of the Chapman function occurs with the optical thickness

$$\begin{aligned}
\tau_\lambda(z,\chi) &= \sigma_{a,\lambda}\int_{-\infty}^s n(s')\,ds' \\
&= \sigma_{a,\lambda}n(z)H(z)\,Ch(x,\chi)
\end{aligned} \tag{2.32}$$

and for the Chapman function $Ch(x, \chi)$ results

$$Ch(x, \chi) = \frac{\int_{\infty}^{s} n(s')ds'}{n(z)H(z)} \ , \tag{2.33}$$

where $x = (R_e + z)/H(z)$, R_e being the Earth's radius, z the altitude, and $H(z)$ is the atmospheric scale height. For an isothermal atmosphere with the assumption that the gas has a constant scale height H, the value of the Chapman function can be estimated with the following expression [*Brasseur and Solomon* (1984)]

$$Ch(x, \chi) = \left(\frac{1}{2}\pi x \sin \chi 2\right)^{1/2} \exp\left(\frac{1}{2}x\cos^2 \chi\right) \left[1 \pm erf\left(\left(\frac{1}{2}x\cos^2 \chi\right)^{1/2}\right)\right] \ . \tag{2.34}$$

$$+ \ sign : \chi \geq \frac{\pi}{2}, \quad - \ sign : \chi \leq \frac{\pi}{2}$$

The Chapman function also depends, in addition to the zenith angle, on the relation between the total altitude $(R_e + z)$ and the constant scale height. For $\chi = \frac{\pi}{2}$, corresponding to sunrise or sunset, a simplified form results for the Chapman function

$$Ch(x, \pi/2) = \left(\frac{\pi x}{2}\right)^{1/2} \ . \tag{2.35}$$

For a detailed deduction of the Chapman function see, cf. [*Risbeth and Garriott* (1969), *Brasseur and Solomon* (1984)].

2.4 UV Absorption Characteristics of Molecular Oxygen and Ozone

Solar photons are absorbed in the stratosphere and mesosphere primarily in the ultraviolet wavelength region and to a lesser extent in visible, near infrared, and X-ray wavelength regions. Therefore the absorbed energy produces electronic, vibrational and rotational excitation, molecular dissociation, and ionisation, but ionisation is of only minor importance for the middle atmosphere. At altitudes below about 60 km, these processes are closely balanced by local recombination and collisional de-excitation, thus most of the absorbed energy is thermalised, which means a local realisation as heat.

Absorption of ultraviolet radiation by atmospheric molecules like molecular oxygen and ozone, can induce transitions into electronically excited states which may then photodissociate. Dissociation occurs primarily in continuous spectra, while excitation of electronic, vibrational, and rotational energy takes place in spectrally complex bands composed of large numbers of lines. Furthermore, dissociation can also arise from absorption in complex spectral bands provided these are at wavelengths shorter than the threshold wavelength of dissociation. The process of dissociation results in the formation of new species and the excitation process, which may occur at the same wavelength as well, results in a change in the electronic or other energy level of the constituent. So absorption of ultraviolet radiation by atmospheric molecules can induce transitions into electronically excited states which may then photodissociate. The concept of absorption cross section refers to the ability of a particular molecule to absorb a photon of a particular wavelength. It does not

refer to an actual area size, even though it has units of area. In this case, the absorption cross section conveys the probability of interaction between light photons of a given energy and the oxygen or ozone molecules.

The Beer-Bouguer-Lambert law describes the absorption of a ray of incident intensity at a given wavelength passing through a layer containing an absorbing species. The variation of intensity is proportional to the absorption coefficient, this coefficient is therefore proportional to the concentration of the absorbing particles. The absorption cross section defines the absorption behaviour of the absorbing species. The absorption cross section is the sum of all the separate cross sections for processes that are possible, resulting from a single photon absorption event the wavelength of the absorbed photon. Absorption of ultraviolet radiation by molecular oxygen and ozone leads to excitation as indicated in the spectrum by absorption lines and by electronic bands consisting of many lines due to vibrational and rotational energy levels. Since the energy of the photon must match the energy difference between the lower and the upper energy level, the absorption occurs at discrete lines or bands in a narrow range of wavelengths.

A illustrative potential energy diagram is shown in Fig. 2.7, where the two displayed curves representative the ground and excited states of a diatomic molecule. Maximum stability results at the minimum in the potential curve, that represents a stable bound configuration of the molecule. Due to absorption of a high energy photon, the electron configuration changes to an excited state whose potential energy is represented by the upper curve. The amount of energy due to transition is given by the difference between the two minima. The vibrational levels are shown as well, denoted by the horizontal line in the potential. The potential energy versus internuclear distance is shown for the ground electronic state X and the first electronically excited state A. For each of these states, the potential energy first decreases and then increases with internuclear distance, corresponding to electrical forces that are repulsive at close range and attractive at longer range on either side of a stable equilibrium point. Further, the potential energy becomes independent of distance for larger separations.
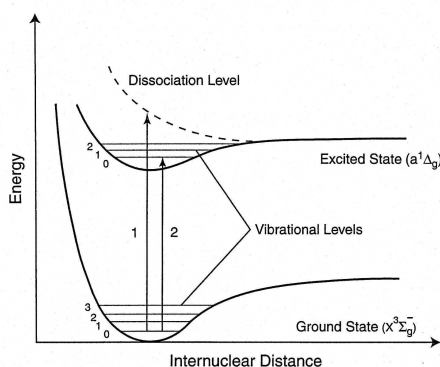
Figure 2.7. Simplified potential energy diagram for two electronic states of a diatomic molecule. The horizontal lines in the potential represent the vibrational energy levels (adapted from [*D.G. Andrews* (1987)].

Photodissociation is indicated in a spectrum by continuous absorption over an extended range of wavelengths. In contrast to excitation, which is indicated by absorption at discrete wavelengths, the absorption due to photodissociation occurs in an absorption continuum.

For a continuum, the transition is not between two well defined energy levels but between a specific lower energy level and any energy greater than the threshold energy for a given process. This means in practice that many different processes may occur together in the same wavelength region, with discrete absorption in lines of bands overlapping one or more continua.

Further the vibrational energy levels contains an internal structure, each level is subdivided into a number of rotational energy levels. The spacing of these levels is too small to be shown in Fig. 2.7 and therefore transitions such as (1) and (2) are multiple and are associated with a series of spectral lines.

Also the dissociation thresholds for both states are illustrated, for the X state, dissociation into two ground-state atoms results, while the threshold for the A state corresponds to dissociation into one or more electronically excited atoms. As the vibrational energy levels increase, the vibrational oscillation energies increase until the dissociation threshold is reached. The transitions, indicated by the slanting arrows in Fig. 2.7, represent (1) the absorption of a photon to produce a transition from one vibrational level to a higher one of the X state, (2) absorption producing a transition from one vibrational energy level of the X state to the first level of the A state, (3) absorption producing photodissociation to two ground-state atoms, and (4) dissociation producing one excited state and one ground state atom. The energy changes associated with the dissociations are continuous, the discrete energy changes associated with transitions between vibrational energy levels produce discrete spectral bands. However, for molecules with identical nuclei, like molecular oxygen and ozone, photon absorption does not occur for transitions from one vibrational energy level to higher one.

Photodissociation results in the severing of chemical bonds and the production of neutral dissociation products $XY + h\nu \rightarrow X + Y$ where both X and Y may be in excited states (electronic, vibrational, rotational) and they can have excess kinetic energy. Usually the products in excited states are much more reactive than in the ground state. Photodissociation is possible at all wavelengths less than the threshold corresponding to the least energetic photodissociation process for the molecule in question. Since the absorption occurs over a continuous range of wavelengths, photodissociation leads to continua in the cross section curve. The difference in energy between that possessed by the absorbed photon and the energy levels of the products is taken up in the kinetic energy of the products. Photoionisation is of minor interest for middle atmospheric examinations and will not considered anymore in this thesis.

2.5 The Molecular Oxygen UV Absorption System

Oxygen plays a key role in the chemistry of the Earth's atmosphere. The splitting of the molecular oxygen bond by ultraviolet solar radiation is the primary step in the formation of ozone. The penetration of solar radiation into the Earth's atmosphere depends on the absorption by each constituent of the atmosphere. The radiation below 100 nm is almost completely absorbed above 100 km by molecular and atomic oxygen, and by molecular nitrogen, only X-rays of wavelength less than 1 nm penetrate to the middle atmosphere. At wavelengths greater than 100 nm, solar ultraviolet radiation can photodissociate atmospheric molecules. At longer wavelengths, the solar spectrum is subdivided into regions of absorption by the principal absorbing species, molecular oxygen and ozone. Molecular oxygen absorbs only the radiation at wavelengths less than 242.4 nm, while ozone,

abundant in the stratosphere, absorbs primarily between 200 nm and 300 nm, but also to some extent in the visible and infrared. Oxygen is a key molecule in photochemistry of atmosphere.

Photoabsorption determines the altitude region where solar radiation is deposited and the transmission of ultraviolet in the atmosphere. Therefore, photon cross sections are required for a quantitative understanding of the atmosphere. The energy levels and associated equivalent wavelengths of atmospheric constituents provide the framework for understanding photon interactions and chemical reactions in the atmosphere. The cross section, the number density relative to other absorbers, and the availability of significant photon flux at the altitude in question are determining the importance of any specific process at any specific place in the atmosphere.

At the ultraviolet wavelengths where radiation interacts with molecular oxygen and ozone, the radiation produces continuous bands of absorption in connection with photodissociation of molecules. Figure 2.8 shows the general shape of the spectral distribution of the absorption cross section of molecular oxygen. In the Herzberg continuum at wavelengths between 242 nm to 200 nm, molecular oxygen is dissociated into two ground-state oxygen atoms. Considering shorter wavelengths, from 200 nm to 175 nm, the absorption spectrum is superposed by the discrete Schumann-Runge bands. Molecular oxygen is vibrationally excited in these bands. Also these excited bound states are unstable and eventually produce two ground-state oxygen atoms. Each of these vibrational bands in the Schumann-Runge system are comprised of rotational lines. Wavelengths between 175 nm and 135 nm are absorbed in the Schumann-Runge continuum, in which molecular oxygen is dissociated into two oxygen atoms, one electronically excited. Absorption at still shorter wavelengths exhibits an irregular banded structure, the atmospheric window region in the molecular oxygen absorption spectrum, which extends from about 130 nm to the ionisation threshold at about 102 nm. It consists of many strong, diffuse absorption bands coupled with regions between the bands of low absorption. The regions of low absorption are called atmospheric windows, because high energy solar ultraviolet radiation can penetrate to lower altitudes than would be expected from averaged cross sections at these wavelengths. The contribution marked Lyman α is due to emission by atomic oxygen in the Sun's spectrum. Due to a coincidence with a minimum in the oxygen absorption spectrum, Lyman α radiation penetrates relatively far into the atmosphere.

The absorption by individual bands varies strongly with altitude. For the Herzberg continuum the smallest values of the absorption cross section result, therefore the Herzberg continuum dominates absorption by molecular oxygen up to 60 km because shorter wavelengths have already been removed at higher altitudes. The Schumann-Runge bands dominate the absorption in the mesosphere from about 65 km to 90 km. The Schumann-Runge continuum becomes more important than the Schumann-Runge band absorption at about 90 km and above, therefore the Schumann-Runge continuum prevails only in the thermosphere, where very energetic ultraviolet radiation is present.

2.5.1   The Molecular Oxygen Schumann-Runge Absorption System

The Schumann-Runge bands of molecular oxygen are of central importance to the photochemistry of the terrestrial atmosphere. Photodissociation of molecular oxygen in the Schumann-Runge bands is a fundamental driver of ozone formation in the middle atmosphere, while Schumann-Runge band opacity controls the atmospheric penetration of solar vacuum ultraviolet radiation. The Schumann-Runge system is characterised by a banded
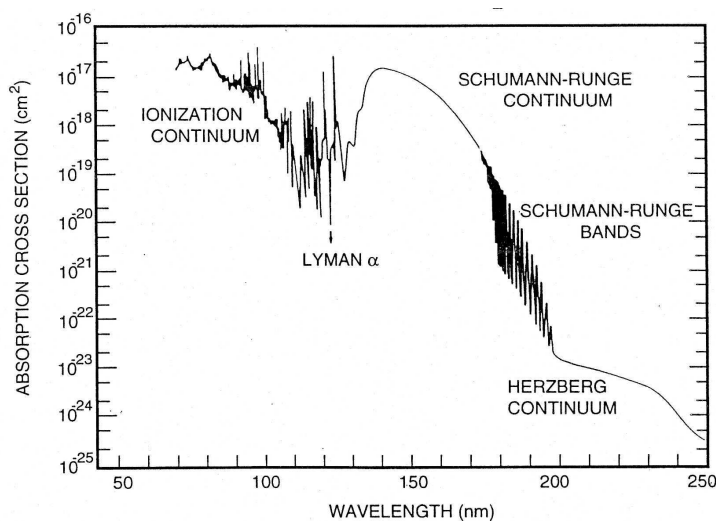
Figure 2.8. UV absorption spectrum as a function of photon wavelength for molecular oxygen (adapted from [*Brasseur and Solomon* (1984)]).

structure from 174 nm to 204 nm and a continuum from 137 nm to 183 nm. As described in Section 2.2.1, absorption of ultraviolet radiation produces (1) transitions from one vibrational energy level of the ground electronic state to the first vibrational energy state of the first electronically excited state, (2) absorption induces photodissociation to two ground-state atoms, and (3) dissociation produces one excited state and one ground state atom. For molecules with identical nuclei, like molecular oxygen, photon absorption does not produce transitions from one vibrational energy level do another energy level in the same electronic state.
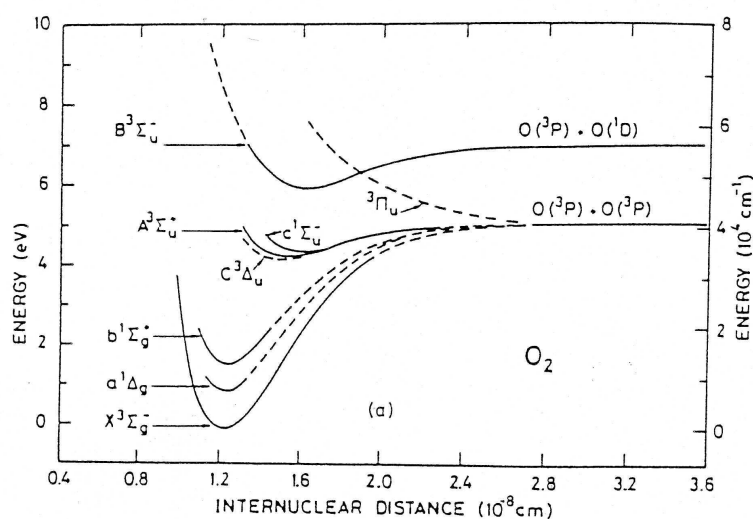
Figure 2.9. Simplified potential energy diagram for molecular oxygen (adapted from [*D.G. Andrews* (1987)]).

These relationships between the energy levels are illustrated in Fig. 2.9, which shows

the potential energy diagram of molecular oxygen. The potential energy for the electronic energy levels of molecular oxygen are shown, including their *term symbols*. Also omitted in this plot are the vibrational and rotational levels. The term symbol specifies the electronic configuration and indicates the ordinal number of the level in a series of terms having the same multiplicity (series X, A, B,..., or series X, a, b,...). Further the multiplicity indicates by the superscript number, which is determined by the net electronic spin with integer quantum number S, corresponding to the number $(2S+1)$ of sub states distinguished by different spin orientations. The Greek letter in the term symbol corresponds to the net orbital angular quantum number in the sequence Σ, Π, Δ..., analogous to atomic orbital angular momentum quantum number symbols (S, P, D,..). The subscripts that follow indicate terms whose wave functions are symmetric or antisymmetric on reflection $(+,-)$, the superscripts indicate even parity (g) or odd parity (u).

These term symbols contain further information about *allowed* and *forbidden* transitions. The allowed transitions can occur, if there is a change of the dipole moment between the two participating terms. These electronic dipole transitions have relatively large cross sections. For absorption (or emission) of radiation other types of change in the electronic
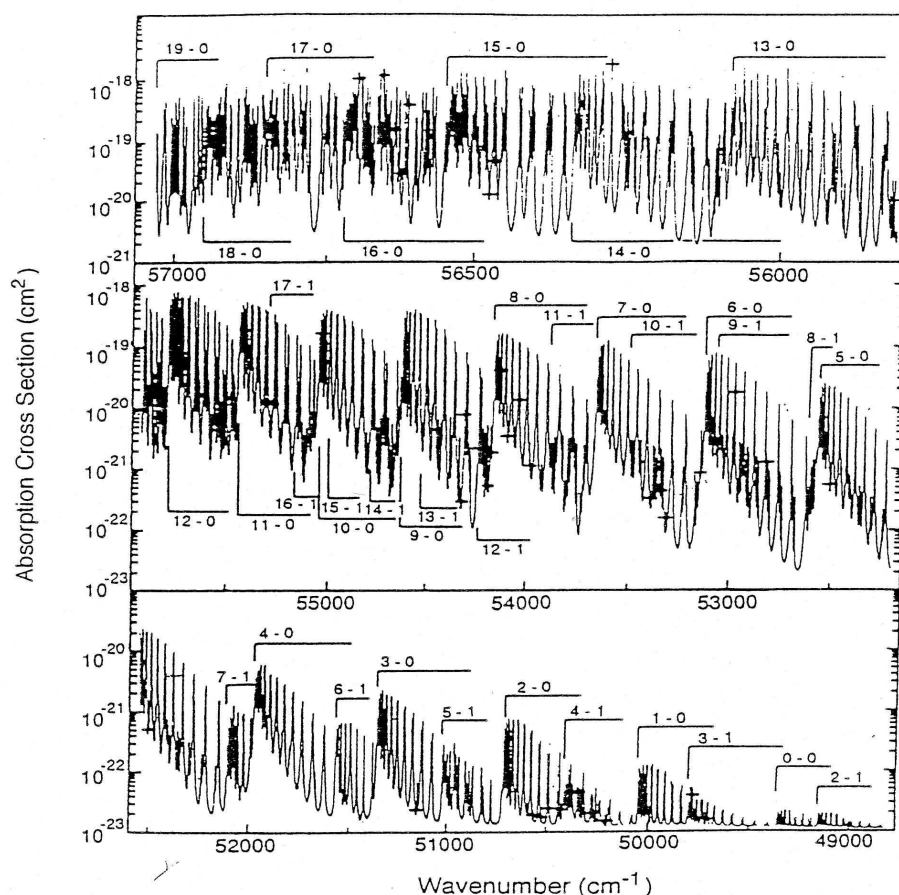
Figure 2.10. Spectral distribution of the absorption spectrum of molecular oxygen in the Schumann-Runge band (adapted from [*D. G. Andrews* (1987)]).

configuration of the molecule can obey. This can be, for example, electronic quadrupole or magnetic dipole changes. Such transitions have typically smaller cross sections than electronic dipole transitions by six orders of magnitude or more and, furthermore, such transitions are included in the category of forbidden transitions. Due to *selection rules*, derived from quantum mechanical theory of the terms, results a distinction between allowed and forbidden transitions. For example, spin change in a transition is forbidden or changes other than $\pm$ or 0 in the total angular momentum quantum number are forbidden (cf., e.g., [*Mitter* (1993)]). For the Schumann-Runge bands, the allowed transition $X^3\Sigma_g^- \to B^3\Sigma_u^-$ is responsible for the strong bands between 175 nm and 204 nm. The Schumann-Runge continuum extends to shorter wavelengths and corresponds to the dissociation $O_2 \to O(^3P) + O(^1D)$, in which one oxygen atom emerges in the excited ^1D state. However, molecules in the upper term Of the Schumann-Runge bands, the $B^3\Sigma_u^-$ state, can undergo a spontaneous transition to the $^3\Pi_u$ state.

This state is unstable due to the missing potential energy minimum, therefore results a rapid dissociation into two oxygen atoms in the ^3P ground state. This transition is a predissociation, a result of this process is, that the lifetime of molecular oxygen in the $B^3\Sigma_u^-$ state is exceptionally short. Figure 2.10 shows the detailed spectral distribution of the absorption cross section of molecular oxygen in the Schumann-Runge bands. The rotational line structure of the vibrational bands is illustrated, including the vibrational levels which are involved in the transition. For example, (1-0) corresponds to rotational lines in the transition between the first excited vibrational level of the B state and the ground vibration level of the X state. The Schumann-Runge band system shows a regular appearance at longer wavelengths, because there exists a regularity of the spacing of vibrational and rotational energy level. At shorter wavelengths, the number of lines from incommensurably overlapping bands become so great, that the spectrum has a disordered, almost random appearance. The absorption cross section varies by about four orders of magnitude between 175 nm and 204 nm. The Schumann-Runge bands can be considered to begin at the (1,0) band, which is a weak absorption feature at 204 nm. The absorption cross section in the region down to the onset of the continuum at about 175 nm are dominated by the higher vibrational states of the band system [*Murtagh* (1988)].

2.5.2 Temperature Dependence of the Molecular Oxygen Schumann-Runge Absorption System

The complex Schumann-Runge spectrum of molecular oxygen results in the absorption of solar ultraviolet radiation over a wide range of altitudes. Thus, proper description of this process requires knowledge of absolute photoabsorption cross sections over a range of wavelengths and temperatures. The Schumann-Runge band region is of central importance of the absorption of solar radiation by oxygen. Absorption by molecular oxygen in the Schumann-Runge bands occurs predominantly in the mesosphere and upper stratosphere. The Schumann-Runge absorption system shows a relatively strong temperature dependence. The temperature dependence results from changes both in the *Boltzmann population distribution* and in the Doppler line widths (see Section 2.2.1), but the Boltzmann effect is much more dominant. However, the band strength for absorption is proportional to the ratio of the number density of molecules in the lower state of the transition to the total number density of molecules of the absorbing gas. This ratio is called the Boltzmann population distribution and is directly proportional to the factor $h\nu/kT$, therefore

it depends directly on the temperature of the absorbing gas. Because these factor is large for vibrational transitions, the relative strengths of bands with different lower state vibrational quantum numbers are extremely sensitive to temperature. Also the differences in energy between rotational levels are much smaller, therefore the temperature sensitivity of the ratios of line strengths within the band is much less, so the overall envelope of the rotational lines within a single vibrational band is controlled by temperature.

Because of the structured nature of these absorption bands, wavelengths near band minima penetrate deeper into the atmosphere than wavelengths near band maxima. Further, the single bands show a inhomogeneous temperature dependency regarding to the wavelength dependent absorption cross sections. Near the band minima, the temperature dependence is much more intensive than near the band maxima, where the temperature dependence is almost not noticeable. This situation is shown in Fig. 2.11, which illustrates the strong temperature dependence of the absorption cross sections of molecular oxygen between 185 nm and 204 nm. However, the molecular oxygen absorption cross section in the Schumann-Runge absorption system decreases with decreasing temperature. In order
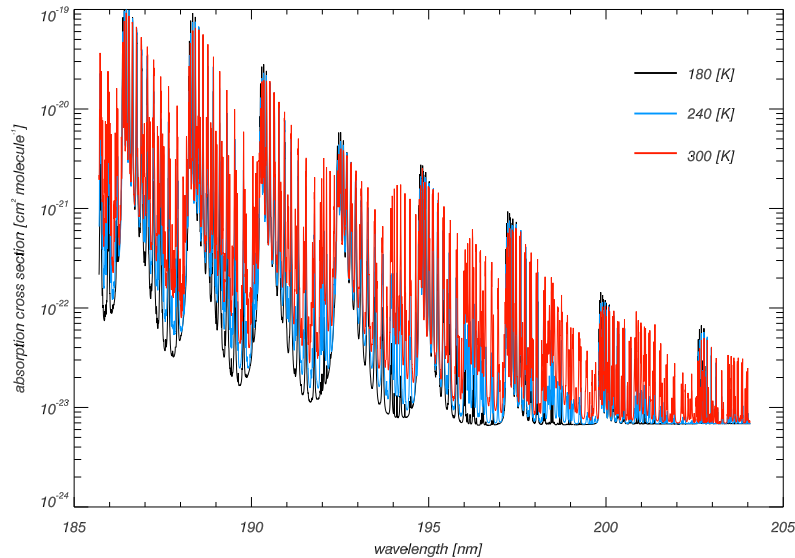
Figure 2.11. Temperature dependent molecular oxygen absorption cross section in the Schumann-Runge absorption system between 185 nm and 204 nm as a function of wavelength. The dark, blue, and red lines corresponds to temperatures of 180, 240, and 300 Kelvin respectively (data taken from http://cfa-www.harvard.edu/amdata/ampdata/cfamols.html#toO2).

to study atmospheric photochemical processes, it is necessary to have access to high resolution photoabsorption cross sections [*Nicolet et al.* (1988b)]. As it is impossible to obtain experimental cross sections for the full range of relevant atmospheric conditions, a adequate form of Schumann-Runge band modeling is required. This has involved the development of line by line models. The high resolution, temperature dependent molecular oxygen cross sections used in this thesis are calculated from the polynomial model of K. Minschwaner [*Minschwaner et al.* (1992)] including the Herzberg continuum cross section in the range 49000.5 cm^{-1} to 52000 cm^{-1} (calculated with coefficients after [*Yoshino et al.* (1988)]).

The non-homogenous temperature dependence in the Schumann-Runge bands as well

as the width of the particular bands are important factors for the selection of the ultraviolet spectrometers bandwidth. With oversized spectrometer bandwidths, a proper determination of the molecular oxygen atmospheric density (as well the atmospheric temperature which can be determined from the oxygen density) is not possible. Earlier studies showed that a spectrometer bandwidth < 2 nm is required to obtain data with sufficient accuracy.

A detailed study about the Schumann-Runge absorption system is give by, e.g., [*D.G. Andrews* (1987), *Yoshino et al.* (1992), *Nicolet and Peetermans* (1980), *Brasseur and Solomon* (1984)].

2.5.3 The Molecular Oxygen Herzberg Absorption System

Because of the large number density of oxygen compared to ozone, the molecular oxygen Herzberg absorption system is important in atmospheric absorption, even though the cross section is small relative to the ozone cross section in the Hartley band region. The molecular oxygen Herzberg system comprises the wavelength region between 185 nm and 242 nm (cf. Fig. 2.8), the Herzberg continuum, where discrete bands make a negligible contribution, and between 242 nm and 260 nm, the Herzberg bands (the Herzberg bands are not shown in Fig. 2.8). At wavelengths less than 242 nm, the cross-sections increase monotonically, all the way to 200 nm. The latter region produces very weak absorption bands and at 242 nm dissociation to two ground-state oxygen atoms (O^3P) results. At these wavelengths, the bands terminate in a weak continuum, which extends to still shorter wavelengths, the Herzberg continuum. The Herzberg bands are important in regions of the atmosphere where the ozone absorption can be relatively weak, such as near the surface (cf., e.g., [*Trakhovsky et al.* (1989a), *Trakhovsky et al.* (1989b)]).

The Herzberg continuum is the region of near-threshold dissociation of molecular oxygen to give $O(^3P)+O(^3P)$. The electronic configuration of the oxygen atoms leads to a considerable number of electronic states of the O_2 molecule, and a ground state $X^3\Sigma_g^-$ that is unusual in that it has two unpaired electrons. In the Herzberg continuum, absorption occurs from the ground state X state to the excited $A^3\Sigma_u^+$, $A'^3\Delta_u$, and $c^1\Sigma_u^-$ states. These states are called the Herzberg I, II, and III transitions, respectively. The excitation of molecular oxygen in the Herzberg continuum is a complicated process, since many electronically excited states and spin-orbit and orbit-rotation couplings amongst them are involved. The Herzberg transitions are electric dipole or spin forbidden, and the absorption cross sections are weak. Absorption cross section within continuum is less than cross section for allowed transitions by a factor of 106-107. The outcome of these is that ozone becomes the dominant attenuator of incoming solar radiation in the 210-300 nm wavelength region. The temperature dependence of the Herzberg continuum cross section of molecular oxygen is negligible over the range of temperature found in the Earth's atmosphere [*Cheung et al.* (1986)].

The Herzberg continuum dominates absorption by molecular oxygen up to about 60 km (see Section 2.2.2), due to the smallest values of the absorption cross section of molecular oxygen, therefore shorter wavelengths have been already removed at higher altitude. However, the Herzberg continuum leads to not less than 60% of the molecular oxygen photodissociation at the stratopause level for an overhead Sun to about 90% in the lower stratosphere [*Nicolet et al.* (1988a)].

The molecular oxygen absorption cross sections in the Herzberg continuum used in this thesis are taken from [*Cheung et al.* (1986)]. More information of the molecu-

lar oxygen Herzberg absorption system can be found in [*Brasseur and Solomon* (1984), *Yoshino et al.* (1988), *Hall and Anderson* (1991)].

2.5.4 The Ozone Hartley Absorption Band

Stratospheric and mesospheric ozone shields the Earth's atmosphere from solar ultraviolet radiation. The UV absorption by ozone primary occurs in the continuous Hartley band, which is located from 200 nm to 310 nm. The absorption reaches a maximum in the 250 nm region and decreases with shorter wavelengths. For wavelengths less than 200 nm, the ozone absorption of solar ultraviolet radiation is usually unimportant compared to the dominant molecular oxygen absorption. In this wavelength region, the absorption by ozone is related to the existence of large bands superimposed on a continuum, but this spectral region is unimportant in the photochemistry of the middle atmosphere because these wavelengths are absorbed by molecular oxygen at higher altitudes. Stratospheric ozone prevents all solar radiation at wavelengths less than about 280 nm reaching the surface of the Earth. The near UV absorption spectrum of ozone in the Hartley band is shown in Fig. 2.12.
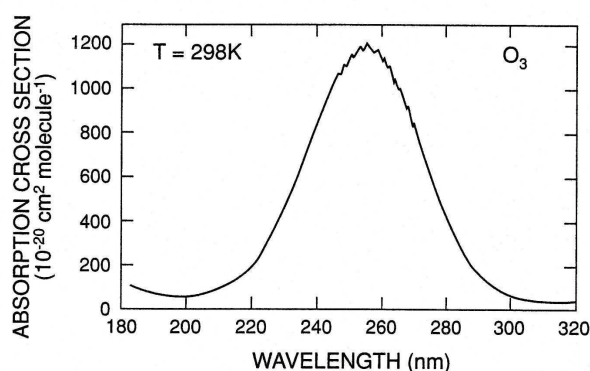
Figure 2.12. UV absorption cross section of ozone as a function of wavelength at 298 K in units of cm^2 (adapted from [*Molina and Molina* (1986)]).

Primarily the ozone absorption begins near 360 nm, in the spectrum a group of diffuse bands results called the *Huggins* bands. These absorption cross sections are temperature dependent and the bands are superimposed on weak continuous absorption. In the Huggins bands, the absorption dissociates ozone into molecular oxygen and atomic oxygen, both products in their ground states. For wavelengths less than 310 nm the Hartley band region begins. In the Hartley band it becomes possible to produce an oxygen atom in the electronically excited state $^1D_2$ and the associated molecular oxygen in the first singlet state $a^1\Delta_g$, thereby results the allowed transition

$$O_3(X^1A_1) + h\nu \rightarrow O_2(a^1\Delta_g) + O(^1D_2) \ .$$
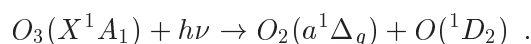
However, there is no significant temperature dependence of the cross sections in the Hartley band over the range of temperatures found in the Earth's atmosphere (expect near the longwave end). The very important fact of these electronically excited state of the oxygen atom is for the atmosphere that it has sufficient energy to undergo an exothermic reaction with ground state molecular oxygen leading to the regeneration of ozone.

55

The absorption ozone cross section data used in this thesis are adapted from [*Molina and Molina* (1986)]. More information about the ozone Hartley absorption system can be found in, e.g., [*Huffmann* (1992), *Molina and Molina* (1986)].

3   Atmospheric Remote Sensing

The field of atmospheric sciences, which includes chemistry, physics, and meteorology, is dependent on observations. It is not possible to reproduce in a laboratory all the chemical reactions and motions of air that occur in the real atmosphere. This means, that numerous observations must be made on many different time and size scales. The time or temporal scales can range from a few minutes to many decades. The size or spatial scales can range from under one kilometer to thousands of kilometers, indeed, to the entire world (e.g., satellite measurements). Therefore, observing the atmosphere requires a diverse set of measurement tools. These tools take the form of different sorts of instrumentation. Where to operate the instrument depends what component of the atmosphere has to be observed. Measurements can be made from space, balloons, aircraft and the ground.

The knowledge on the distribution of atmospheric parameters like temperature, pressure, and such important trace gases as ozone was limited decades ago to data from the worldwide radiosonde network, extending no higher than about 30 km, from a limited number of rocket profiles, and from some balloon and aircraft measurements obtained in connection with special experiments. None of them provided truly global coverage. This situation changed radically in the late 1960s with the advent of satellites carrying sensors capable of sounding the middle atmosphere (cf. [*Elachi* (1987), *Huffmann* (1992)]).

Measurements form the base of the analysis and the understanding of the atmospheric composition and structure. Observables of concentrations or atmospheric constituents can be made *in situ* or remotely. Measurements provide the information for testing models and validating theoretical concepts. The two types of measurements involve different techniques. *In situ* measurements are made at the exact instrument position (on the portion of the atmosphere that is located at the instrument). Typically parameters measured with *in situ* instruments are meteorological data, such as temperature and wind, but also the concentration of atmospheric constituents, such as ozone and several trace gases. Remote sensing refers to instrument-based techniques used in the observation of spatially distributed information about an object, doing this by applying recording devices not in physical, intimate contact with the medium (thus at a finite distance from the observed target, in which the spatial arrangement is preserved). A general examination of the remote sensing technique can be found in [*Huffmann* (1992), *Rees* (2001)].

3.1   History of Remote Sensing – an Overview

The measurement of atmospheric parameters from a distance is generally called remote sensing. This defines the study of the Earth's atmosphere from above, by the use of instruments on artificial satellites. Thereby the instrument making the measurement is far from the point at which the measurement is being made. The remote sounding technique

involves the detection and measurement of electromagnetic energy after it has been modified by the part of the atmosphere of interest. The fact, that the flux intensity arriving at the instrument is generally a function of many unknowns, makes the interpretation of such measurements difficult. Before it reaches the detector, the radiation may have been scattered, reflected, absorbed, and remitted several times, each time in a way that is characteristic of the composition, temperature, and pressure of the atmospheric gas.

The technology of remote sensing started with the first photographs in the early nineteenth century. Remote sensing above the atmosphere originated at the dawn of the space age (both Russian and American programs). The power and capability of launch vehicles was a big factor in determining what remote sensors could be placed as part (or all) of the payload. Smaller sounding rockets were developed by the military in the mid of the last century. These rockets, while not attaining orbit, contained automated still or movie cameras that took pictures as the vehicle ascended. The first non-photo sensors were television cameras mounted on unmanned spacecraft and were devoted mainly to looking at clouds. The first U.S. meteorological satellite launched into orbit on 1960 used vidicon cameras to scan wide areas at a time to generate weather maps. During the '60s, the first sophisticated imaging sensors were incorporated in orbiting satellites. At first, these sensors were basic TV cameras that imaged crude, low resolution black and white pictures of clouds and Earth's surface, where clear. A significant advance in sensor technology stemmed from subdividing spectral ranges of radiation into bands (intervals of continuous wavelengths), allowing sensors in several bands to form multispectral images. In the early 1970s, the first unmanned satellites specifically dedicated to multispectral remote sensing were developed to monitor the Earth's surface.

The development of non-photographic remote sensing technology progressed rapidly after the first mapping satellite, LANDSAT1, was put in orbit in 1972. The development of artificial satellites in the latter half of the 20th century allowed remote sensing to progress to a global scale. Instrumentation aboard various Earth observing and weather satellites such as LANDSAT, the Nimbus and more recent missions such as ENVISAT or CHAMP provided global measurements of various data for civil, scientific, and military purposes.

There are many types of satellites used for remote sensing of the Earth. The three major types are atmospherical, oceanographic, and terrestrial satellites. Atmospherical satellites are used to obtain information about the Earth's atmosphere, oceanographic once to obtain data about the Earth's oceans and other water bodies. Terrestrial satellites provide data about the Earth's land surface. The range of the electromagnetic spectrum allows researchers to see the Earth from a different perspective.

3.2   Observational Data

Measurements form the base of the understanding of the effectiveness of the complex climate system or how atmospheric processes proceed. Data provide the information for testing models and validating theoretical concepts. Using observations together with the balance equations makes it possible to investigate the mechanism by which the various processes occur in the atmosphere. Also the magnitude of some of the external constrains of forcings can be deduced from atmospheric data. The main sets of observations of the atmosphere can be grouped into *in situ* surface and upper air data, and remote sensing data.

In situ measurements involve direct sampling of the atmosphere. A sample of the atmosphere is brought into the instrument and is analysed for its properties. This can involve the use of mass or optical spectroscopy, chemical assays, or observation of how intense light interacts with the molecules inside the sample. These techniques can be employed either from ground, aircraft, or balloon platforms. A global network of ground-based stations provides local meteorological parameters, such as pressure, temperature, specific humidity, or cloud cover. Actually more than 7000 stations furnishes weather data. The stations are mainly located in western Europe, the United States, and some parts of Asia. To obtain a vertical distribution of, e.g., temperature or specific humidity, radiosondes can be used. These are balloon-borne instruments that measures the meteorological quantities at various altitudes, transmitting data back to Earth via radio signals. Balloon-borne instruments have also been used for measuring the ozone concentration (ozonesondes) or stratospheric aerosol profiles of number density and size distribution. Since the second world war, the number of reporting stations grow up from a few hundred to about 1000 stations, mainly distributed over North America, Europe, and Asia, which provides daily data. The data coverage over the inhabited regions of the continents is sufficient for the purpose of long-term-scale climate research. On the other side, extensive regions without data are found over the oceans or the Antarctica. In this regions only a few radiosonde measurements are taken regularly. Each radiosonde ascent measures the temperature, pressure, and humidity with high vertical resolution from the ground to about 20 km to 30 km altitude. Therefore, the entire troposphere and lower stratosphere can be covered by *in situ* measurements. Balloons are seldom used above 40 km, because the low air density limits the payloads even for large balloons. For sampling the atmosphere above this layer rockets are in use, measurements are taken by the instruments when they descent trough the atmosphere with a parachute.

An advantage of *in situ* measurements is the high resolution of the data, also samples can always be taken at the same spatial region. This makes long-term trend studies easily possible. Such measurements are often considerably cheaper and easier to realise than remote sensing measurements. However, the scientific output of the experiment is relatively limited, and *in situ* measurements are very localised. Some regions of special scientific interest are not covered very well. Anyway such measurements are essential for the validation of remote sensing data. Data assimilation systems still use temperature data extracted from radiosonde experiments.

The second method to collect atmospheric data, the so called remote sensing technique, is differentiated to *in situ* measurements.

Remote sensing is characterised by the fact, that measurements of information of an object are done by a recording device that is not in physical or intimate contact with the object. Remote sensing applications can be found in ground-based, in balloons, aircraft, and spacecraft systems. Table 3.1 shows some important methods of measuring various compounds by *in situ* and by remote sensing measurements.

Satellite sensors are a powerful tool for atmospheric research and satellite remote sensing became the most advanced technique in Earth observation. Actually remote sensing measurements by satellites are the main input into weather and climate models. The relevance of data provided by satellite based measurements in climate research has expanded greatly since the early 1960s when cloud pictures were the only useful data product. Measurements of the net incoming and outgoing radiation flux on top of the Earth's atmosphere were one of the first reliable measurements of these fundamental driving force of

Compound	In Situ Methods	Remote Sensing Methods
H_2O	Frost point hygrometer, Lyman-α absorption	IR and microwave spectroscopy, Raman lidar, filter spectroscopy
O_3	UV absorption chemiluminescence	UV, IR, and microwave spectroscopy, LIDAR
O_2	mass spectroscopy	UV and IR spectroscopy
NO	chemiluminescence	IR spectroscopy
NO_2	photolysis, chemiluminescence	IR and visible spectroscopy
HCFC, HFC	tunable diode laser	IR spectroscopy
NO_x	chemiluminescence	UV spectroscopy
Cl, ClO	resonance fluorescence	microwave spectroscopy

Table 3.1. *In situ* and remote sensing methods for measuring important atmospheric species (cf. [*Brasseur and Solomon* (1984)]).

the climate system. Satellite measurements are providing useful information from different spectral bands like the ultraviolet, visible, and infrared bands. But also information from other spectral bands can be used for atmospheric studies. For example, the microwave band is used for investigations about precipitable water and liquid water content of the atmosphere. Another example is the determination of the nature and concentration of aerosols in the atmosphere using backscattered ultraviolet radiation. The remote sensing method provides an excellent global coverage with cycles of two or three days for sampling the same region. However, the measured data are always scattered over hundred of kilometers in the horizontal and over several kilometers in the vertical. Remote sensing methods needs numerical inversion systems, where indirect measurements of parameters of interest are to be retrieved.

3.3 Basics of Atmospheric Remote Sensing

Remote sensing is differentiated from *in situ* measurements by the fact that the location of the measurements is different from that of the instrument. Atmospheric remote sensing requires that information be propagated by electromagnetic radiation from the atmosphere to the instrument. The radiation is characterised by a specific wavelength, which interact with some physical aspect of the medium. The instrument measures the radiation, from this measurement characteristics of the atmosphere can be deduced. This process is known as retrieval and requires the use of fundamental light scattering and radiative transfer theories. The information may be contained in the intensity, spectral distribution, or polarisation of the received signal.

There are two basic types of remote sensing, called *active* and *passive* remote sensing. Active remote sensing involves interacting with the radiation in the atmosphere that has already been changed by the presence of the parameter in question and measuring the response. Active systems employs a radiation source generated by artificial, the emitted signal corresponds to a specific wavelength and is sent to the atmosphere. A part of the emitted radiation is scattered back to the detector. That signal can be analysed and the atmospheric composition or rather the structure with which the signal has been modified by absorption or scattering can be retrieved. Radar is one example of active remote

sensing. Passive remote sensing utilises naturally occurring radiation, which is mostly radiation coming from the Sun (e.g., UV, IR, and visible) or the Earth-atmosphere system (e.g., thermal radiation or microwave). Stellar and lunar signals can also be measured but whose disadvantage are relatively small signal intensities.

A multiplicity of techniques have been used to scan the Earth's atmosphere from space. Instruments are viewing along limb (horizontal) ray paths, nadir (downward), or a hybrid combination of viewing geometry, for both occultation and emission experiments. The two basic types of remote sensing (active and passive sounding) can be further divided into following fundamental categories: absorption, emission, refraction, and scattering experiments. In a absorption experiment, radiation after propagating the atmosphere along the line of sight is measured. The radiation source is usually the Sun, but the Moon, stars, and several man made transmitters in the radio or radar wavelength region are also be used. Solar occultation is used by, e.g., the Atmospheric Trace Molecular Spectroscopy Experiment (ATMOS) [*Farmer* (1987)]. It measures the solar radiation after it passes through the atmosphere at sunrise or sunset and provides stratospheric measurements of many chemical species like N_2 or CO_2. Another satellite experiment concerned with stratospheric chemistry is the Stratospheric Aerosol and Gas Experiment (SAGE) (cf., e.g., [*Chu et al.* (1989), *McCormick et al.* (1989), *Fussen et al.* (1998), *Fussen* (1998)]). The SAGE instrument measures sunlight through the limb of the Earth's atmosphere in seven spectral wavelengths (from 0.385-1.02 μm). The measured sunlight, which was scattered and absorbed by trace gases and aerosols, is converted into vertical profiles of ozone, water vapor, nitrogen dioxide, and aerosol concentrations. Another example for absorptive remote sensing is the Solar Monitoring and Atmospheric Sounder (SMAS), the far most treated and in detail discussed occultation instrument in this thesis. The SMAS sensor concept exploits (cf. Section 4.1) solar occultation data to retrieve profiles of ozone and temperature (cf., e.g., [*Rehrl* (2000), *Rehrl and Kirchengast* (2004)]). Another important instrument is the Global Ozone Monitoring by Occultation of Stars (GOMOS) instrument. GOMOS uses stellar occultation data to retrieve atmospheric constituent profiles like ozone (cf., e.g., [*Retscher* (2004)]).

In an emission experiment, the radiation emitted by the atmosphere is observed and the sensor measures the spectral characteristics and intensity of the emitted radiation. An example instrument is the Infrared Atmospheric Sounding Interferometer (IASI). IASI is a spaceborne instrument intended to measure the humidity distribution of the atmosphere. This is done by spectrometry at infrared wavelengths from 3.6 μm to 15.5 μm. It will obtain improved atmospheric profiles of temperature and humidity in the troposphere and lower stratosphere and provide additional information on a range of other geophysical parameters, including atmospheric ozone and some trace gases (cf., e.g., [*Weisz* (2001), *Schwärz* (2004)]).

Refractive occultation experiments are characterised by the path delay of the signal due to a refractive atmosphere (cf. [*Tarayre and Massonnet* (1996)]). The path delay depends on the refractive index profile of the atmosphere and on the angle of incidence of the ray. This refractive index profile depends essentially on altitude but it depends, to a lesser extent, on the climatic and meteorological conditions of the atmosphere. Refractive occultation monitoring makes use of occulting navigation signals of the GPS (Global Positioning System) constellation they pass through the atmosphere and are intercepted by a GPS receiver on a Low-Earth-Orbit satellite. The highly accurate measurements permit the derivation of vertical profiles of the temperature, pressure, and humidity in the

middle atmosphere, as well as profiles of electron content in the ionosphere. An example of the radio occultation technique is the Challenging Minisatellite Payload (CHAMP) mission, managed by GFZ Potsdam ([*Wickert et al.* (2005b)]). Another powerful concept of the refractive occultation technique is the Gravity Recovery and Climate Experiment (GRACE), providing tropospheric and stratospheric data of temperature, pressure, and humidity (cf., e.g., [*Beyerle et al.* (2005), *Wickert et al.* (2005a)]).

In a scattering experiment, solar radiation scattered within the Earth-atmosphere system is observed. The signal backscattered from the Earth's surface, or from particles (cf. aerosols) in the medium between the Earth's surface and the instrument is measured. An example is the Total Ozone Mapping Spectrometer (TOMS) concept. TOMS senses the total stratospheric ozone column, utilising the strong absorption by ozone in the ultraviolet region. The atmosphere scatters the UV radiation from the Sun strongly. The combination of scattering and absorption allows the determination of the ozone amount from the spectrum of the radiation returned to space (http://toms.gsfc.nasa.gov). The source of radiation is usually the Sun, but experiments with scattering instruments can also be done with man made signals by active systems.

3.4   Solar Occultation

Occultation methods have been used for many years to provide accurate measurements of species concentrations of planetary and terrestrial atmospheres. The technique is ideal for monitoring trends of species of global change. Absorptive occultation instruments measure solar, lunar, and even stellar radiation directly though the limb of the atmosphere during satellite Sun, Moon, and star rise and set events. By measuring the amount of absorption of radiation through the atmosphere at different wavelengths (e.g., UV, visible, or infrared), occultation instruments can infer the vertical profiles of a number of trace constituents.

The solar occultation technique is a very simple method to measure vertical profiles of atmospheric constituents using the Sun as light source. An occultation occurs when one body blocks the view of another, while an eclipse occurs when a body disappears because the light from the sun has been prevented from reaching it by a second body. The Sun is observed as it tracks through the atmosphere, and concentrations of gases in the atmosphere are inferred from the degree of absorption in selected spectral channels. As the spacecraft orbits the Earth, the receiver instrument points toward the Sun and measures its intensity. Before each sunset starts, the line of sight between the spacecraft and the Sun is unobstructed by the atmosphere so that the Sun's intensity as measured by the receiver instrument is unattenuated. When the satellite starts to dip below the horizon so that the line of sight passes through a portion of the atmosphere, the Sun's intensity will be attenuated due to aerosols and gases in the atmosphere that scatter and absorb sunlight.

During sunrise events, when the satellite moves from the dark towards the sunlit side of Earth, the Sun is first viewed through the atmosphere, and then along an unobstructed path when the satellite rises above the horizon. Thus, the measurement sequence during sunrise is just the reverse of that during sunset. This is carried out at a series of tangent heights, increasing in altitude during a sunrise or decreasing in altitude during a sunset. From each of the atmospheric measurements a slant column can be calculated which can contain contributions from multiple atmospheric layers. The slant columns contain

sufficient information that when combined and inverted, one can obtain a profile of the atmosphere.

3.4.1 Advantages and Disadvantages of the Solar Occultation Method

The theoretical study of Hays and Roble (cf. [*Hays and Roble* (1968a), *Roble and Hays* (1972)]) demonstrated that the absorptive occultation method is a very useful concept for remotely sensing the atmosphere. To separate the various atmospheric species, measurements at specific wavelength bands at high spectral resolution are needed. The principle of solar occultations is similar to those of classical absorption spectroscopy. Absorption spectroscopy is an important technique for determining the composition and number density of constituents in the middle atmosphere [*Hinteregger* (1962)]. The intensity data measured during occultation are then used to obtain information about the absorbing species in the atmosphere. The absorption spectrum of a mixture of gases is fully diagnostic of the composition, although some gases are much more difficult to detect than others. In an occultation event, many spectra are obtained as a function of the height at which the atmosphere is traversed, and the vertical distributions of individual gases can be obtained. The intensity of the Sun, in certain atmospheric absorption bands, is monitored by a satellite tracking the Sun during Earth's atmosphere crossing. One advantage of the solar occultation technique is the improved vertical resolution. The ratio of the atmospherically attenuated radiation to the unattenuated radiation measured outside the atmosphere provides the atmospheric transmission at specified wavelengths as a function of height. Thereby profiles of various trace gases in the atmosphere can be retrieved. The vertical resolution of measurements from a absorptive occultation instruments is typically about one to two km.

Another advantage is the so called self-calibration of these systems (this applies to all absorptive occultation methods). Absorptive occultation is generally based upon relative measurements. The same instrument is used to measure the attenuated and unattenuated radiation. Therefore long-term instrument changes disappear for the ratio of these two measurements which is ideal to study atmospheric trends. Recapitulating, the main advantages of solar occultation measurement technique are self-calibration and good vertical resolution.

The main disadvantage of the solar occultation method is the weak global coverage. Low Earth orbiting satellites makes approximately 14 circulation in one day, therefore theoretically 28 occultations results (14 sunrises and 14 sunsets) [*Rees* (2001)]. Lunar occultation show the same number of possible occultations. With the stellar occultation technique a good daily global coverage of measurements can be obtained, because there are possible target stars in all directions when the satellite is in polar orbit.

Compared to stellar occultations, solar occultations yields to a higher signal to noise ratio due to higher signal intensity of the Sun. This allows very accurate retrieval results and provides high sensitivity (precision) measurements because it uses the bright Sun as a light source. The disadvantage of stellar occultations is the low intensity of the targets which is the most limiting factor for stellar occultations. The stellar fluxes compared to the constant solar flux are relatively weak. The signal collecting telescope for stellar methods has to be large in order to gain the signal. Solar occultations are generally immune to the effects of atmospheric emissions. But in the lower atmosphere with higher refractive impact, stellar occultations have the advantage that the refractive effects can be treated more easily for stars as a point source than for the Sun which is an extended source. The

rays of the stellar radiation hitting the detector are parallel, the stars are practically at infinite distance.

The occultation technique works best for a point source, then the vertical resolution at the tangent point is very sharp [*Hays and Roble* (1968a)]. A point source affords maximum resolution. For the Sun as a finite source, the light rays emitted from the lower and upper limb can have tangent ray heights separated by about 25-30 km when observed from satellite altitude. This complicates the problem, the inversion of full solar disk occultation data represents special problems. This results because the apparent size of the Sun, as seen by the detector, is generally large compared to the local atmospheric scale height [*Atreya et al.* (1984)]. So a single measurement therefore consists of light received from widely separated ray paths and will collectively sample a region of the atmosphere. In general, the solar occultation requires an integration over the finite source to generate the transmission profile [*Hays and Roble* (1973)]. For a proper designed instrument like the SMAS sensor, a minimisation of the problem of the extended size of the source can be solved by viewing only a small fraction of the solar disc (e.g., for the SMAS sensor results a width of ≤ 2 km).

One advantage of the Sun as a light source is its brightness, therefore no lack of photons for detection results. Also the spectrum is complete down to the very shortest wavelengths. Therefore the dissociation continuum absorption by various constituents can be used. The variation of intensity across the solar disk is quite variable, there are a few areas that are many times brighter than the rest of the disc. When the data from this kind of source are analysed and modeled assuming a uniform Sun, an underestimated atmospheric temperature can result if there is only one primary hot spot with the rest of the Sun being very dim. For wavelengths above about $\sim$50 nm, the Sun has a very granular structure with a highly random distribution of these hot spots. In this case, when it is applicable for the SMAS concept the errors made in assuming a uniform Sun are negligible [*Smith and Hunten* (1990)], especially also since the fraction of the solar disk viewed focus the disk center.

3.4.2 Techniques for Solar Occultation

Over the past 20 or more years, solar occultation satellite instruments have played an important role in Earth observation by providing accurate and stable measurements of aerosols, ozone, and other trace constituents in the middle atmosphere and upper troposphere. The possibility of using the Sun or stars as light source for extinction experiments was shown in 1968 by Hays and Roble [*Hays and Roble* (1968b)]. The instrument concept for solar occultation experiments originated as a hand-held, single wavelength sunphotometer (Stratospheric Aerosol Measurement or SAM) which has flown onboard an Apollo mission in 1975 [*Pepin and McCormick* (1976)]. Solar occultation satellite missions providing important contributions to Earth observation like the Stratospheric Aerosol Measurement (SAM) II from 1978-1993 [*McCormick et al.* (1981)], or the Stratospheric Aerosols and Gas Experiment (SAGE) series (cf., e.g., the pioneering work about the solar occultation technique for stratospheric investigations reported by [*McCormick et al.* (1979), *McCormick* (1987), *Wang et al.* (1992)]). Another example for solar occultation is the SCIAMACHY experiment onboard the ENVISAT satellite (launched in 2002), using an imaging spectrometer whose primary mission objective are global measurements of trace gases in the troposphere and in the stratosphere (cf.

http://envisat.esa.int/). The solar radiation transmitted, backscattered and reflected from the atmosphere is recorded at relatively high resolution. Yet another solar occultation experiment is the Solar Occultation for Ice Experiment (SOFIE) onboard the Aeronomy of Ice in the Mesosphere (AIM) satellite, scheduled for launch in September 2006 (cf. http://aim.hamptonu.edu/). The objective of this experiment is to study polar mesospheric clouds (PMCs) and the environment in which they form. The SOFIE channels are designed to measure gaseous signals to dedicate PMC measurements and temperature.

Solar occultation experiments providing densities for a number of species in the Earth's atmosphere (cf., e.g., [*Atreya* (1981), *Roscoe et al.* (1994)]). Occultation is the principal method of probing other planets atmospheres. Smith and Hunton [*Smith and Hunten* (1990)] demonstrated in a review the use of the absorptive occultation technique for studies of other planetary atmospheres. The investigation of the atmospheres of planets like Jupiter, Martian, Saturn, and Uranus was primarily based on remote sensing techniques.

Extinctive Solar Occultation

Two types of occultation techniques have been used for decades, which is the extinctive and the refractive measurement. Both techniques can be used to determine the composition and structure of the atmosphere of the Earth, other planets, and their satellites. In each case, radiation from the Sun (the source of the radiation could be a star or the Moon too) interacts with the atmosphere, measurements of the outgoing signals are used to retrieve atmospheric parameters like temperature or atmospheric constituents density profiles.
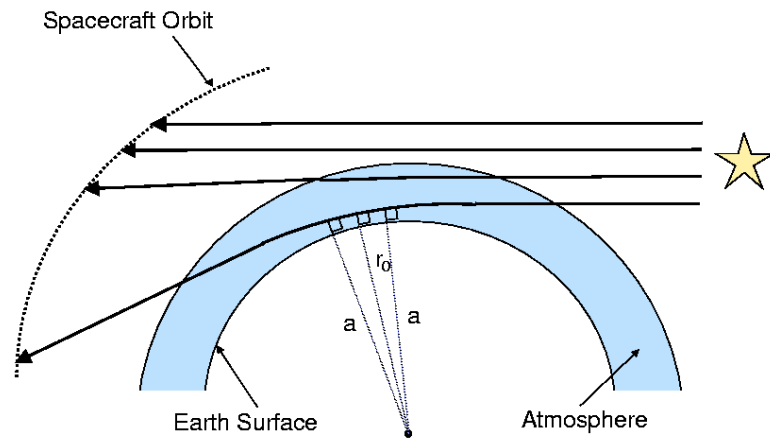
Figure 3.1. Geometry for solar occultation observations of atmospheric parameters as function of tangent height r_0. On top of the atmosphere the rays coming from the Sun are not bended, with decreasing height the bending of the rays increases due to the increasing air density. The impact parameter a defines the perpendicular distance between either of the ray asymptotes and the center of curvature (adapted from [*Retscher* (2004)]).

Basically, the extinctive solar occultation technique is similar to the classical technique of absorption spectroscopy. Figure 3.1 shows the principle occultation geometry for solar occultation. The Sun utilises as signal source and a spectrometer is used as detector. The atmosphere along the line of sight acts as absorbing medium between emitter and detector.

Extinctive occultations occur when atmospheric constituents absorb or scatter incoming solar radiation. Because extinction cross sections are generally wavelength dependent, spectral measurements obtained as the Sun sets deeper into the atmosphere are diagnostic of the atmospheric composition. Constituent profiles can be further determined from the relative transmission. Absorption and scattering can be summarised by the term extinction. The extinction technique is very useful for the determination of aerosol and other minor gases in the middle atmosphere. The ratio of the occulted spectrum to the unocculted spectrum, measured above the atmosphere, is referred to as the atmospheric transmission. As a result, extinctive occultation measurements are self-calibrating and ideal for long-term monitoring of climatic trends.

The extinctive solar occultation method in the ultraviolet wavelength region is in generally limited to high altitudes due to the absorptive characteristics of molecular oxygen and ozone. Both atmospheric constituents absorb most of the UV radiation already in high altitudes before the radiation could reach low atmospheric regions. Therefore a low signal to noise ratio results in the low stratosphere and troposphere. Also ray bending and atmospheric emissions are limiting factors for the extinctive solar occultation method. The high atmospheric opacity in selected bands in the visible and near infrared wavelength region results from the strong absorption behaviour, due to electronic and vibrational processes, of water vapor and carbon dioxide. In the UV wavelength region the atmospheric opacity mainly results due to the ozone layer in the upper atmosphere.

Refractive Solar Occultation

Refractive occultations occur when density gradients in the atmosphere refract the incoming radiation, also called bending, causing it to follow curved ray paths through the atmosphere. During an occultation event, solar rays are refracted by the Earth's atmosphere towards higher densities. Because the refraction angle is directly related to the atmospheric density profile, measured refraction angles can be used to retrieve atmospheric bulk properties like temperature, pressure, and density profiles [*Ward and Herman* (1998)]. This basic approach was pioneered using Global Positioning Satellite (GPS) data. Refractive sounding of planetary atmospheres with centimeter wavelength radio signals, termed the radio occultation method, has been utilised since the 1960's to study the atmospheres of Mars, Venus, and the outer planets (cf., e.g., [*Kliore et al.* (1965), *Fjeldbo et al.* (1971)]). In the 1980's, Russian scientists employed the occultation technique for studying the Earth's atmosphere. In general, the temperature determination at high altitudes (the middle atmosphere) is limited by the accuracy of the refraction measurements.

These two methods of occultation have been used separately in the past; however, recent analysis of occultation data have shown, that they can be combined to retrieve atmospheric composition simultaneously with profiles of temperature and pressure.

3.4.3   Orbit and Occultation Geometry for Solar Occultation

Satellites applying remote sensing techniques are used to obtain global coverage of observations. Satellite experiments using the solar occultation technique have been passive remote sensing, measuring radiation from the Sun that has traversed various layers of the atmosphere. The satellite orbit as well as the orientation of the instrument with respect to the orbital plane denotes the geographic coverage of a satellite remote sensing experiment. For solar occultation Low Earth Orbit (LEO) satellites are in use. A typical orbital period

66

for LEO satellites is around 90-100 min. The orbits take the satellites over, or nearly over, the geographic poles. The rotation of the Earth means that successive orbits move the observation point around 24° of longitude. The orbital plane is not fixed in inertial space, gravitational forces from the nonspherical Earth and from effects from the Sun and Moon controls the satellite revolution. The planes orbit can be controlled and adjusted so that the period of precession is one year. Thereby the precession keeps up with the movement of the Earth in its orbit around the Sun. Thus, the LEO orbit maintains a constant relation to the Sun. This mode is called Sun-synchronous (or polar orbit) and the observation point passes a given longitude at the same two local times each day. LEO satellites are often deployed in satellite constellations, because the coverage area provided by a single LEO satellite covers a small area, and the satellite travels at a high angular velocity to maintain its orbit. Many LEO satellites are needed to maintain continuous coverage over an area.

This contrasts with geostationary (or geosynchronous) satellites, where a single satellite, moving at the same angular velocity as the rotation of the Earth's surface, provides permanent coverage over a large area. A geostationary satellite orbits the Earth directly over the equator, approximately 36,000 km up. At this altitude, one complete trip around the Earth (relative to the Sun) takes 24 hours. Thus, the satellite remains over the same spot on the Earth's surface at all times, and stays fixed in the sky from any point on the surface from which it can be observed. Satellites in geostationary orbits exhibit a constant signal and continuous coverage relationship with large area coverage between the satellite and its ground segment. Weather satellites are usually of this type.

Two viewing modes are commonly in use for atmospheric sounding: observations at nadir and limb sounding observations. In a nadir atmospheric sounding experiment a sensor views vertically downwards into the atmosphere towards the Earth's surface. Nadir viewing measurements are used to measure radiation from relatively short path length of emitting gas, against the warm background of the Earth-atmosphere system, as well as emitting thermal radiation (cf., e.g., the IASI or SCIAMACHY instrument as mentioned in Section 3.3). Nadir sounding observations showing a comparatively poor vertical resolution.

With the second viewing method, the limb sounding, significantly higher resolutions can be achieved. The solar occultation method is a typical limb sounding method and for this work the far most important instrument, the SMAS sensor concept, uses these technique. A remote sensing instrument views a defined beam or limb of the atmosphere with far longer path lengths along the line of sight (only the limb of the atmosphere is sensed). The limb view will make a tangent to the Earth's atmosphere at some point and this minimal distance to the Earth is called the tangent height. Both, limb and nadir sounding, use the Schwarzchild's equation. In the case of the limb sounding, the weighting functions peak very sharply at the tangent height because the instrument senses nothing below the tangent height and atmospheric density decreases exponentially above the tangent height. The background of the limb sounding is the cold and uniform space, contrary to nadir sounding, where the background is the hot and variable Earth surface. Limb sounding is more sensitive and allows higher vertical resolution than nadir sounding.

4 The SMAS Solar UV Occultation Sensor

The SMAS sensor concept is a part of the so called ACLISCOPE mission (Atmosphere and Climate Sensor Constellation Performance Explorer), developed in response to a Call for Earth Explorer Opportunity Missions (ESA SP-1226, *The Living Planet Programme*, 1998) by [*Kirchengast et al.* (1998)]. The description in this Chapter largely follows the [*Kirchengast et al.* (1998)] proposal. The primary ACLISCOPE mission objective is to provide fundamental atmospheric and solar data of highest quality for climate change research, especially on atmospheric change because the evolution of the Earth's climate system is increasingly influenced by human activities. This objective comprises climate analysis, monitoring, modeling, prediction, and process studies, all of which can be derived by the fundamental data of the mission, produced partially with the SMAS sensor concept. The experimental payload includes further a so called GRAS sensor (GPS/GLONASS Receiver for Atmospheric Sounding), which produces the refractive occultation data of high utility for the troposphere and stratosphere (cf., e.g., [*GRAS-SAG* (1998)]).

The ACLISCOPE mission furnishes profiles of densities, pressure, and temperature in the middle atmosphere. This part of the ACLISCOPE mission based on the SMAS sensor concept employs the solar occultation technique and is primarily aiming at mesospheric profiles. Furthermore, top of atmosphere (TOA) solar irradiance measurements can be observed at wavelengths less than 250 nm. Also profiles of refraction angle, refractivity, density, pressure, and temperature in the troposphere and stratosphere, humidity in troposphere, and refractivity and electron density in the middle and upper atmosphere can be obtained with the complementary GRAS sensor concept (uses GNSS occultation) together with the SMAS sensor concept. Both sensor concepts furnish data globally and with high vertical resolution, accuracy, and long-term stability. The space segment of ACLISCOPE consists of a constellation of six LEO satellites in two orbits, each satellite carrying a GRAS and a SMAS sensor. The added SMAS sensor provides direct Sun observations and uses the solar occultation technique (see Section 3.4.2) for atmospheric profiling from the upper stratopause upwards.

The major ACLISCOPE mission objectives are (for both SMAS and GRAS sensor concepts) (1) climate change research comprising analysis, monitoring, modeling, prediction, and process studies, and particularly also research in anthropogenic climate impacts detection and attribution, (2) atmospheric analysis and modeling and atmospheric process studies for the entire lower, middle, and upper atmosphere, (3) upper atmosphere research on both thermosphere and ionosphere including space weather questions, and (4) demonstration of these occultation sensor concept as a long-term observing system for climate monitoring, climate and weather prediction of the entire atmosphere. So the ACLISCOPE

mission could be of key relevance to the European Space Agency's (ESA) Earth Explorer Themes *Physical Climate* and *Atmosphere and Marine Environment: Anthropogenic Impacts*.

This thesis only examines the SMAS sensor concept. More information about the full ACLISCOPE mission is described by [*Kirchengast et al.* (1998)] and in [*ESA-SP-1196(7)* (1996)]. For further details on the GRAS sensor concept see [*GRAS-SAG* (1998)]. Good background knowledge descriptions related to the ACLIS-COPE mission objectives have been given by the ESA reports [*ESA-SP-1196(7)* (1996), *ESA-SP-1227* (1998)].

4.1   The Sun Monitor and Atmospheric Sounder - SMAS

The SMAS sensor concept furnishes solar occultation measurements, which explore the Earth's atmosphere from the stratopause upwards. Further is the SMAS sensor concept self-calibrating and uses an passive limb sounding technique. This means, that the SMAS sensor provides self-calibrating transmission data, which allow to accurately derive profiles of air density, pressure, and temperature as well as the densities of molecular oxygen, atomic oxygen, and ozone. Secundry density profiles of molecular nitrogen can be derived (the determination of molecular nitrogen). Furthermore, SMAS intends to continuously record the variable solar irradiance with high radiometric accuracy at wavelengths less than 250 nm, in the middle (MUV) and extreme (EUV) ultraviolet wavelengths region.

One very important asset of the SMAS sensor concept is its self-calibration, which delivers data with long-term stability. This time stability is an important feature for climate research and monitoring. For absorptive measurements like with the SMAS sensor concept, the self-calibration results since only normalised intensities are exploited instead of absolute radiance, therefore measurements from different satellites and times can be compared without any adjustment.

The SMAS sensor primarily delivers middle atmospheric data, which are data up to the mesopause, located at about 90 km, and upper atmospheric data, which are beyond the mesopause level. Furthermore the SMAS sensor delivers solar irradiance data. From the SMAS middle atmospheric data, profiles versus height for columnar content, air and ozone density, pressure, and temperature for the mesosphere result. On the other hand, profiles versus height for columnar contents and densities of molecular oxygen, molecular nitrogen, and atomic oxygen, as well as of pressure and temperature in the upper atmosphere (the thermosphere) results from the SMAS upper atmospheric data.

The SMAS sensor is technically based on developments of the Frauenhofer Institute for Physical Measurement Techniques (FIPM) Freiburg and the University of Boulder for the SNOE (Student Nitric Oxide Explorer) satellite (cf., e.g., http://lasp.colorado.edu/snoe/) with channels at wavelength less than 35 nm and from FIPM developments for the Russian-Ukrainian PHOTON mission. SNOE carries very similar silicon diode detectors as baselined for SMAS. A similar system is the one developed for the PHOTON mission, which includes channels at wavelengths less than 130 nm [*Neske et al.* (1997)]. The expansion of the measured wavelengths by 10 MUV channels between 190 nm and 246 nm is a simple modification of the existing sensors.

4.1.1 SMAS Channel Selection

Many major ACLISCOPE mission objectives as described at the beginning of this Chapter are largely possible through adding the SMAS sensor concept to the GRAS sensor, therefore the SMAS sensor senses the same and highly complementary fundamental atmospheric parameters as GRAS, but just above the GRAS high-quality region, this means from the stratopause upwards. The most relevant complementary height range is the mesosphere, but ideally the data should extend from 30 km upwards into the thermosphere. These thermospheric data are necessary for initialisation of the mesospheric data in the retrieval process.

The examination of the radiative interaction properties with the Earth's atmosphere delivers for the SMAS sensor a natural range in the wavelength region less than 250 nm, which indicates the relevant situation and shows the penetration altitude of the incident radiation). The spectral region therefore is the middle and extreme ultraviolet and the resulting spectral regions for the most needed height, ranging from 50 km to 100 km, are the Schumann-Runge bands, and the Herzberg continuum, both for molecular oxygen. For ozone sounding the lower edge of the continuous Hartley band is most suitable. The

Channel Number	Channel Wavelength [nm]	Solar origin of radiation	Main solar emission	Atmospheric species intervening in occultation
1 (EUV)	1-10	Corona		N_2,O_2,O
2 (EUV)	17-25	Corona	Fe X-Fe XII	N_2,O
3 (EUV)	29-35	Transition region	He II (30.4 nm)	N_2,O
4 (EUV)	50-65	Chromosphere	He I (58.4 nm)	N_2,O
5 (EUV)	70-90	Transition region	O II-O IV	N_2,O
6 (EUV)	110-130	Chromosphere	H I (121.6 nm)	O_2
7 (MUV)	190.00 ± 0.5	Photosphere	continuum	O_2
8 (MUV)	192.55 ± 0.5	Photosphere	continuum	O_2
9 (MUV)	203.50 ± 0.5	Photosphere	continuum	O_2,O_3
10(MUV)	204.00 ± 0.5	Photosphere	continuum	O_2,O_3
11(MUV)	204.25 ± 0.5	Photosphere	continuum	O_2,O_3
12(MUV)	206.00 ± 0.5	Photosphere	continuum	O_2,O_3
13(MUV)	210.00 ± 0.5	Photosphere	continuum	O_2,O_3
14(MUV)	222.00 ± 0.5	Photosphere	continuum	O_3
15(MUV)	234.00 ± 0.5	Photosphere	continuum	O_3
16(MUV)	246.00 ± 0.5	Photosphere	continuum	O_3
17(VIS)	300-700	Photosphere	continuum	Air

Table 4.1. The 17 SMAS sensor channels and characteristic parameters. The ten MUV channels (no. 7 to 16) are the channels of interest in this work.

relevant mesospheric channels are thus ten channels within 190 nm to 246 nm. The signal source for such occultations needs to be the Sun, because the Sun provides a sufficient and continuous signal at wavelengths < 250 nm. Also is the brightness across the solar disk ray homogenous in the MUV wavelength region. Based on a sensor analysis, the radiometric channels of the instrument are selected as summarised in Table 4.1. As the table shows,
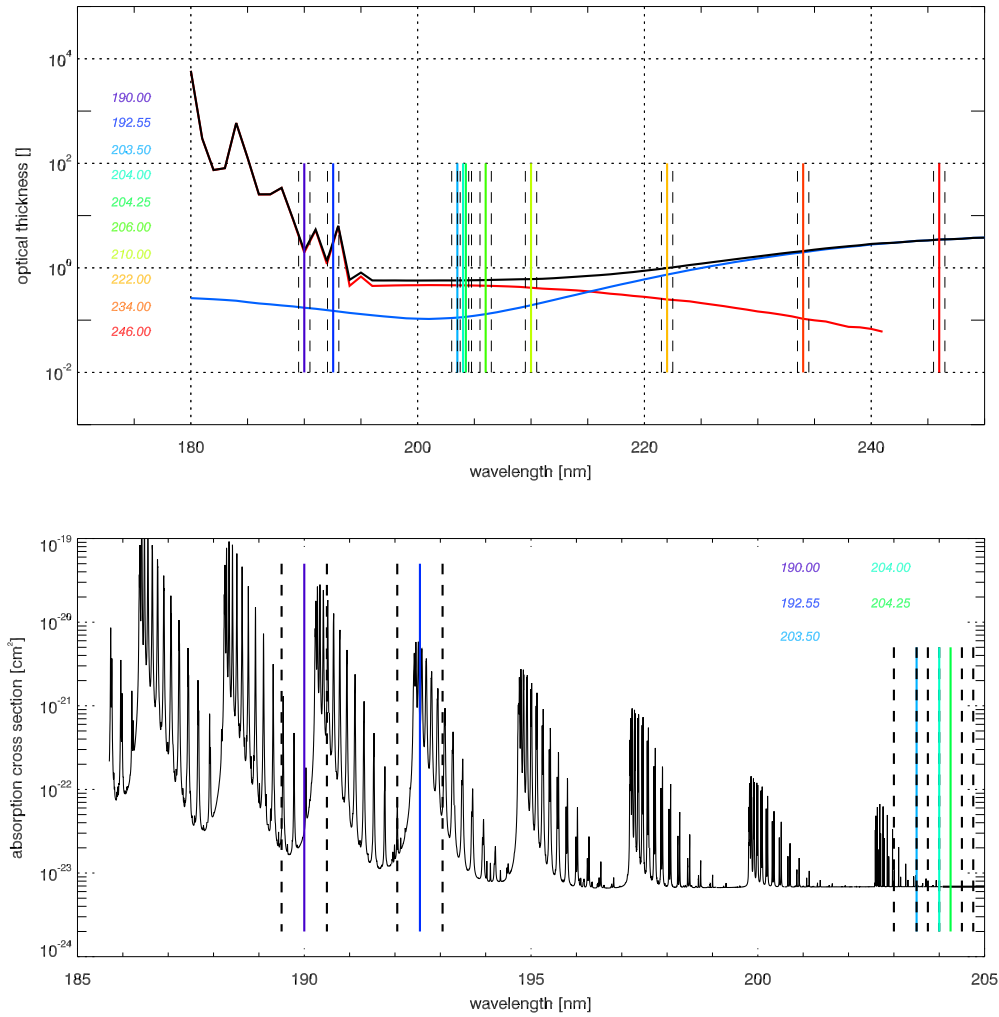
Figure 4.1. The upper panel shows the optical thickness of molecular oxygen (red line), ozone (blue line), and both (black line) at an altitude of 60 km for a temperature of 240 K. The colored vertical lines denote the ten SMAS channels in the MUV wavelength area, including the instrumental bandwidth (±0.5 nm) of the channels (dashed lines). The lower panel shows the molecular oxygen Schumann-Runge absorption cross sections at 240 K. The five Schumann-Runge channels are overplotted (colored vertical lines).

17 channels are required in total to fulfill the ACLISCOPE mission requirements. The core channels for the mission objectives are the ten MUV channels. The locations of and distances between the ten several channels are defined such, that a total coverage of the whole mesosphere is ensured. The bandwidth of the MUV channels is 1.0 nm. The visible channel is primarily for calibration purposes but this channel can also be used, in cloud free situations, for tropospheric temperature evaluation based on refractive dispersion of the occulted signal amplitude profile. The six EUV channels are primarily for thermospheric research (temperature, densities of the absorbing species); the EUV solar radiation is responsible for photoionisation at thermospheric altitudes. The selected channels were chosen to give a good signal response in the Schumann-Runge bands and

Herzberg continuum as well in the Hartley band, which is especially important for middle atmospheric ozone retrieval. The table furthermore gives some information on the source of the signal and on the intervening atmospheric species on which information is contained in SMAS occultation data. The knowledge of the density of the main atmospheric absorbing species molecular oxygen allows derivation of pressure and temperature.

The optical thickness of the absorbing species molecular oxygen, ozone, and for both in the ultraviolet region between 180 nm and 250 nm at an altitude of 60 km is shown in Fig. 4.1, upper panel. The SMAS sensor channels are drawn in, including the instrumental bandwidth of ± 0.5 nm. The lower panel shows the Schumann-Runge absorption system between 185 nm and 205 nm, where the five Schumann-Runge channels of the SMAS sensor are drawn in. Only the channels 7 and 8 lie in the band system, the three other Schumann-Runge channels lie at the upper boundary of the absorption system.

4.1.2 SMAS Instrument Characteristics

The SMAS sensor results from the SOL-ACES (Solar Auto-Calibrating EUV/UV Spectrophotometer) instrument, which covers the solar irradiance in the EUV/UV spectral range of 17-220 nm. The transmitted radiation is measured by a silicon diode detector located at the end of the absorption path and the data permits the absolute quantification of the solar flux in the prescribed spectral range [*Schmidtke et al.* (2000)]. The SMAS sensor is based on high sensitivity, high-precision ultraviolet silicon diodes, preferably, on even more precise diamond diodes. The concept core was proven on the SNOE satellite and a flight model instrument with six channels less than 130 nm and one broadband visible channel is ready for the Russian-Ukrainian PHOTON satellite (launch in late 2007) [*Kramer* (2002)]. The adaption of the available heritage for SMAS as well as the expansion of the measured wavelengths by ten MUV channels between 190 nm and 246 nm is a rather modest modification of existing sensors.

The SMAS instrument consists primarily of three components: the Sensor Arrangement, the Electronic Box, and the Sun Pointing Assembly (SPA). The SMAS instrument is baselined to consist of 17 radiation detector units, these are, in order to adapt to various different interfaces, designed as single small units (50×50×60 mm and with a power consumption of 0.12 W). On top there is a high sensitivity, high-precision UV silicon or diamond diode, the sensible area is 10×10 mm and either the diode is coated with a thin metallic film or covered by a set of two interference filters. The detectors field of view need be limited to $\frac{1}{30}$ deg for ensuring < 2 km vertical resolution. The diode current is converted by a preamplifier, this circuit corresponds to an Electrometer-Amplifier. Further is the output of the preamplifier transferred via Voltage to Frequency Converter (VFC) to the Electronic Box.

A 16 bit counter is involved toward the telemetry. The basic readout data rate is 10 Hz and can be directly used as sampling rate during occultation periods. For continuous solar irradiance monitoring a sampling rate of 0.1 Hz is sufficient. By trimming the offset of the preamplifier slightly to a positive value, no negative signal at the entrance of the VFCs results. For thermal stability the detector units are fixed on an aluminum plate. Furthermore, the temperature of the plate at the solar pointing assembly shall be as low as possible (below 30° Celsius). A variation of temperature kept less than ± 3 Kelvin during the measurement increases the accuracy of the data, therefore an electrical interface for three temperature sensors is included, providing analogue signals. In the Electronic Box, the 17 VFC science signals are stored in 16 bit counters to be transferred

to the telemetry. The Sun Pointing Assembly keeps the solar disk center continuously in the sensor field of view, with $\frac{1}{60}$ deg pointing knowledge, to ensure optimal and constant solar signal during atmospheric occultation measurements. Therefore the base plate of the SMAS sensor arrangement needs to be mounted on a sun pointing device, which offers constant sun pointing angles (within $\frac{1}{60}$ deg precision) during occultation. The SMAS sensor is a small, passive, low weight, low power, low data rate instrument and compatible with satellites of micro satellite size. The main characteristics are summarised in Tab. 4.2. The main scientific objective of the ACLISCOPE mission is climate change research.

Characteristics	SMAS Sensor
Mass	< 8 kg (total)
Power consumption	< 8 W
Max. data rate	< 2.5 kbit/sec
Total volume	< 300×200×150 mm^3
Number of channels	17 radiometric channels 1 VIS, 10 MUV, 6 EUV
Sampling rates	10/1/0.1 Hz
Precision (single indicative figure)	< 3×10^{-3} (silicon diode) < 1×10^{-3} (diamond diode) precision at 10 Hz rate
Sensor pointing accur. (towards Sun)	< $\frac{1}{30}$ deg vertical res. < $\frac{1}{60}$ deg knowledge

Table 4.2. Main characteristics of the SMAS science payload (after [*Kirchengast et al.* (1998)], slightly modified).

There are indications that tropospheric temperatures are increasing and stratospheric and mesospheric temperatures are decreasing. Atmospheric temperature are measured routinely by a global network of radiosonde stations, complemented by satellite sounding and aircraft reports. However, while efforts are ongoing to improve temporal and spatial resolution of existing systems, other techniques are useful to provide not only additional data but also atmospheric data of higher quality. Such data can be provided by the ACLISCOPE mission, involving the SMAS sensor concept (together with the GRAS sensor concept).

The primary objective is to provide with the aid of the SMAS sensor concept fundamental atmospheric and solar data for climate change research, especially on atmospheric change because the evolution of the Earth's climate system is increasingly influenced by human activities. However, indications exist that the changing thermal structure from the upper troposphere to the mesosphere is a particularly sensitive indicator of anthropogenic climate impacts. The SMAS sensor concept can furnish data to globally monitor this changing structure over the full mesosphere with very high accuracy. These solar occultation data can be used for climate monitoring and prediction, atmospheric analysis and modeling.

The main objectives for climate monitoring and prediction are to provide a global climatology of the temperature in the entire mesosphere at high absolute accuracy and vertical resolution. Further objectives are to support research into climate variability and change (inter-annual and intra-annual) and into the energetics of the climate system over the period of the mission, and thus to contribute observational input and validation of

models used to predict future trends and variability. Also in addition, for atmospheric analysis and modeling, the SMAS sensor concept can provide long, consistent sets of atmospheric states for research and model development exploiting the data of the mission together with other observations. Furthermore, a *spin-off* mission objective is that observations are provided for upper atmosphere research, e.g., for thermospheric investigations. There, observations of the densities of molecular oxygen, molecular nitrogen, and atomic oxygen, as well as pressure and temperature are provided. Also are provided direct, continuous, and accurate observations of solar irradiance for wavelengths less than 246 nm in 16 channels.

These high-utility atmospheric data can be provided with the SMAS sensor as part of the ACLISCOPE mission, which needs to be implemented as a small constellation of satellites to be able to fulfill the scientific requirements. The baseline constellation of the mission includes six micro satellites in two low earth orbits. To learn optimally about vertical and horizontal resolution properties of the occultation data, the ACLISCOPE concept includes a pair of satellites (Sat-Pair) in constellation, which furnishes the necessary experimental data for research in occultation resolution and accuracy. Particularly for the horizontal resolution studies, the availability of the Sat-Pair furnishes horizontally redundant occultation events closely related in space (distance less than 150 km) and time (separation less than 5 min). Figure 4.2 shows an indication of the the typical coverage of SMAS occultation events for the baseline. By the aid of this Sat-Pair, investigations about tandem retrieval compared to single profile retrieval are possible for example. The ACLISCOPE SMAS sensors, if implemented as baselined, can provide a data set of ∼150 occultation profiles per day in the mesosphere (and above), together with continuous solar irradiance observations for wavelengths less than 246 nm. To obtain the main objectives as described above, the ACLISCOPE baseline implementation has to be compliant with the overall requirements summarised in Tab. 4.3.

Geographic coverage with occultation events	Globally, well balanced density over all latitudes; special feature: pairwise occ. events are needed, the mean tangent points of which shall be separated < 5 min in time and < 150 km horizontally
Horizontal sampling per 6 hours	< 600 km latitudinally (in average)
Covered height range during occultation	50 km $< h <$ 400 km (all channels together) 50 km $< h <$ 120 km (10 MUV channels)
Temperature accuracy	< 2 K, within 60 km $< h <$ 90 km at 2 km vert. res.
Long-term stability	< 0.2 K/decade (temperature)
Accuracy of other occultation variables	Consistent with the required temperature accuracy
Quality direct solar data Radiometric precision Radiometric accuracy	Continuous monitoring at 10 sec sampling $< 10^{-3} (\lambda > 30$ nm); $< 10^{-2} (\lambda < 30$ nm) $< 3\% (\lambda > 130$ nm); $< 10\% (\lambda < 130$ nm)
Timeliness	< 1 day - 1 month

Table 4.3. Main requirements for ACLISCOPE/SMAS mission (after from [*Kirchengast et al.* (1998)]).

Furthermore, there exists an enormous synergetic potential of using the ENVISAT-

GOMOS stellar data together with the GRAS GNSS occultation data and the SMAS solar occultation data. Favorably, while the GRAS data have their highest performance below 30 km, the SMAS data above 50 km, the GOMOS data have their best range between 25 km and 55 km (cf., e.g., [*ACRI S.A. et al.* (1998), *Retscher* (2004)]). Therefore, the joint optimal estimate of GNSS, stellar, and solar occultation sensors GRAS, GOMOS, and SMAS, respectively, can deliver global upper air data of unprecedented climate change research utility on temperature, water vapor, and ozone with high vertical resolution and accuracy.
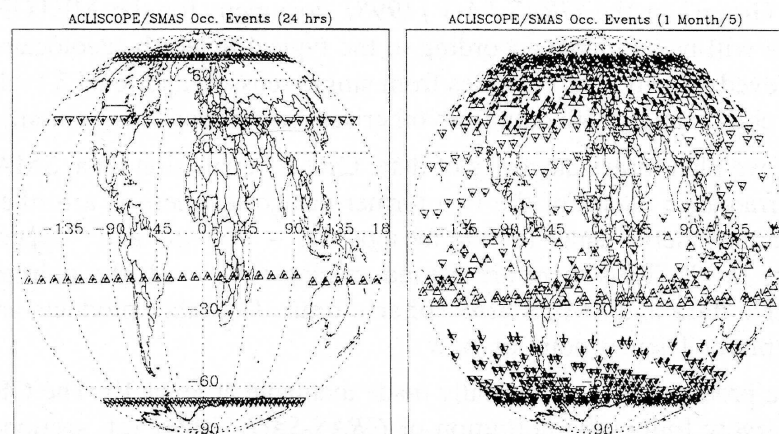
Figure 4.2. Typical coverage by SMAS occultation events for one day (left panel) and for an arbitrarily selected month (right panel; every fifth event is plotted). Sunset occultations (top down triangles), sunrise occultations (upright triangles). In time, solar occultations always happen at the terminator. During the year, governed by the Sun's declination, the somewhat peculiar monthly coverage (right panel) moves through a wide range of latitudes (cf., e.g., [*Russel et al.* (1993)]). After [*Kirchengast et al.* (1998)].

Due to its accurate fundamental data products (temperature, density, etc.), the SMAS sensor concept can enhance many other of the Earth Explorer missions planned by the European Space Agency such as an Earth Radiation Mission [*ESA-SP-1227* (1998)] or an Atmospheric Chemistry Mission [*ESA-SP-1196(7)* (1996)]. Furthermore, it is highly complementary to an Atmospheric Dynamics Mission [*ESA-SP-1227* (1998)]. SMAS also provides data for programmes of the middle and upper atmosphere and space weather community such as represented by SCOTEP (Standing Committee on the Solar Terrestrial Energy Programme) and COSPAR (Committee on Space Research). A specific programme example is the recently initiated TIGER (Thermospheric Ionospheric Geospheric Research) programme.

4.2 Mesospheric Temperature Sounding

The main scientific use areas for the SMAS solar occultation data are in the fields of climate change research. This means climate monitoring, modeling and prediction, atmospheric analysis and modeling for the upper troposphere, stratosphere, mesosphere, and in the same way for the thermosphere. The SMAS sensor concept is able to contribute these necessary data with high absolute accuracy and high vertical resolution for the entire

mesosphere and with all channels together also for the thermosphere up to about 400 km. Furthermore, a long-term stability and consistency of the occultation data results due to the self-calibration of the occultation technique, this is an important fact for climate research and monitoring (see Section 4.1).

The temperature is a key parameter to characterise the mean state of the atmosphere and its long-term evolution. The temperature structure of the atmosphere is likely to change under the impact of anthropogenic forcing such as the increase of greenhouse gases and depletion of stratospheric ozone. There are indications that stratospheric and mesospheric temperatures are decreasing and on the other hand tropospheric temperatures increase. Exactly that changing of thermal structure in the entire middle atmosphere is a particularly sensitive indicator of anthropogenic climate impacts. Also the change in aerosol concentrations influences the atmospheric structure. All these are expected to change the radiation budget of the atmosphere and thereby the Earth's climate. So a permanent observation of the temperature structure of the Earth's atmosphere is necessary.

A recent statistical analysis shows that the changing thermal structure may be a very sensitive indicator of climate trends and, in particular, the mesosphere seems to be an even better indicator of expected middle atmosphere cooling than the stratosphere. Therefore, the anthropogenic climatic impacts can be shown in particular by monitoring the full thermal structure of the middle atmosphere. The determination of the three-dimensional field of temperature in the middle atmosphere with high vertical resolution and accuracy allows an accurate climatology of atmospheric temperature to be established and long term trends to be inferred. These temperature profiles can be obtained together with the sensor concepts as described in the previous Paragraph.

Scientifically the use of the SMAS sensor concept, extending the GRAS only mission, is fully justified to open up to a global study (from day-to-day to inter-annual scales) of the atmosphere from the stratopause upwards with highest data quality and quantity. Furthermore these data can be used for a variational assimilation analysis for a consistent climatology of the entire atmosphere [*Kirchengast et al.* (1998)]. This requires advanced coupled General Circulation Models [*Russell et al.* (1995)] of the lower atmosphere (below 90 km) and upper atmosphere (above 90 km), which are basically available, though operated by different communities, for example the available ECHAM model from the MPIM Hamburg [*Roeckner et al.* (2004)]. Many different atmospheric processes may be analysed by these models supported by ACLISCOPE/SMAS data.

4.3   Mesospheric Ozone Sounding

Ozone plays a key role in supporting life at the Earth's surface by intercepting harmful ultraviolet radiation. Most of the ozone molecules in a vertical column in the middle atmosphere are found at altitudes below 35 km. Ozone is one of the main atmospheric gases absorbing solar energy, exactly in the ultraviolet wavelengths region. The positive temperature gradient of the stratosphere is due to the strong ultraviolet absorption characteristics of ozone. Therefore, a depletion of stratospheric and obviously mesospheric ozone produces a cooling of the middle atmosphere. Ozone is formed in the stratosphere and mesosphere by photochemical processes and has a maximum concentration between about 20 km and 25 km height. Furthermore, the concentration and vertical distribution of ozone vary with latitude and season, and on shorter time and space scales as well. A

reduction of the ozone concentration in the middle atmosphere will produce more harmful ultraviolet radiation at the Earth's surface.

Long-term changes in the Earth's climate, caused by changes in the abundance of radiatively active compounds in the atmosphere, like ozone, are expected to become significant during the next decades [*Houghton et al.* (2001)]. Ozone is of particular importance when viewed in the context of chemistry-climate interactions. Changes in its distribution will have the largest impact on surface temperatures when changes occur in the middle atmosphere. Observations over the last two decades show that ozone concentrations have fallen in the stratosphere and therefore also in the mesosphere. The depletion in stratospheric and mesospheric ozone levels has probably produced a general cooling of the climate system. A significant fraction of the temperature trends observed globally in the stratosphere over the last two decades could be associated with ozone depletion.

Although measurements of total ozone columns are of great importance, they are in sufficient to gain a thorough understanding of the chemical and dynamical processes determining the ozone variations. Height resolved ozone information on a global scale over an extended period of time at a reasonable temporal and spatial resolution is needed. However, for the mesosphere no sufficient ozone data exists. On the other hand, mesospheric ozone data are necessary to improve the understanding of the natural and anthropogenic influences on both, stratospheric and mesospheric ozone variation, because the mesosphere seems to be a better indicator of middle atmosphere cooling than the stratosphere (see also the previous Paragraph). The ACLISCOPE/SMAS sensor concept can provide these necessary mesospheric ozone data with high vertical resolution and accuracy. The SMAS sensor concept measures the absorption of ultraviolet radiation in the lower wavelength part of the ozone Hartley band, in the wavelength region between 200 nm and 246 nm (see Section 4.1). From these measurements normalised transmission data can be generated and the columnar content and the vertical ozone number density, respectively, then retrieved.

4.4 Thermospheric Sounding

As an enhancement the SMAS sensor concept can provide profiles on number densities of molecular oxygen, molecular nitrogen, and atomic oxygen in the thermosphere up to about 400 km height (with the six EUV channels). Also the temperature, up to the isothermal thermospheric temperature, can be provided. Therefore the SMAS sensor concept also delivers data of high quality and quantity for thermospheric research. Combined with the GRAS sensor concept, both sensors can provide simultaneously profiles of electron density and thermospheric densities (as above mentioned) and temperature. This allows to rigorously study thermospheric-ionospheric interaction phenomena, which could never be rigorously addressed before due to lack of data (cf., e.g., global gravity wave activity, magnetospheric storm processes). It opens up for robust analysis of the thermosphere-ionosphere system by numerical weather prediction assimilation methods such as classically applied to the troposphere and lower stratosphere, which is impossible so far.

The SMAS sensor concept can also furnish excellent day-to-day air drag data for geodetic research and applications like orbit modeling and prediction for LEO space platforms such as the International Space Station. Such applications currently have to rest on primarily climatological models like MSISE-90 [*Hedin* (1991)]. Furthermore, the SMAS upper atmosphere data can be a world leading asset for Space Weather applications.

The SMAS sensor concept can, besides acquiring solar occultations, provide a continuous and accurate time series of top of atmosphere solar irradiance data in the channels at wavelengths less than 246 nm, using UV spectroradiometry. This wavelength region is the spectral region with the most variable solar flux which affects the middle and upper atmosphere. This continuous solar irradiance information is a much needed input for atmospheric radiation and energy budget research. Furthermore it is also an important complement to UV/VIS/NIR top of atmosphere solar data from other sensors like, e.g., the ISSA (International Space Station Alpha) Solar Package, currently developed by the ESA, which measures the sun's electromagnetic emission over the full range from EUV to NIR and the total solar irradiance. This information is useful for questions of natural variability of solar forcing and its climate system impacts relative to anthropogenic impacts.

The continuous SMAS direct solar irradiance data in the EUV range (below 130 nm) are very useful and keenly awaited by the relevant international community. In fact, the most serious disadvantage for operating existing upper atmosphere first principles models consists in the use of proxy F10.7 data (the solar radio flux at 10.7 cm) instead of direct measurements of the EUV radiation which is the primary energy source driving the thermosphere-ionosphere system. The SMAS irradiance data can tightly constrain this input. Furthermore, these solar irradiance data are for models a highly complementary information to the SMAS thermosphere (and also to the GRAS ionosphere) profile data, this is a further boost for science for upper atmosphere research and space weather applications.

5 An End-to-end SMAS Data Processing System

Remote sounding of the atmospheric temperature and composition profiles from Earth orbiting satellites has become a technique of major practical importance for scientific observations of the Earth's atmosphere and will clearly continue to be of importance for the foreseeable future, both for the Earth and for soundings of other planetary atmospheres. In this Chapter, a method which can be used to calculate the temperature and composition of the middle atmosphere is represented from measurements of intensity of incident radiation. Such measurements can be made by the SMAS sensor concept introduced in the last Chapter. A simulation study was carried out in this thesis (for both, temperature and ozone sounding), in order to have a robust model for the application of real data. The occultation technique for determining the properties of the Earth's atmosphere using absorptive occultation measurements, bears great capability of providing profiles of atmospheric key quantities with high accuracy and vertical resolution (cf., e.g., [*Elachi* (1987), *Russel et al.* (1993), *Hays and Roble* (1968b), *McCormick et al.* (1989)]).

The intensity of the Sun, in certain atmospheric absorption bands, is monitored by a low Earth orbiting satellite tracking the Sun during occultation by the Earth's atmosphere. The intensity data during occultation are then used to obtain information about the absorbing species; in the SMAS case for the mesosphere and thermosphere (cf., e.g., [*Roble and Hays* (1972), *Roble and Norton* (1972)]). The used limb geometry is tailored to furnish a high spatial resolution, whereas the absorptive properties of the intervening medium can be related to densities of the different absorbing species. Usually, absorptive occultations have been used to measure density profiles. However, from density profiles of major species, pressure profiles can be calculated by integration, employing the hydrostatic equation. Furthermore, pressure profiles can be related, by the use of the ideal gas law, to atmospheric temperature profiles. A detailed description on error characterisation and statistics can be found in, e.g., [*Rodgers* (1976), *Rodgers* (1990), *Rodgers* (2000), *Storch and Zwiers* (1999)].

5.1 Theory of Measurements and Inverse Problems

The SMAS sensor concept uses the Sun as the source of light and the satellite photometer as detector, with the Earth's atmosphere between acting as the absorption cell. As the satellite moves in its orbit, the source ultimately is occulted by the Earth. The technique of the SMAS sensor concept uses a LEO satellite, the adapted detector measures the change in solar irradiance as the Sun is occulted by the limb of the Earth (either during sunrise or sunset). At a given wavelength, the signal emitted by the Sun is attenuated

due to the absorption by the species presented in the Earth's atmosphere, which absorb solar radiation at that wavelength. The measured transmission profile therefore contains information about the combined slant path column density of all these absorbing species. The absorption characteristic of a mixture of gases is fully diagnostic of the composition, if measured in a sufficient number of sensible selected channels.

The atmospheric parameters are coupled to the measured radiation through radiative transfer. The resulting information, which can be extracted from the measurement, is limited by the complicated nature of the radiative transfer processes and by factors concerning the measurement procedure (which includes the spectroradiometers resolution, measurement geometry, and instrumental noise). In an occultation event, the attenuated signal is obtained as a function of the height at which the atmosphere is traversed, and the vertical distributions of individual gases can be obtained. After the composition, the most basic quantity derivable from the distribution of major species is the temperature, which appears in the equation of state. The SMAS sensor concept uses the middle and extreme ultraviolet wavelengths region, this properly exploits the interaction properties of the middle atmosphere with the incoming solar ultraviolet radiation. During the occultation process, the intervening atmosphere absorbs progressively more of the light due to the strong photo-absorption features of the Earth's atmosphere.

The occultation intensity data can be related to tangential column number density profiles of the particular absorbing species, if the wavelength dependent absorption cross sections are known. This separation of the absorbing species and calculation of of tangential column number densities is called *spectral inversion*. The equation for the tangential column number density as function of the vertical number density profile corresponds to an Abel integral equation which can be inverted to determine the number density profile at the occultation tangent location. That second step in the retrieval of the vertical number density profiles from the observed intensity data, is called *spatial inversion*. Thus, the spectral inversion has to be done before the spatial inversion is accomplished by the inverse Abel transform. The SMAS sensor is a self-calibrating instrument, therefore the occultation technique involves a relative measurement with normalisation given by the measured solar irradiance above the atmosphere during each event. The following results are therefore independent of absolute instrument calibration or source strength (as large as a sufficiently accurate signal can be measured). This is a very important feature because it tends to negate the effects of instrument degradation over time. As mentioned in Section 3.4.1, the occultation technique works best for a point source. For solar occultation, where the radiation is emitted from the upper and lower limb, the problem of a finite source can be solved if measurements view only a small fraction of the solar disk.

The signals detected by occultation sensors already constitute an important data base for the monitoring of the atmosphere. Including the instrumental factors of the SMAS sensor, the wavelength and altitude dependent transmission function of the atmosphere can be calculated. This transmission function measures the optical properties of the atmosphere in the horizontal direction; it is a good measure of the transmissivity of the atmosphere which is a central property for the mesospheric ozone and temperature sounding. To proceed from the transmission functions to the distributions of the absorbing species (molecular oxygen and ozone) inversion methods must be applied. Therefore, the different absorbers have to be isolated first, based on the total transmission function. A second step deals with the retrieval of the vertical profiles such as pressure and temperature [*Retscher et al.* (2004b)].

The mathematical approach to retrieve atmospheric parameters like density or temperature can be divided into two general processes, (1) the forward model, and (2) the inverse problem. The forward problem contains a model of the radiative transfer process to calculate the normalised intensity according to Eq. 2.15. The retrieval of the atmospheric state is possible as a given sample of spectrally distributed measurements of the intensity depends on the state of the atmosphere in a known way. This allows to deduce the state of the atmosphere. Generally it can be described as an inverse problem. The inverse problem is the matter of inverting a known equation, which expresses radiation as a function of the atmospheric state in terms of radiation.

5.2 SMAS Forward Model

The intensity of the solar radiation passing the Earth's atmosphere is given by the combined attenuation of all absorbing species along the ray path and can be basically determined at each frequency using the Beer-Bougert-Lambert's law, given by Eq. 2.15. Thus, the obtained transmission profile (normalised intensity) contains information about the combined limb path column density of all absorbing species. A function like the Beer-Bougert-Lambert's law, which calculates measurable quantities based on the state of the atmosphere, is called generally *forward function*, a appropriate computer program that applies such a function is called a *forward model*. The forward problem has do be modulated in a appropriate way to solve the associated inverse problem to estimate the atmospheric parameters from the measured radiance. The description of the SMAS forward model follows mainly the work of Rehrl and Kirchengast [*Rehrl and Kirchengast* (2004)].

The atmospheric transmission T_λ is defined at each wavelength λ of interest as

$$T_\lambda = \frac{I_\lambda(s)}{I_\lambda(0)} = \exp^{-\tau_\lambda} \quad , \tag{5.1}$$

where

$$\tau = \frac{I_\lambda(s)}{I_\lambda(0)} = \int_{s_2}^{s_1} \sum_i n_i(s')\, \sigma_{i\lambda}(s')\, ds' \tag{5.2}$$

denotes the corresponding optical thickness. The normalised atmospheric transmission at any given wavelength is the ratio of the solar radiation intensity measured in the atmosphere, $I_\lambda(s)$, relative to the solar intensity above the atmosphere, $I_\lambda(0)$. The integral is carried out along a ray path s, this ray path is refracted for an altitude up to about $\sim$75 km, above refraction and therefore bending of the ray is negligible. In this context the number densities n_i and the cross sections $\sigma_{i\lambda}$ refer to the species molecular oxygen and ozone.

The estimation of the due to ray bending shifted tangent ray height is in principle calculated via solving the refractive ray path problem. The path is determined from

$$\frac{d^2\mathbf{x}}{d\tau} = n(\mathbf{x})\nabla n(\mathbf{x}) \tag{5.3}$$

with the Sun and satellite position as boundary conditions. Above 50 km height we can use a simple approximation (see below). The $n(\mathbf{x})$ denotes the atmospheric refractive index field, and $d\tau$ is the along-ray arc length divided by the refractivity index n. The

'driving field' for the ray tracing equation is the wavelength-dependent refractive index n for a neutral density ρ, given by (cf., e.g., [*ACRI S.A. et al.* (1998)])

$$n = 1 + \frac{10^{-6}}{1.00062}\left(83.4213 + \frac{24060.3}{130 - 10^6\lambda^{-2}} + \frac{159.97}{38.9 - 10^6\lambda^{-2}}\right)\frac{\rho}{\rho_0} \ , \tag{5.4}$$

where λ denotes the wavelength and is expressed in nanometers, and ρ_0 is the reference air density for standard temperature (296 K) and pressure (1013 hPa). This approximation applies a calculation without a contribution from density gradients other than the ones in the plane determined by the satellite, the Sun, and the Earth center. This can be rewritten as

$$n = 1 + 10^{-6}N \ , \tag{5.5}$$

where N is the refractivity. If the atmosphere is spherically symmetric, the bending angle α can be described as (cf., e.g., [*Kursinski et al.* (1997)])

$$\alpha = -2a\int_a^\infty \frac{d\ln n'/dx'}{\sqrt{(x'^2 - a^2)}}\,dx' \tag{5.6}$$

with $x = nr$ (r denotes the radius value) and a is a constant for a ray path, known as the impact parameter. For altitudes where ray bending is nearly negligible ($\alpha < 20$ μrad), the equation for the bending angle can be approximated as ([*Kirchengast* (1998), *Melbourne et al.* (1994)])

$$\alpha = a\,N \ . \tag{5.7}$$

The impact parameter a is given by

$$a = 10^{-6}\sqrt{\frac{2\pi(R_E + z)}{H(z)}} \ , \tag{5.8}$$

where R_E is the Earth radius, z is the value of the straight-line tangent ray height, and $H(z)$ denotes the altitude dependent scale height. The geometry of the ray bending furnish the equation to estimate the shift $\triangle z$ of the tangent ray height as follows

$$\triangle z = \frac{D_{LEO}\,D_{Sun}}{D_{LEO} + D_{Sun}}\alpha \ , \tag{5.9}$$

where D_{LEO} and D_{Sun} denotes the straight-line distance from the un-shifted tangent ray height to the LEO satellite and the Sun, respectively.

The effect of chromatic refraction [*Edlen* (1953)] for the SMAS sensor concept is negligible and therefore the refractive index of air is independent on wavelength. Chromatic refraction led to a spatial separation of rays with different wavelengths. The aberration between the several channels is very low, for instance results for the outer channels (190.00 nm and 246.00 nm) an aberration $< 5\%$. The constituent profiles vary too weakly along tangent altitude changes due to small differences of the path length for different wavelengths. Also defocusing effects can be disregarded for the realistic SMAS forward model.

Furthermore, a complete geolocation calculation is carried out, each simulated measurement of the atmospheric transmission is precisely geolocated.

The resulting modulated transmission data are based on a realistic occultation event. The satellite orbit, the shape of the Earth, the state of the atmosphere, and

the solar coordinates are the contributing factors to the geolocation. The geometry data of the event are present by EGOPS (End-to-end Occultation Sounding Simulator [*Kirchengast* (1998), *Kirchengast et al.* (2002)]), providing quasi true satellite orbits, geodetical positions of the satellite, as well as the approximated position of the Sun. The shape of the Earth is approximated by the well-known model WGS86 (World Geodetic System [*TR8350* (2002)]). The used molecular oxygen density is calculated from the CIRA-86 (Cooperative Institute for Research in the Atmosphere) database [*CIRA-86* (1990)]. The ozone density is based on AFGL-TR-86 data (FASCODE model) (cf., e.g., [*Anderson et al.* (1995)]).

Furthermore, a term for Rayleigh scattering is included. Rayleigh scattering is more important in the lower stratosphere but has also be considered in the mesosphere. A factor for the air density with the Rayleigh cross section is introduced as well. The wavelength dependent Rayleigh scattering cross section for air can be calculated at each wavelength as (cf. [*Thomas and Stamnes* (1999)])

$$\sigma_{\lambda,Rayleigh} = \lambda^{-4}\ 10^{-28} \sum_{i=0}^{3} a_i \lambda^{-2i}\ , \qquad (5.10)$$

where σ is given in [cm^2] and the appropriate coefficients a_i are listed in Tab. 5.1. The formula is applicable for wavelengths between 180 and 1050 nm. The aerosol concentration

Parameter	Value
a_0	3.9729066
a_1	4.6547659×10^{-2}
a_2	4.5055995×10^{-4}
a_3	2.3229848×10^{-5}

Table 5.1. Parameter to calculate the Rayleigh cross sections.

in the mesosphere is very low, therefore a term representing the aerosol extinction in the signal, according to Mie scattering, can be neglected. Anyway, the aerosol cross sections can be approximately calculated by Ångströms law $\sigma_{\lambda,Mie} = \frac{\sigma_0}{\lambda}$ with $\sigma_0 = 3 \times 10^{-7}$ cm^2.

In this basic work the nitric oxide photodissociation near 191 nm and 183 nm (cf., e.g., [*Minschwaner and Starke* (2000)]), initiating the primary mechanism for NO$_x$ removal in the middle atmosphere, is not considered, but should be worked out in a future refinement.

The full channel transmission T_{ch} can be modeled further as

$$T_{ch}(t_i) = \int\limits_{\triangle t} \int\limits_{\triangle v} \int\limits_{\triangle \lambda} T_{atm}(\lambda', v', t')\, W(\lambda' - \lambda_0)\, W_v W_t\, d\lambda'\, dv'\, dt'\ , \qquad (5.11)$$

where the modulated transmission results as function of time t_i, these responds to the sampling time. The basic sampling rate in case of the SMAS sensor is 10 Hz and corresponds to a vertical sampling of about 200 m. The integral is carried out over a wavelength band $\triangle\lambda$, properly covering the spectral width of each channel, the vertical field of view $\triangle v$, and the measurement integration time $\triangle t$. The SMAS field of view is pointing to the Sun center and designed 1/30 deg wide, corresponding to ~2 km vertical resolution. This limited field of view covering only a equatorial fraction of the solar disk (< 20 deg band) is useful, since the full solar disk would otherwise illuminate at any given time a height

range of 25 km to 30 km extend, severely complicating the retrieval of atmospheric profiles [*Lumpe et al.* (1991)]. The channel shape function $W(\lambda - \lambda_0)$ is modulated as normalised Gaussian function with a half-width of 0.5 nm and the resulting signal is weighted by this normed Gaussian convolution function. Furthermore, two simple boxcar functions are used, $W_v = 1/\triangle v$ ($\triangle v$ corresponds to 1/30 deg) and $W_t = 1/\triangle t$ ($\triangle t$ corresponds to 100 msec), for properly limiting the field of view and time integration domain.

For given geometry and time t_i, the atmospheric transmission file $T_{atm}(\lambda, v, t)$ can be sampled as function of wavelength, field of view, and time. By integration Eq. 5.11 the desired channel transmission T_{ch} can be obtained. For smooth atmospheric profiles adopted in this study, the two box car integrations could be well ignored and the channel transmission T_{ch} was just forward modulated for different wavelengths along a single ray arriving from the Sun center at the time t_i.
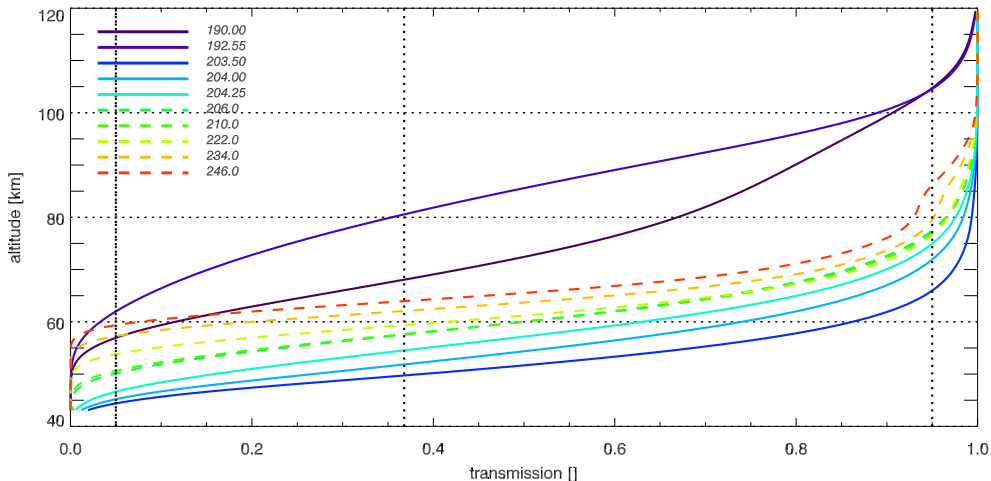
Figure 5.1. Simulated SMAS channel transmission profiles for the ten selected wavelengths forming the basis of the forward model. The solid lines show the transmission profiles in the Schumann-Runge bands and the dashed lines show the transmission profiles in the Herzberg continuum and overlapping Hartley band. The annotated numbers denote the center wavelengths of the channels. The vertical dashed lines near the left and right boundary delimit the region, within which measurements are foreseen to be exploited.

Exemplary modulated SMAS transmission data for ten channels are shown in Fig. 5.1, based on a realistic occultation event. Spherically symmetric atmospheric profiles were adopted and a scanning of the atmosphere over altitude from 120 km to 50 km was used. Transmissions for processing are only use able if they lie within a threshold of $0.05 < T_{ch} < 0.95$. The Schumann-Runge cross section data used in this thesis were taken from K. Minschwaner et al. [*Minschwaner et al.* (1992)], computed from polynomial coefficients, including the Herzberg continuum cross section in the region between 190 nm and 204 nm. Regarding wavelengths > 204 nm, the Herzberg continuum data were taken from M. Nicolet et al. [*Nicolet et al.* (1989)], the ozone cross section data from L.T. Molina and M.J. Molina [*Molina and Molina* (1986)], respectively.

For the modulated SMAS transmission profiles, the effects of scintillation and refractive dilution are not included. The forward model is only a model of the underlying physics of the measurement. The real physics could be too complex and in some aspects too uncertain

to be entire known and described. Thus the forward model should be describe the detailed physics with an adequate accuracy (cf., e.g., [*Maybeck* (1979), *Maybeck* (1982)]).

The Real Transmission: The Effects of Scintillation and Dilution

The real transmission measured by the SMAS sensor concept is not only depending on absorbing atmospheric components, additionally refraction effects impacts the measured transmission. Rayleigh scattering, as mentioned above, is already taken into account as a coefficient to the simulated transmission data. Another effect is the so called *scintillation*. Scintillation is due to spatial differences in refractive index in the atmosphere, an electromagnetic wave propagating through the atmosphere will experience fluctuations in the path length though different layers due to these. Scintillation is caused almost exclusively by small temperature variations (on the order of 0.1 - 1 K) in rather small parcels of strata of air, resulting in refraction index fluctuations. The primary reason of such small scale fluctuations is turbulent mixing of air with different temperatures. Wind motion transporting such fluctuations trough the line of sight and produces the irregular changes in intensity which are characteristic for the effect of scintillation. The effects of scintillations are always much more intensive near the horizon than near the zenith. Small atmospheric parcels of air of the order of only centimeter to decimeter produce most of the scintillation irregularities in the atmosphere.

Another effect is the so called *refractive dilution*, an effect occurring due to the change of the propagation direction of the ray while passing the atmosphere. This effect is related to the density gradient of the atmosphere. The density gradient will cause a larger deflection to a grazing ray compared to a rays with a larger impact parameter. The change of the propagation direction in the atmosphere will result to dilution of the related intensity.

Both effects, scintillation and refractive dilution, are mainly noticeable in the lower atmosphere. For the lower mesosphere, these effects can have a small impact to the measured transmission. However, in this thesis both effects are not considered for the simulation of the transmission data.

5.3   Forward Model Approximations

For an exact calculation of the transmission profiles in the highly oscillatory Schumann-Runge bands, a resolution of 500 sampling points (corresponds to 0.002 nm sampling) for each channel is necessary. Using these 500 samples of $T_{atm}(\lambda, v, t)$, Fig. 5.1 shows the wavelength-integrated channel transmission profiles. For channels > 205 nm, the absorption cross sections are smooth functions - molecular oxygen Herzberg continuum and ozone Hartley band - and 0.2 nm sampling is sufficient. The Herzberg continuum comprises the wavelength region between 185 nm and 242 nm, the Hartley band those from 190 nm to 310 nm, reaching a maximum near 250 nm. Because of the large number density of molecular oxygen compared to ozone, the Herzberg continuum is important beyond 205 nm even though the cross section is small relative to the ozone cross section in the Hartley band. The Hartley band absorption is unimportant below 190 nm. The cross sections in the Herzberg continuum and Hartley band shows a very slight temperature dependence, which can be neglected in the SMAS forward modeling.

As a result of the dense sampling needed in the Schumann-Runge bands, the rigorous forward model algorithm is fairly slow, and if used as part of an inversion algorithm a

faster algorithm is highly desirable. In order to obtain such a faster algorithm following two approximations were evaluated: the Piecewise Integration Approximation (PIA) and the Optimal Random Selection Approximation (ORSA).

5.3.1 The Piecewise Integration Approximation (PIA)

In the PIA, Schumann-Runge cross sections integrated over a prescribed number of partial channels of width $\triangle\lambda$, spread over the full spectral width of a SMAS Schumann-Runge channel, are used to compute the channel transmissions. The needed values of the Gaussian channel shape function are properly averaged as well.

More explicitly, the PIA approximates channel transmissions $T_{ch}(s)$ as follows,

$$T_{ch}(s) = \sum_{i=\triangle\lambda_i}^{\triangle\lambda_I} T_{ch,i}(s) = \sum_{i=\triangle\lambda_i}^{\triangle\lambda_I} \exp[-\int_s \bar{\sigma}(\triangle\lambda_i, T(s'))\, n(s')\, ds']\, \bar{W}(\triangle\lambda_i) \qquad (5.12)$$

with the associated averaged temperature dependent Schumann-Runge absorption cross sections $\bar{\sigma}(\triangle\lambda_i, T(s))$,

$$\bar{\sigma}(\triangle\lambda_i, T(s)) = \frac{1}{\triangle\lambda} \int_{\triangle\lambda} \sigma(\lambda', T(s))\, d\lambda' \ , \qquad (5.13)$$

and averaged Gaussian weighting function $\bar{W}(\triangle\lambda_i)$, given by

$$\bar{W}(\triangle\lambda_i) = \frac{1}{\triangle\lambda} \int_{\triangle\lambda} W(\lambda' - \lambda_0)\, d\lambda' \ , \qquad (5.14)$$

$$\sum_{i=\triangle\lambda_i}^{\triangle\lambda_I} \bar{W}(\triangle\lambda_i) = 1 \ . \qquad (5.15)$$

Both, the averaged Schumann-Runge absorption cross sections and the Gaussian weighting function are integrated over a finite equidistant wavelength region $\triangle\lambda$ for each partial channel. In turn, according to Eq. 5.13, all partial channel transmissions are integrated to yield the full channel transmission.

In Fig. 5.2 (left panel), the integrated Schumann-Runge absorption cross sections as used in the PIA (Eq. 5.13) for 100 partial channels are illustrated (0.2 nm sampling). The resulting transmission profiles for the five SMAS Schumann-Runge channels for different numbers of partial channels are shown in Fig. 5.2, right panel. The primary band structure of the Schumann-Runge bands persists to a certain degree under the PIA integration as Fig. 5.2, left panel illustrates. The right panel shows, that a sufficient number of partial channels is needed to accurately model the transmission profiles. While 25 partial channels are not yet a sufficient number, 100 partial channels appear to be an adequate number already, furnishing an accuracy of the approximated transmission of better than 1%. Compared to original 500 pins per channel this is a reduction by a factor of five of the computational cost for the sampling of the atmospheric transmission T_{atm}. The use of the PIA in a forward model embedded in retrieval algorithms is simple, straightforward, and the in this thesis used forward model approximation.
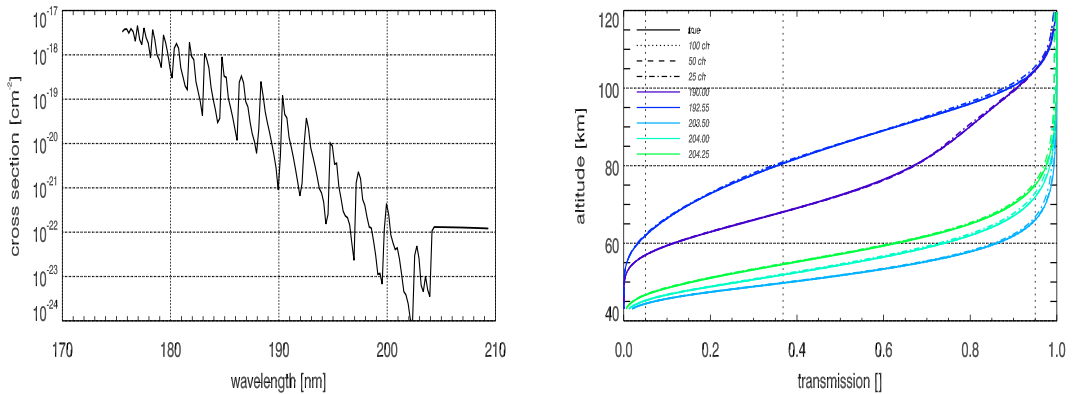
Figure 5.2. Partial integrated Schumann Runge absorption cross sections at 240 K (left panel) for 100 partial channels. The transmission profiles in the Schumann-Runge bands are shown in the right panel for full integration (true), 100 partial channels (dotted), 50 partial channels (dashed), and 25 partial channels (dashed-dotted).

5.3.2 The Optimal Random Selection Approximation (ORSA)

The idea of the ORSA is to reduce the number of sampling bins by Monte-Carlo drawing of a prescribed number of bins out of the original sample of 500 bins. Using this Monte-Carlo drawing, for which 10^4 trials were found an adequate number of trials, to reduce the 500 bins per Schumann-Runge channel to an optimal subset of 100 bins. Optimally is defined in that 100 bin subset were kept from the 10^4 randomly drawn subsets, which produces for a given atmospheric state (temperature profile) the most accurate approximated channel transmission profile compared to the exact 500-bin per channel computation.

Performing this type of ORSA for a sufficient diversity of atmospheric temperature profiles provides a number of look-up tables, which can be used in a nearest neighbor sense for a fast algorithm based on n only 100 bins per Schumann-Runge channel. A set of 18 conditions over different months and latitudes seems to be sufficient for ensuring an accuracy in approximated transmissions of better than 1% for the Schumann-Runge channels based on 100 bins. Due to the complicated handling (diversity of look-up tables, etc.) of the ORSA compared to the PIA, the ORSA is not used in the context of retrieval algorithm evaluations but rather the PIA is used as the method of choise.

5.4 Root Mean Square and Moving Average

For a realistic consideration of the SMAS forward model it is important to include the error behaviour of the SMAS sensor (a detailed discussion about the SMAS sensor characteristic is given in Section 4.1.2). The SMAS sensor concept is based on high sensitivity, high-precision ultraviolet silicon diodes (or even more precise diamond diodes). A quantity to describe the error behaviour of these diodes is the so called *root mean square* (RMS) error, also known as quadratic mean. The RMS is a statistical measure of the magnitude of a quantity, in this case radiances, and can be calculated for a series of discrete measurements (or for a continuously varying function).

The RMS error corresponds to the so called *Gaussian white noise* and was modulated as such. This describes a for any time normally (Gaussian) distributed random process. The RMS error values corresponds to the percental deviation from the noise free measured signal. White noise is generally a random process with a constant spectral density function. Hence the spectral amplitude of white noise match to $S = S(\nu)$ and the corresponding autocorrelation function is a Dirac delta function $R(t) = S\delta(t)$. Thus white noise which is uncorrelated from one time instant another [*Brown and Hwang* (1997)]. For the SMAS sensor a RMS of 0.3% at 10 Hz sampled transmission data results for silicon diode detectors and 0.1% for diamond diodes, respectively. The RMS values are determined by the developer of these diode detectors, the FIPM Freiburg. The 0.3% RMS error case is considered in the subsequent Sections of the retrieval processing.

For a better retrieval performance it is useful to smooth the transmission data. This can be done with a moving average calculation for every height step in the profile. The moving average is a simple method to smooth measured data by replacing a data point with the average (or a weighted form of it) of its neighbors. For a given sequence for one selected sensor channel, the height level i dependent transmissions $\{T_{ch,i}\}_{i=1}^{N}$ are replaced by a new sequence of smoothed transmissions $\{(T_{ch,i})_s\}_{i=1}^{N-n+1}$, defined from $T_{ch,i}$ by taking an average of subsequences of n terms, each weighted with different k_j

$$(T_s)_{\lambda i} = \frac{1}{\sum_n k_n} \sum_{j=i}^{i+n-1} k_j T_{\lambda i} \ . \tag{5.16}$$

Moving averages are in general weighted with equal weights, here the weights are defined such that $\sum_n k_n = 1$. For a chosen subsequence of $n = 5$ the weights are given with $k_n = \frac{1}{10}[1, 2, 4, 2, 1]$, where k_3 represents the weight for the original $T_{ch,i}$ before taking the mean.

5.5   The Retrieval of Atmospheric Parameters

The wavelength dependent normalised solar intensity, as measured by the SMAS sensor device aboard of a LEO satellite during occultation of the Sun by the Earth's atmosphere can be expressed by Beer-Bougert-Lambert's law. This law implies that the solar intensity attenuated due to the Earth's atmosphere can be determined by considering the combined attenuation of all absorbing species along the ray path. The ultimate aim of the SMAS sensor concept is to deduce the atmospheric properties such as profiles about the pressure and temperature, and the densities of the absorbing species, which are necessary to determinate the atmospheric temperature. For the SMAS retrieval, molecular oxygen and ozone are retrieved simultaneously, forming a joint retrieval. The expansion of the retrieval scheme by incorporating trace gases like nitric oxide (cf., e.g., [*Minschwaner and Starke* (2000)]) in the operational SMAS retrieval is possible, but is not investigated in this thesis.

Based on the well fixed forward model, an inverse connection between the measurements (normalised intensities) and the target state (the density profiles of the absorbing species, molecular oxygen and ozone) of the atmosphere has do be found. As mentions briefly in Section 5.1, a two-step method can be used. This method divides the retrieval into two separate gaits, the separation of the absorbing species and calculation of the column number densities (spectral inversion) and the calculation of the vertical number densities (spatial inversion). Hence it is necessary to establish the connection between the

tangential column number densities N_i and the vertical number densities n_i of the absorbing species. This follows from the geometry of the occultation experiment and can be performed via an Abel transform. This two-step retrieval scheme generates a line-by-line vertical retrieval, a correlation of adjacent vertical lines is not given any more after the spectral inversion.

5.5.1 Theoretical Introduction

For a given physical system, a mathematical model can be developed to describe the behaviour of the system for investigations of its structure and modes. The relation between measurement vector $\mathbf{y}$ and the actual state $\mathbf{x}$ of the physical system can be approximated by the forward model $\mathbf{F}(\mathbf{x})$

$$\mathbf{y} = \mathbf{F}(\mathbf{x}) + \epsilon \ , \tag{5.17}$$

where ϵ denotes the measurement error vector of the forward model. The forward model can be seen as the algebraic mapping of the state space into the measurement space, with an uncertainty described by the measurement error, which is often Gaussian. The quantity $\mathbf{F}$ can be a linear of non-linear function of the state vector $\mathbf{x}$. For the linear case, where $\mathbf{y}$ is assumed to be linearly related to $\mathbf{x}$, follows

$$\mathbf{y} = \mathbf{K}\mathbf{x} + \epsilon \ , \tag{5.18}$$

where $\mathbf{K}$ is the Jacobian matrix (or also called the *weighting function matrix*), which allows to determine the actual state from the measurements. For m measurements and n elements of the state vector, the Jacobian matrix is of dimension $m \times n$. For a particular measurement follows

$$y_i = \sum_{j=1}^{n} (\mathbf{k}_i)_j x_j + \epsilon_i \ , \tag{5.19}$$

where $\mathbf{k}_i$ is called the *weighting function* (of dimension n) and constitutes the ith row of $\mathbf{K}$ corresponding to the ith measurement. Therefore every single measurement in the measurement vector consists of the complete state vector, each element x_i is weighted by the corresponding element K_{ij}.

The forward function for limb sounding measurements (and indeed most other remote sounding problems) is generally not linear and the relation between measurement vector and the one to be estimated is non-linear. The problem can be linearised by expanding the forward model into a Taylor series about the initial guess profile $\mathbf{x}_0$

$$\mathbf{y} \approx \mathbf{F}(\mathbf{x}_0) + \mathbf{K}(\mathbf{x} - \mathbf{x}_0) + ... + \epsilon \ , \tag{5.20}$$

where the Jacobian matrix $\mathbf{K}$ denotes the partial derivatives of the forward model with respect to $\mathbf{x}$, evaluated at $\mathbf{x} = \mathbf{x}_0$. The mapping of sensitivity of the state vector $\mathbf{x}$, the density profile, into the measured transmission $\mathbf{y}$ is represented by the rows of the Jacobian matrix $\mathbf{K}$

$$\mathbf{k}_i = \left(\frac{\partial y_i}{\partial x_1}, ..., \frac{\partial y_i}{\partial x_j} \right) \ . \tag{5.21}$$

Numerically the Jacobian coefficients are calculated by a perturbation of the densities of the absorbing species with $\pm 5\%$ and then performing a forward model calculation, which delivers the corresponding $\mathbf{y}$. Theoretical the perturbation should be done only

at the exact tangent ray height, but for the SMAS case this delivers a too low signal response. Thus a perturbation over three adjacent heights is introduced, which furnishes a significantly higher signal and represents the basis for an accurate retrieval procedure.

Including terms of higher-order in Eq. 5.20 produces better approximations of the exact relationship between state and measurements. Nearly linear or moderately non-linear problems can ignore higher-order terms and Eq. 5.20 can be written as

$$\mathbf{y} = \mathbf{y}_0 + \mathbf{K}(\mathbf{x} - \mathbf{x}_0) + \epsilon \ . \tag{5.22}$$

Next, optimal estimation techniques can be used to deduce an estimate of the state with minimum error, assuming that the measurement error characteristic is known for the particular measuring procedure.

The measurement vector $\mathbf{y}$ contains all measurements recorded at a certain moment, the dimension corresponds to the number of channels (denoted by m) which the measurement device can record. In the SMAS temperature and ozone retrieval, this accords to ten channels in the MUV band, designated with the numbers 7 - 16 in Tab. 4.1. The particular atmospheric state, temperature and number densities of the absorbing species, at the moment when the measurement is taken is described by $\mathbf{x}$. The dimension of $\mathbf{x}$ (denoted by n) is equivalent to the number of sampling points. The Beer-Bougert-Lambert's law represents the connection between the measurement vector $\mathbf{y}$ and the state vector $\mathbf{x}$.

Limb sounding measurements are in general non-linear problems and a simple direct inversion for the state vector $\mathbf{x}$ is not feasible. A direct inversion in the case $\mathbf{K}(\mathbf{x}) = \mathbf{K}\mathbf{x}$ would result in

$$\mathbf{x}_{rs} = \mathbf{K}^{-g}\mathbf{y} \ . \tag{5.23}$$

The operator $\mathbf{K}^{-g}$ denotes the general inverse matrix and $\mathbf{x}_{rs}$ corresponds to the retrieved state (cf., Tab. A.A.1). Generally for limb sounding at high altitudes low signal-to-noise ratios results. Such problems (like also the SMAS case) are ill-posed and Eq. 5.23 cannot be used directly but a solution can be found by inserting sensible *a priori* information. Therefore the forward model function $\mathbf{F}(\mathbf{x})$ has to be approximated in a way which is suitable for the considered situation.

The *Bayesian approach* is a more general way to solve such noise perturbed problems with minor but reliable information about the behaviour of the state. The Bayesian approach deals with an investigation of the propagation of conditional probability densities. Inaccurate prior information can be quantified as a probability density function (*pdf*) over the state space, on the other hand inaccurate information about the measurement due to noise can by quantified by a *pdf* over the measurement space. This means the solution of the inverse problem is the probability density $P(\mathbf{x}|\mathbf{y})$ of the state conditioned on the measurement. Generally the mean of the $P(\mathbf{x}|\mathbf{y})$ is defined by the optimal estimate. Bayes' theorem defines how the measurement *pdf* maps into the state space and combines with prior information, according to the forward model $\mathbf{y} = \mathbf{F}(\mathbf{x}) + \epsilon$. The task in the non-linear as well as the linear case is to find a best estimate and an error characteristic that describes this *pdf* well enough for practical use. A short overview about inverse problems and a detailed discussion about Bayes' theorem can be found in Appendix A.

The Bayesian approach incorporate available prior knowledge of the wanted parameter. The mechanism for doing this requires to assume that the parameter is a random variable with a known prior probability density function. In the absence of data, the estimate is completely determined by the imposed prior knowledge. The choice of prior is critical in

Bayesian estimation, a wrong choice result in a poor estimator that is biased towards the prior mean. The effect of the data is to find an estimate that compromises between the data and prior.

A detailed discussion about inverse methods for atmospheric remote sounding can be found in [*Rodgers* (1976), *Rodgers* (1990), *Rodgers* (2000)].

5.5.2   The Best Linear Unbiased Estimator BLUE

With the Bayesian approach non-linear problems can be solved. The Bayesian approach tries to incorporate non-linearities while still using a linear estimation algorithm. The Bayesian solution for the linear problem can be modified for an inverse problem in which the forward model is a general function of the state. This requires that the estimate is constrained to be a linear function of the measurement. For not too non-linear or moderately non-linear problems a Gauss-Newton method can be applied for an iterative approach to find a optimal solution. The Gauss-Newton algorithm can be used to solve non-linear least square problems and uses a modification of Newton's method that does not use second derivatives (omitting small residual terms from the iteration in the case of non-linearity). The Gauss-Newton algorithm is an iterative procedure, this means the algorithm needs an initial guess for the parameters.

For the SMAS case, the spectral inversion can be done with an iterative Best Linear Unbiased Estimation (cf. [*Rodgers* (2000), *Kirchengast et al.* (2004)]) solution to obtain the atmospheric parameters (number density profiles of the absorbing species). The BLUE algorithm can be initialised by the atmospheric state obtained at the previous heigh level. Further, the BLUE requires the specification of covariance matrices for the number density and temperature data as well for the measurement data, which can be designed based on the knowledge of their respective error characteristics. The algorithm is initialised at high altitudes (e.g., 120 km) with some initial state, the errors due to initialisation decay quickly over about the first two or three scale heights. The BLUE principle minimises the variance of the linear combination of the data subject to the constraint, that the estimator must be unbiased, this means that the BLUE restricts the estimator to be linear in data. The SMAS forward model can be linearised by simply taking the logarithm of Beer-Bougert-Lambert's law, so at each altitude a standard linear model with additive noise results. The linearised form is convenient for the error analysis.

The baseline case for a fast converging iterative optimal estimation algorithm as the BLUE represents, is given by

$$\mathbf{x}_{i+1} = \mathbf{x}_i + \left(\mathbf{K}_i^T \, \mathbf{S}_\epsilon^{-1} \, \mathbf{K}_i\right)^{-1} \left[\mathbf{K}_i^T \, \mathbf{S}_\epsilon^{-1} \left(\mathbf{y} - \mathbf{y}_i(\mathbf{x}_n)\right)\right] \quad . \tag{5.24}$$

In Eq. 5.24, $\mathbf{x}_{i+1}$ is the iteratively estimated state vector. The starting point $\mathbf{x}_i = \mathbf{x}_0$ is a first guess profile and usually $\mathbf{x}_0 = \mathbf{x}_{ap}$, where $\mathbf{x}_{ap}$ accords to the *a priori* profile. The measurement vector corresponds to $\mathbf{y}$, $\mathbf{y}_i = \mathbf{K}(\mathbf{x}_i)$ to the forward model measurement vector which is estimated at any iteration step i; $\mathbf{y}_i = \mathbf{K}(\mathbf{x}_i)$ is used without modification, however. The measurement error covariance matrix $\mathbf{S}_\epsilon$ (see next section) in Eq. 5.24 characterises the measurement error (and is not only the covariance of the measurement error ϵ but also of the measurements) and the Jacobian weighting matrix $\mathbf{K}_i$ represent the mapping involved. The index i is the iteration index, which is started by using $\mathbf{x}_0 = \mathbf{x}_{ap}$.

The simulated transmission data are superimposed by a stochastic error realisation ϵ, produced by the means of an application of the error pattern method [*Rodgers* (2000)], and

are consistent with the measurement error covariance matrix. This method is described below, based on the use of the *a priori* covariance matrix $\mathbf{S}_{ap}$.

The equation above is practically repeated until a convergence criterion is reached or no further improvements of $\mathbf{x}_{i+1}$ over $\mathbf{x}_i$ are realised by further iterations. It should be considered that any additional iteration increases the computational time significantly, because at each iteration step the Jacobian weighting function matrix $\mathbf{K}_i$ has to be computed again. The cost function χ^2 specifies the number of needed iteration steps and can be calculated via

$$\chi^2 = (\mathbf{y} - \mathbf{y}_i)^T \mathbf{S}_\epsilon^{-1} (\mathbf{y} - \mathbf{y}_i) + (\mathbf{x}_i - \mathbf{x}_{ap})^T \mathbf{S}_{ap}^{-1} (\mathbf{x}_i - \mathbf{x}_{ap}) \tag{5.25}$$

at each iteration step i. The iteration stops and convergence is obtained when $\chi_i^2 \geq \chi_{i-1}^2$. The SMAS retrieval shows a satisfying accuracy after eight iterations. The basic condition to fulfil the convergence criterion is, if χ^2 is smaller than the number of selected channels.

5.5.3 Error Characterisation

Simulated Measurements

The simulated measurements of the normalised intensities requires an input profile vector containing temperature, air density, and ozone density. Because no real measurements are available, a random noise factor has to be added to the simulated measurements in order to generate quasi-realistic data. For the noise modeling normally distributed random numbers are created with standard deviation values according to the SMAS sensor characteristics.

A priori Covariance Matrix

For the retrieval calculations produced in this thesis, a standard background model, the climatological CIRA86 model [*Fleming et al.* (1988)] (temperature and air density) and the FASCODE model (ozone profiles) [*Anderson et al.* (1995)] are used to select the *a priori* profiles $\mathbf{x}_{ap}$. The *a priori* covariance matrix $\mathbf{S}_{ap}$ reflects how close the *a priori* profile is to the true state. A covariance matrix is symmetric and non-negative definite, and is always positive definite. Usually the true profile is not known in reality. For the temperature retrieval a linearly increasing error profile starting from 10 K at 50 km height up to 20 K at 100 km is used. For the *a priori* profiles typical errors are expected in prior ozone profiles and 20% uncertainty for the diagonal elements of $\mathbf{S}_{ap}$ is assumed. Further exists a correlation between the thin layers defined by the sampling rate of the SMAS sensor. For the non-diagonal elements of $\mathbf{S}_{ap}$ a correlation length $L = 6$ km is assumed, this means that the prior profiles are usually smooth at scales smaller than the atmospheric scale height. Theses non-diagonal elements are modeled via exponential drop-off and can be expressed by

$$(S_{ap})_{ij} = \sigma_i \, \sigma_j \exp\left[-\frac{|z_i - z_j|}{L} \right] \quad , \tag{5.26}$$

where z_i and z_j denote the height levels between which the covariance is expressed. The standard deviation is denoted by σ_i at a specific height level and corresponds to $\sigma_i =$
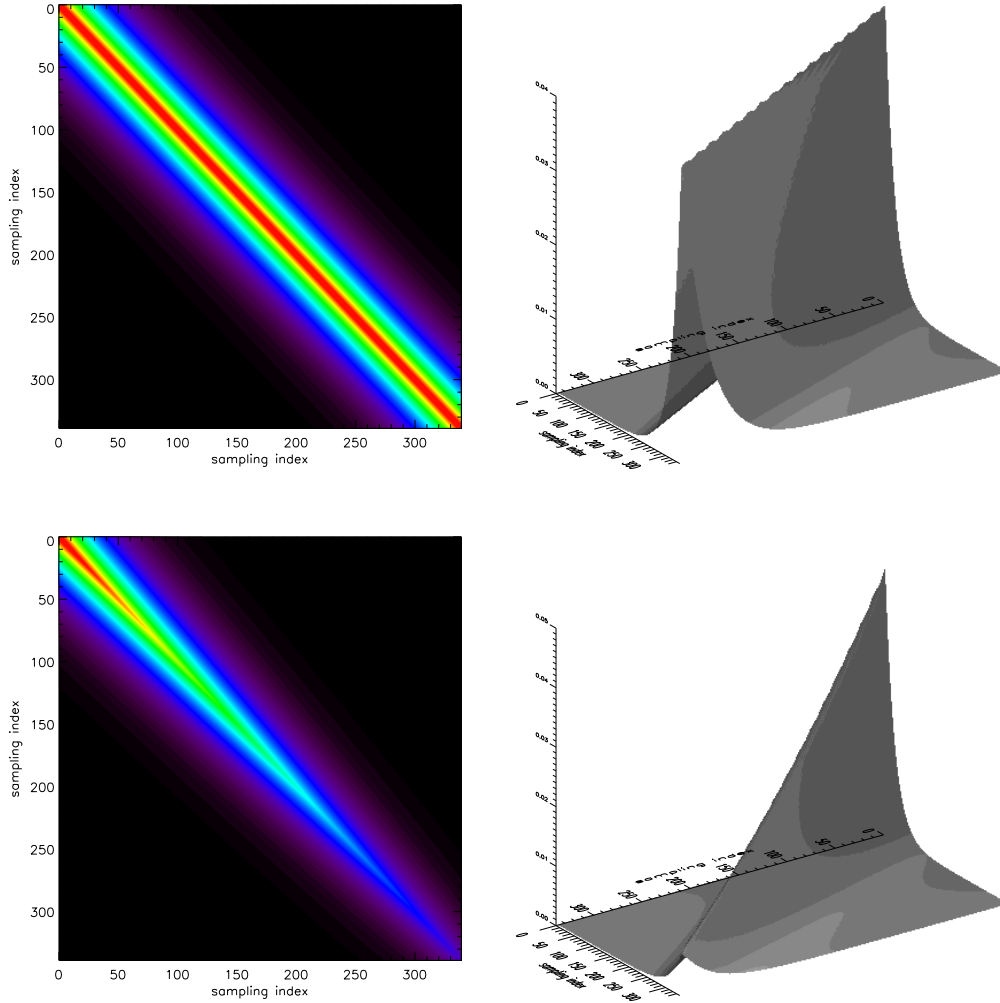
Figure 5.3. *A priori* covariance matrix $\mathbf{S}_{ap}$ for ozone (upper panel) and temperature (lower panel) with Gaussian drop-off correlations. The correlation length $L = 6$ km, assumed uncertainties of 20% for ozone, and 10 K at 50 km height up to 20 K at 100 km for the temperature, respectively.

$\sqrt{(\mathbf{S}_{ap})_{ii}}$. The notation of the resulting *a priori* covariance matrix for the joint retrieval can be expressed by

$$\mathbf{S}_{ap} = \left(\begin{array}{cc} \mathbf{S}_{ap}^{O_3} & 0 \\ 0 & \mathbf{S}_{ap}^{O_2} \end{array} \right) \ .$$

In Fig. 5.3 an example of the ozone covariance matrix and temperature covariance matrix used in the SMAS ozone and temperature retrieval is shown.

Error Pattern Method

With the error pattern method *a priori* profiles $\mathbf{x}_{ap}$ can be calculated which are consistent with $\mathbf{S}_{ap}$ (e.g., [*Rodgers* (2000)]). This method can be used for error vectors in general, but for simplicity reasons it is only used in this thesis in the notation of the *a*

priori profile. A covariance matrix is symmetric, so that the matrix of eigenvectors $\mathbf{L}$ is orthogonal and can be normalised, so that $\mathbf{L}^{-1} = \mathbf{L}^T$. In general any covariance matrix can be decomposed. For the *a priori* covariance matrix $\mathbf{S}_{ap}$ follows

$$\mathbf{S}_{ap} = \sum_i \lambda_i \mathbf{l}_i \mathbf{l}_i = \sum_i \mathbf{e}_i \mathbf{e}_i^T \quad , \tag{5.27}$$

where the orthogonal vectors $\mathbf{e}_i$ are the error patterns and these obey $\mathbf{e}_i = \sqrt{\lambda_i}\,\mathbf{l}_i$. The $\mathbf{e}_i$ can be regarded as eigenvectors $\mathbf{l}_i$ of the *a priori* covariance matrix $\mathbf{S}_{ap}$, weighted by the square root of the eigenvalues λ_i. The first ten error patterns of the ozone $\mathbf{S}_{ap}$ are shown in Fig. 5.4.
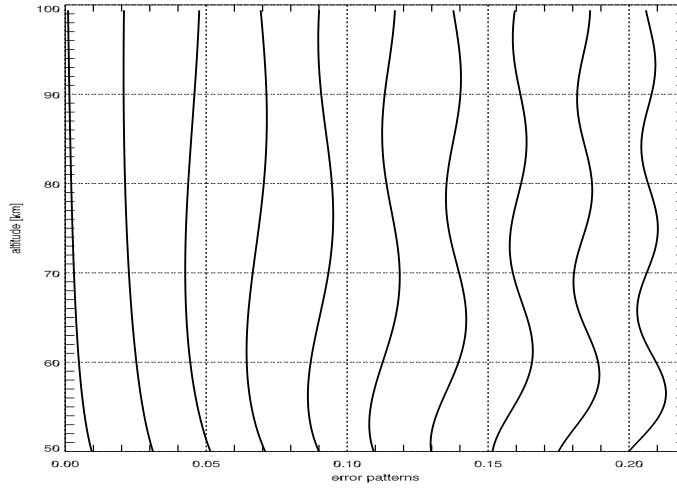
Figure 5.4. The first ten scaled eigenvectors (error patterns) of the ozone *a priori* covariance matrix $\mathbf{S}_{ap}$.

The random error ϵ in $\mathbf{x}$ can be expressed as a sum of these error patterns

$$\epsilon_x = \sum_i a_i\,\mathbf{e}_i \quad , \tag{5.28}$$

where the scalar coefficients a_i are normally distributed random deviates with unit variance, computed from a normalised Gaussian distributer. To generate the *a priori* profiles statistically consistent with the $\mathbf{S}_{ap}$, the error vector ϵ_x can be added to the "true" state vector $\mathbf{x}$. To verify this method, a so called *empirical* error covariance matrix $\mathbf{S}_e$ can be designed by forming the expectation value

$$\mathbf{S}_e = \langle \epsilon_x\,\epsilon_x^T \rangle = \frac{1}{n} \sum_{j=1}^n \epsilon_{j,x}\,\epsilon_{j,x}^T \tag{5.29}$$

of an ensemble of realisations. This is illustrated in Fig. 5.5 for an ensemble of $n = 100$ as well as of $n = 10000$ random vectors ϵ_x. As shown in this figure, the empirical matrix approaches the actual matrix with an increasing number of ensemble members. The
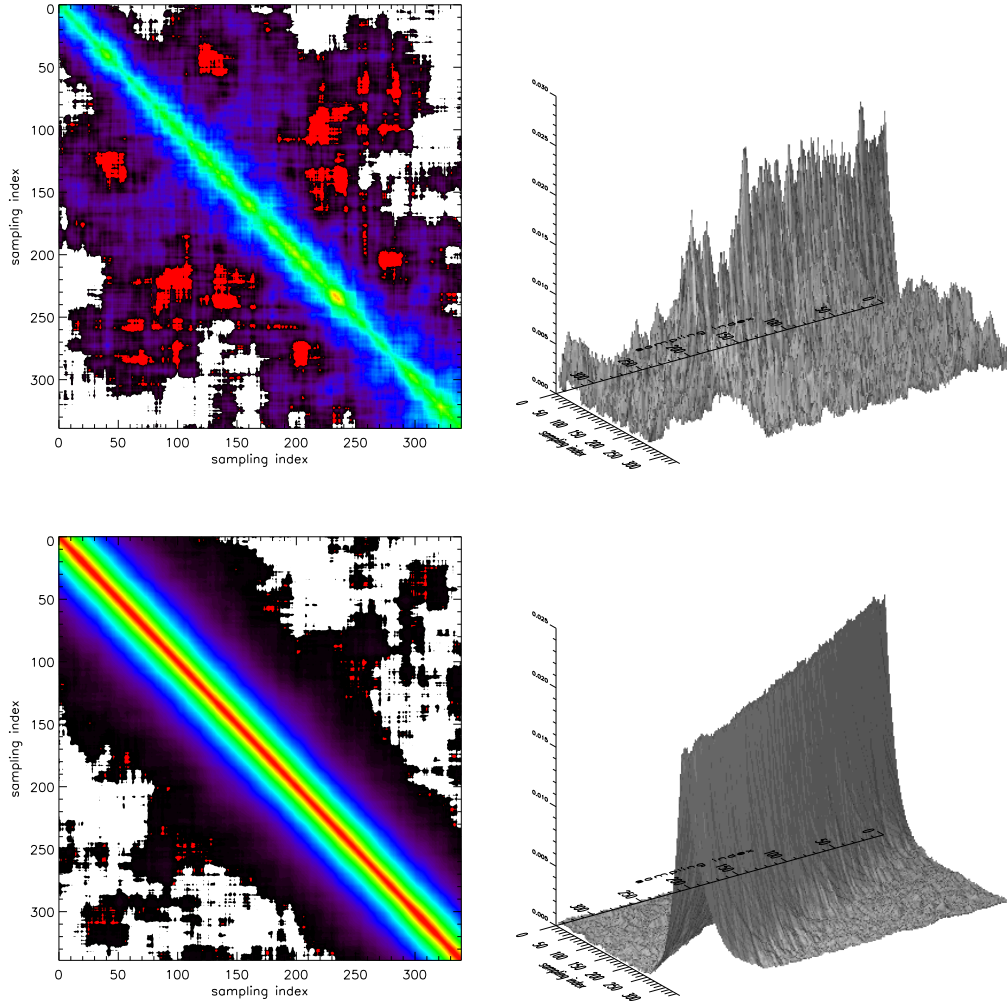
Figure 5.5. Empirical *a priori* ozone covariance matrix using ensemble of 100 (upper panel) and 10000 (lower panel) with Gaussian drop-off correlations. The correlation length $L = 6$ km and $\sigma = 20\%$.

original matrix can be reconstructed by an infinite number of contributing random errors to $\mathbf{S}_e$

$$\mathbf{S}_{ap} = \lim_{x \to 0} \sum_{j=1}^{n} \epsilon_{j,x} \, \epsilon_{j,x}^{T} \quad . \tag{5.30}$$

Error Covariance Matrix

Information about the data error is essential for solving any inverse problem. Typically, the errors are assumed to be independent, identically distributed with equal variance (referred to as the error variance), and the error variance is estimated as part of the optimisation. The error covariance matrix $\mathbf{S}_\epsilon$ was designed by taking 0.3% standard error (this corresponds to the RMS error characteristic as described in Section 5.4; also 0.1%

RMS error is possible, this corresponds to diamond diodes) at unity transmission and increasing errors with decreasing transmissions y_j, according to

$$(\mathbf{S}_\epsilon)_{jj} = \frac{RMS}{\sqrt{y_j}} \quad . \tag{5.31}$$

There is no correlation between neighboring channels and therefore the non-diagonal elements of $\mathbf{S}_\epsilon$ are set to zero.

5.5.4 Spectral and Spatial Inversion

Spectral Inversion

The separation of the absorbing species for all involved channels will be the first step in the SMAS retrieval scheme before starting the vertical (or spatial) inversion. The spectral inversion can be solved due to determination of the horizontal column number densities of absorbing species from the measured tangential atmospheric transmission data T_{ch}. This is coupled with the vertical inversion via an iterative loop. The columnar contents describing the vertical distribution of the absorbing species and can be determined using the BLUE algorithm as described above. The measured transmission can be expressed by Beer-Bougert-Lambert's law.

Spatial Inversion

The second step in the retrieval scheme is the inversion of the tangential column number densities into vertical number density profiles. This can be done for species which decreases approximately exponentially with altitude, via the Abel integral equation. The connection between the tangential column number densities $N_i(z)$ (z denotes the height coordinate) and the vertical number densities $n_i(z)$ takes the form of an Abel integral transform for a spherically symmetric atmosphere, this definition is general and applies to an arbitrary line of sight. By definition, the column number density of the ith absorbing species is given by

$$N_i(z) = \int_\infty^\infty n_i(s') \, ds' \quad , \tag{5.32}$$

where ds' is an element of path length along the line of sight, which origin is located at the tangent point and the detector assumed to be at $s = \infty$. In a spherically symmetric atmosphere, the ray path is symmetrical about the tangent point. Denoting the equations referring to the radius of the tangent point r_t, substituting the height coordinate z by the corresponding radius r, and furthermore by introducing the variable $r' = (s^2 + r_t^2)^{1/2}$, which gives the geocentric distance of an arbitrary point along the ray path, Eq. 5.32 takes the form of an Abel integral transform (cf., e.g., [*Hays and Roble* (1968a), *Hays and Roble* (1968b)])

$$N_i(r_t) = 2 \int_{r_t}^\infty dr' \frac{r' n_i(r')}{\sqrt{r'^2 - r_t^2}} \quad , \tag{5.33}$$

where $n_i(r')$ is the number density of the ith absorbing species at the distance r' from the center of Earth. Next, Eq. 5.33 can be inverted to obtain the number density of the ith

absorbing species at the radius r

$$n_i(r) = -\frac{1}{\pi} \int_{r_t}^{\infty} dr' \frac{1}{\sqrt{r'^2 - r_t^2}} \frac{dN_i(r')}{dr'} \quad . \tag{5.34}$$

To express Eq. 5.34 in terms of the tangent altitude z, the replacements $r' = z' + R_E$ and $r_t = z + R_E$ are necessary, and one obtains

$$n_i(z) = -\frac{1}{\pi} \frac{1}{\sqrt{2R_E}} \int_z^{\infty} dz' \frac{1}{\sqrt{z' - z}} \frac{dN_i(z')}{dz'} \quad , \tag{5.35}$$

where the approximation $r_t + r' = 2R_E + z + z' \approx 2R_E$ is used [*Lumpe et al.* (1991)] since the maximum effective value of either z or z' is much less than the radius of Earth. For tangent altitudes $z \leq 100$ km this approximation introduces an error of $< 1\%$. In thesis, the more accurate form, Eq. 5.34, is used directly.

Both equations are algebraic forms of the Abel integral equation relating the tangential column number densities $N_i(z)$ at different heights z to vertical density profiles $n_i(z)$ ($r = R_E + z$). For numerical computations, Eqs. 5.34 and 5.35 have a disadvantage because due to existence of a singularity at the lower integral boundary. That disadvantage can be evaded with the method used in this thesis which largely follows the work of S. Syndergaard [*Syndergaard* (1999)].

In order to perform the inversion with an algebraically convenient form, Eq. 5.34 is discretised with the so called *onion-peeling* method which corresponds to a division of the atmosphere into shells. Each shell corresponds to the distance between two consecutive sampling points, defined by the sampling rate of measurement device, which is 10 Hz for the SMAS sensor concept. The inversion algorithm has to be done for both absorbing species, thus the subscript index is suppressed further on. The Eq. 5.34 is discretised assuming first, that the derivations of the tangential number densities of each species vary linearly inside each shell. The Abel integral equation can be put into matrix form, discretised into m shells (the subscript index $j = 1, 2, \cdots, m$ corresponds to a finite number of mean radii r_j), and is regarded as a function of the independent impact parameters r_j or r_l corresponding to the mean radii (further on the subscript index t denoting the tangent point is neglected). Thus follows for Eq. 5.34

$$\mathbf{n} = \mathbf{A}\mathbf{N}_d \tag{5.36}$$

with $\mathbf{n} = (n_1, n_2 \cdots, n_m)$ and $\mathbf{N}_d = \left((\frac{dN}{dr})_1, (\frac{dN}{dr})_2, \cdots, (\frac{dN}{dr})_m\right)$, and

$$A_{jl} = \begin{cases} 0 & , \quad l < j \\ -\frac{1}{\pi(r_{j+1}-r_j)} \left[\sqrt{r_{j+1}^2 - r_j^2} - r_{j+1} \ln\left(\frac{r_{j+1}+\sqrt{r_{j+1}^2-r_j^2}}{r_j}\right) \right] & , \quad l = j \\ \frac{1}{\pi} \left\{ \frac{1}{r_l - r_{l-1}} \left[\sqrt{r_l^2 - r_j^2} - \sqrt{r_{l-1}^2 - r_j^2} - r_{l-1} \ln\left(\frac{r_l + \sqrt{r_l^2 - r_j^2}}{r_{l-1}+\sqrt{r_{l-1}^2-r_j^2}}\right) \right] \right. \\ \left. - \frac{1}{r_{l+1}-r_l} \left[\sqrt{r_{l+1}^2 - r_j^2} - \sqrt{r_l^2 - r_j^2} - r_{l+1} \ln\left(\frac{r_{l+1}+\sqrt{r_{l+1}^2-r_j^2}}{r_l+\sqrt{r_l^2-r_j^2}}\right) \right] \right\} & , \quad l > j \end{cases} \tag{5.37}$$

being the elements of an $(m \times m)$ triangular matrix $\mathbf{A}$ [*Syndergaard* (1999)]. The kernel $(r'^2 - r^2)^{-\frac{1}{2}}$ in Eq. 5.34 determines the structure, thus the diagonal elements in $\mathbf{A}$ are far the largest ones and they are falling off rapidly away from diagonal. The equations above can be used to calculate the vertical number densities of both, molecular oxygen

and ozone from the tangential column number densities. As known from similar cases in other occultation techniques (cf., e.g., [*Steiner et al.* (1999)]), the Abel inversion of course propagate not only the signal but measurement errors into the density profile.

The further calculation of the pressure and temperature profiles resulting from the retrieved density profiles is rather straightforward and is described in the next section.

5.5.5 Retrieval of Pressure and Temperature

From the retrieved molecular oxygen density profile parameters of the neutral atmosphere, such as density ρ, pressure p, and temperature T can be calculated by employing the hydrostatic equation. For the SMAS data analysis only the partial pressure of molecular oxygen is useful, from the known distribution of the atmosphere as mixture of gases (for molecular oxygen 20.948% per volume), the total pressure results. The contribution of the ozone partial pressure to the total pressure is negligible compared to the contribution of molecular oxygen. Thus only the data of molecular oxygen will be used to retrieve the pressure and temperature profiles.

The first step in the retrieval of a pressure profile from the density profile of molecular oxygen requires integration of the density profile along the vertical coordinate. Therefore the molecular oxygen number density profile $n^{O_2}(z)$ has to be related to the molecular mass density profile $\rho_m^{O_2}(z)$ by

$$\rho_m^{O_2}(z) = \frac{M^{O_2} n^{O_2}(z)}{N_A} \ , \tag{5.38}$$

where M^{O_2} denotes the molar mass of molecular oxygen and N_A corresponds to Avogadro's number. The pressure profiles can be derived via applying the hydrostatic equation, which defines that the downward oriented gravitational force F on a parcel of air must be equate the upward forces due to pressure gradients. Hence follows

$$dF = -\rho \, g(z, \varphi) dx \, dy \, dz \tag{5.39}$$

and for the pressure follows

$$dp = -\rho \, g(z, \varphi) \, dz \ , \tag{5.40}$$

which denotes the net force per area. The acceleration of gravity g can be calculated by [*Press* (1993)]

$$g(z, \varphi) = 9.806 \, (1 - 0.0026 \cos 2\varphi)(1 - 3.1 \times 10^{-7} z) \ . \tag{5.41}$$

The pressure can be obtained by integrating the hydrostatic equation

$$p^{O_2}(z) = \int_z^\infty g(z') \, \rho_m^{O_2}(z') \, dz' \tag{5.42}$$

with an initialisation top of atmosphere, defined at a height of 120 km with a pressure $p \simeq 0$. Initialisation errors decrease exponentially with the scale height of the atmosphere as the integration moves downwards the atmosphere.

Using the total atmospheric pressure profile, the temperature profile of the middle atmosphere follows. The retrieval of the atmospheric temperature profile from density

profiles, and from the partial $p^{O_2}(z)$ to total pressure profile $p(z)$ requires the ideal gas law. In each shell, the temperature $T(z)$ can be calculated as

$$T(z) = \frac{p(z)}{n(z)k} \ , \tag{5.43}$$

where k denotes the Boltzmann constant. This equation yields the temperature profile of the atmosphere.

5.6 Error Analysis Formulae

Every scientific result is subject to error. It is important when reporting a value to also report the error associated with it. Therefore error analysis and characterisation is an important task for every measurement. The Bayesian approach forms the basis for error analysis in the case of occultation measurements (cf., Appendix A) and a more detailed discussion about can be found in cf. [*Rieder and Kirchengast* (2001a), *Rieder and Kirchengast* (2001b)]). An introduction to error statistics can be found in [*Lang and Pucker* (1998), *Gershenfeld* (1999), *Storch and Zwiers* (1999)].

For a set of independent measurements $\mathbf{x}_i$ of an ensemble $\mathbf{x}$ of possible states in a system of interest several statistical properties can be defined. Typical variables are the mean value $\hat{\mathbf{x}}$, the variance $\hat{\sigma}^2$ (or $var(\mathbf{x})$), and the standard deviation $\hat{\mathbf{s}}$. These quantities are often called moments of a distribution of random variables.

For a data set, the mean (or first moment of a distribution) is just the sum of all the observations divided by the number of observations. The mean is the arithmetic average of a set of values and can be described as

$$\hat{\mathbf{x}} \equiv \frac{1}{n} \sum_{i=1}^{n} \mathbf{x}_i \ . \tag{5.44}$$

The mean tells nothing about how big the fluctuation in $\mathbf{x}$ are around it. A convenient way to measure this is by the variance $\hat{\sigma}^2$ (second moment of a distribution). This quantity in error statistic is in probability theory a measure of its statistical dispersion, indicating how its possible values are spread around the expected value. Where the expected value shows the location of the distribution, the variance indicates the scale of the values, and is a standard form to indicate the possible deviations from the mean. The variance can be expressed as

$$\hat{\sigma}^2 \equiv \frac{1}{n} \sum_{i=1}^{n} (\mathbf{x}_i - \hat{\mathbf{x}})^2 \ , \tag{5.45}$$

this defines the average value of the square of the deviation around the mean.

Another significant measure is the expectation value of the estimators given by Eq. 5.44 and Eq. 5.45, which is the average value of a distribution. The expectation value of $\hat{\mathbf{x}}$ is

$$\langle \hat{\mathbf{x}} \rangle = \frac{1}{n} \sum_{i=1}^{n} \langle \hat{\mathbf{x}}_i \rangle = \langle \mathbf{x} \rangle \equiv \mu_x \ , \tag{5.46}$$

while for the variance follows

$$\langle \hat{\sigma}^2 \rangle = \frac{1}{n} \sum_{i=1}^{n} \left\langle (\mathbf{x}_i - \hat{\mathbf{x}})^2 \right\rangle = \sigma_x^2 - \sigma_{\hat{x}}^2 = \frac{n-1}{n} \sigma_x^2 \ , \tag{5.47}$$

where σ_x^2 and $\sigma_{\hat{x}}^2$ are the variances for $\mathbf{x}$ and $\hat{\mathbf{x}}$, respectively. To obtain the expected mean value for the variance, Eq. 5.47 has to be corrected by the factor $n/(n-1)$. The differences of profiles are given by

$$\Delta \mathbf{x} = \mathbf{x}_m - \mathbf{x}_r \ , \tag{5.48}$$

where $\mathbf{x}_m$ represents the measurement and $\mathbf{x}_r$ a corresponding reference profile.

After defining such measures, an estimator for the so called *bias profile* can be obtained by substitution of $\mathbf{x}_i$ in Eq. 5.47 by $\Delta \mathbf{x}$

$$\hat{\mathbf{b}} \equiv \frac{1}{n} \sum_{i=1}^{n} \Delta \mathbf{x} \ . \tag{5.49}$$

Applying this to Eq. 5.45 and Eq. 5.47 results in

$$\hat{\mathbf{s}}^2 \equiv \frac{n}{n-1} \hat{\sigma}^2 = \frac{1}{n-1} \sum_{i=1}^{n} \left(\Delta \mathbf{x} - \hat{\mathbf{b}} \right)^2 \ , \tag{5.50}$$

where $\hat{\mathbf{s}}$ is an estimator of the standard deviation of a bias-free profile $\mathbf{x}_f = \Delta \mathbf{x} - \hat{\mathbf{b}}$.

In a more generally discussion an error covariance matrix $\mathbf{S}$ can be defined as

$$\mathbf{S} = \frac{1}{n-1} \sum_{i=1}^{n} \mathbf{x}_f \mathbf{x}_f^T \ . \tag{5.51}$$

The diagonal elements in $\mathbf{S}$ are variances at different height levels l, the non-diagonal elements denote covariance elements. Another measure of interest is the root-mean-square (RMS)

$$\mathbf{r} = \sqrt{\hat{\mathbf{b}}^2 + \hat{\mathbf{s}}^2} \ . \tag{5.52}$$

At last an error correlation matrix $\mathbf{R}$ can be found

$$R_{lk} = \frac{s_{lk}}{\sqrt{s_{ll} s_{kk}}} \ , \tag{5.53}$$

where the non-diagonal elements define error cross-correlations. Full correlation is given for values of one in $\mathbf{R}$, while zero non-diagonal values indicate no correlation (the diagonal elements are all one and $\mathbf{R}$ equal the unit matrix).

5.7 Statistical Optimisation of Ozone Profiles

The Abel inversion propagate not only the signal but the measurement into the density profile. This provides an instable ozone profile at heights > 90 km due to the absorption behaviour of ozone (cf. Section 2.5.4). To produce continuous ozone profiles (and a stable iterative retrieval algorithm) up to the upper boundary of the measured transmission data, a routine which optimally combines measured and background (*a priori*) vertical ozone number density profiles has to be used.

An optimal solution can be found with

$$\mathbf{n}_{opt} = \mathbf{B}\,\mathbf{n}_o + (1 - \mathbf{B})\,\mathbf{n}_b \ , \tag{5.54}$$

where $\mathbf{n}_b$ is the background, $\mathbf{n}_o$ the observed number density profile, respectively. The error covariance matrix $\mathbf{B}$ denotes the Gaussian transition from the observed to the background profile and can be expressed as

$$B_{ii} = \begin{cases} \sigma_i \sigma_i \exp\left(-\frac{(r_0 - r_i)^2}{L^2}\right) & , \; r_i \geq r_0 \\ 1 & , \; r_i < r_0 \end{cases} \tag{5.55}$$

where r_0 denotes the height level where the transition starts (the altitude where the ozone retrieval starts to be instable) and r_i is the impact parameter at different height levels. The correlation length $L = 2$ km and the background errors (σ_i) are set to be one. For altitudes lower r_0 the diagonal elements are set to be one, this means, only the observed profile accounts to the statistical optimisation [*Gobiet and Kirchengast* (2002)]. As background profiles FASCODE model data were chosen. A more detailed discussion about statistical optimisation can be found in [*Gobiet and Kirchengast* (2002), *Gobiet and Kirchengast* (2004)].

6 Retrieval Performance Analysis Results

In this Chapter retrieval results are presented, derived from the SMAS Schumann-Runge/Herzberg and Hartley band channels 7 to 16 of Tab. 4.1. Monitoring the mesosphere by the SMAS solar occultation sensor starts with the measurement of signal intensity profiles, normalised to transmission profiles, one for each channel. The sequential inversion process starts with a spectral inversion of transmission data to molecular oxygen and ozone columnar content profiles, followed by a spatial inversion via Abelian transform to obtain vertical number density profiles. The same was done for molecular oxygen to obtain air density profiles, which are forming the basis of the temperature retrieval.

The spectral inversion converts the transmission data from the ten MUV-channels into columnar contents describing the horizontally-integrated vertical distribution of the two main absorbers, molecular oxygen and ozone. Therefore a joint ozone and temperature retrieval scheme based on SMAS transmission data was developed, processed with an optimal estimation technique (cf. Section 5.5) providing a first guess from *a priori* information.

Month	Latitude	O_2 and temperature: CIRA-86 model	O_3 profile: FASCODE model
January	Equator	Equator	Tropical / model 5
	MidLat.	40 deg North	MidLat. Winter / model 3
	HighLat.	60 deg North	SubArctic Winter / model 4
March	Equator	Equator	Tropical / model 5
	MidLat.	40 deg North	MidLat. Winter / model 3
	HighLat.	60 deg North	SubArctic Winter / model 4
July	Equator	Equator	Tropical / model 5
	MidLat.	40 deg North	MidLat. Summer / model 2
	HighLat.	60 deg North	SubArctic Summer / model 4
October	Equator	Equator	Tropical / model 5
	MidLat.	40 deg North	MidLat. Summer / model 2
	HighLat.	60 deg North	SubArctic Summer / model 4

Table 6.1. Temperature and density profiles (ozone and molecular oxygen) used in the SMAS retrieval scheme.

6.1 Ozone and Molecular Oxygen Density Profiles Retrieval Performance

For the ozone and molecular oxygen (as well as for the temperature) retrieval, an optimal estimation scheme (cf. Section 5.5) including prior information was used. The ozone *a priori* information data were derived from AFGL-TR-86 data (FASCODE model) (cf., e.g., [*Anderson et al.* (1995)]). Table 6.1 summaries the density and temperature profiles used for the SMAS forward model and retrieval. The temperature and molecular oxygen profiles are calculated from the CIRA-86 model. In this simulation study, SMAS transmission profiles and geolocation data were taken and processed with the BLUE inversion scheme. The forward model and its derivatives are called iteratively, which is forming the core of the retrieval. The *a priori* information is of major importance because it is used to initialise as first guess the iteration of the retrieval. In a first step, the geolocation data were provided using an end-to-end simulator (EGOPS) (cf. [*Kirchengast* (1998), *Kirchengast et al.* (2002)]). The EGOPS delivers 'true' LEO orbits, geodetical position of the LEO satellite as well as a well approximated position of the Sun. The test occultation event was situated over north-eastern France and was the one also used by [*Retscher et al.* (2004a)].
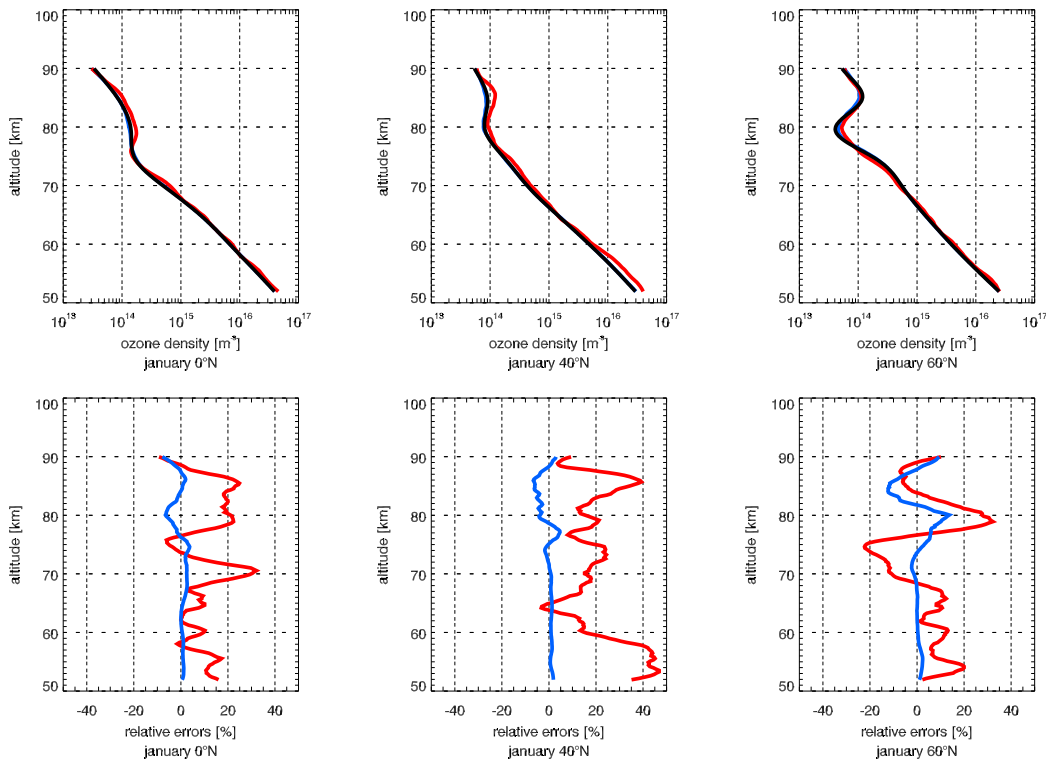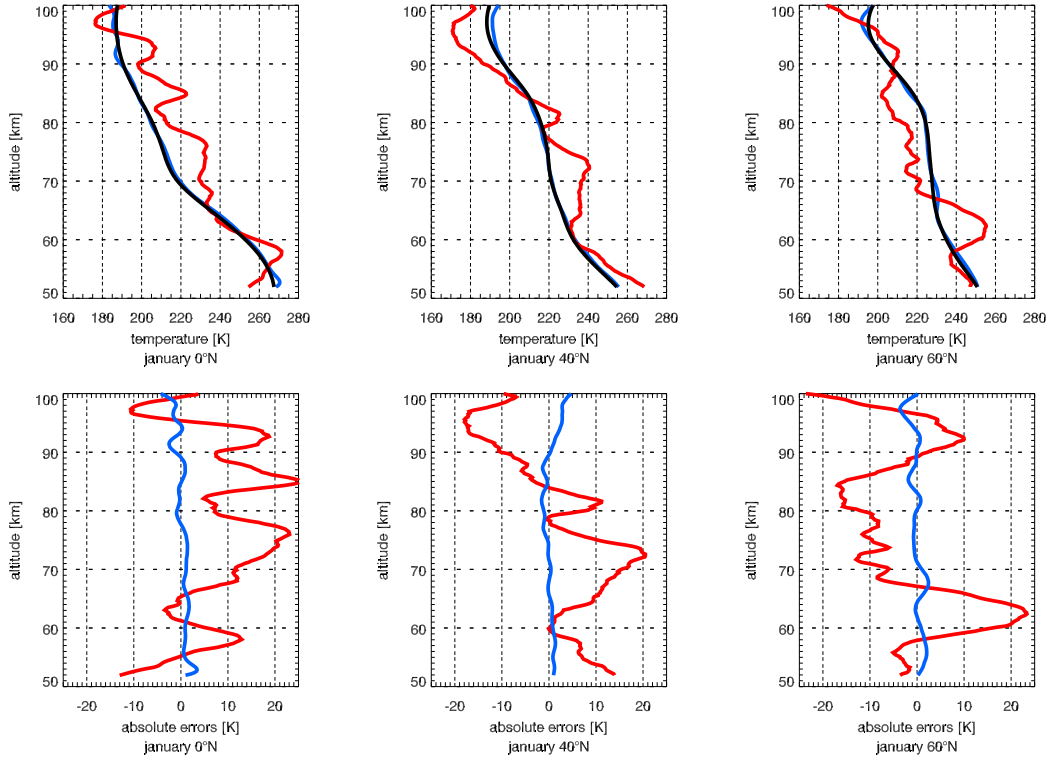

Figure 6.1. Simulated single ozone density profiles resulting from the SMAS processing system (upper panel) for three different latitudes (Equator, 40 deg north, 60 deg north) for January. The basic ozone densities were calculated from the AFGL-TR-86 (FASCODE) model (cf. Tab. 6.1). The solid black lines correspond to the 'true' reference profiles and the red lines to the *a priori* profiles. The blue lines denote the retrieved ozone density profiles after eight iterations. The lower panels show the related departure of the *a priori* ozone density profiles (red lines) and the retrieved ozone density profiles (blue lines) from the 'true' profiles, respectively.

The iterative BLUE algorithm combined with the Abel inversion can be used to calculate the vertical ozone and molecular oxygen number density profiles. Some exemplary retrieved single ozone profiles (upper panel) for January for three different latitudes (Equator - left panel, 40 deg north - middle panel, and 60 deg north - right panel) are illustrated in Fig. 6.1, with densities over a logarithmic scale. The molecular oxygen density was calculated from the CIRA-86 model, the ozone density from AFGL-TR-86 data. The illustrated vertical number density profiles contain some noise (induced 0.3% measurement error at 10 Hz-sampled transmission data; corresponds to SMAS silicon diode detectors, cf. Section 5.4). The vertical resolution is about 2 km. A relative ozone retrieval error of less than $\pm 5\%$ in most of the height domain of interest up to 90 km is found for the 0.3% measurement error case.

The lowest impact parameter r_1 in Eq. 5.37 corresponds to about the 50 km height level, where $T_{ch} > 0.05$ for the lowest-reaching channel, while the uppermost impact parameter r_m corresponds to an altitude of about 100 km ($T_{ch} < 0.95$). The Abel inversion is of course error-sensitive, this is, in particular, noticeable in the retrieved ozone number density profiles at heights > 90 km. To calculate the vertical ozone number density it is meaningful to use the statistical optimisation procedure as described in Section 5.7. This procedure is necessary to provide a continuous vertical ozone profile (for the use of the iterative BLUE algorithm) up to the height of the upper boundary of the transmission data (around 100 km). Furthermore, the discretisation of the Abel integral equation provides a discretisation error $< 1\%$ [*Syndergaard* (1999)].

The effects of scintillation and dilution (cf. Section 5.2) were neglected in this work (the reasonable error resulting in the modeled transmissions is of size $< 1\%$ [*Retscher* (2004)]). The *a priori* error covariance matrix was chosen to have a standard deviation of 20% for ozone. The random errors in the forward model were designed as outlined in Section 5.4, and *a priori* data as given in Section 5.5.3. The error incurred by the discretised solution of the Abel transform with a matrix inversion technique and due to the numerical programming of the columnar contents profile is very small and negligible.

Ozone absorbs only for the most part in the Hartley band, with the used upper wavelength boundary at 246 nm, which defines the upper vertical boundary of a stable ozone retrieval scheme and is situated around 90 km for the SMAS sensor concept. The inversion of the ozone vertical number density is very sensitive against the measurement error at high altitudes. This can be readily explained considering the SMAS transmission plot (see Fig. 5.1); no appreciable signal from the 210-to-246-nm-channels exists at altitudes above 90 km. Thus the ozone profile can be observed up to an altitude of about 90 km, which is sufficient to scan the mesosphere, however. Ozone concentration above the mesosphere is generally negligible.

For molecular oxygen, a stable inversion results up to an altitude of about 100 km. The *a priori* information data were derived from the CIRA-86 model. For the molecular oxygen retrieval a linearly increasing error profile starting from 10% at 50 km height up to 20% at 100 km was used. The resulting molecular oxygen density profiles are shown in Fig. 6.2 for the same latitudes as in Fig. 6.1 for January (converted into the air densities using the known distribution of the atmosphere as mixture of gases). A relative molecular oxygen retrieval error (as well as air density retrieval error) of less than $\pm 2\%$ is found for the 0.3% measurement error case for the major part of the height domain of interest.

It results that the channels from 190.00 nm up to 204.25 nm primarily detect the molecular oxygen-attenuated solar radiation. For the inversion of the vertical molecular
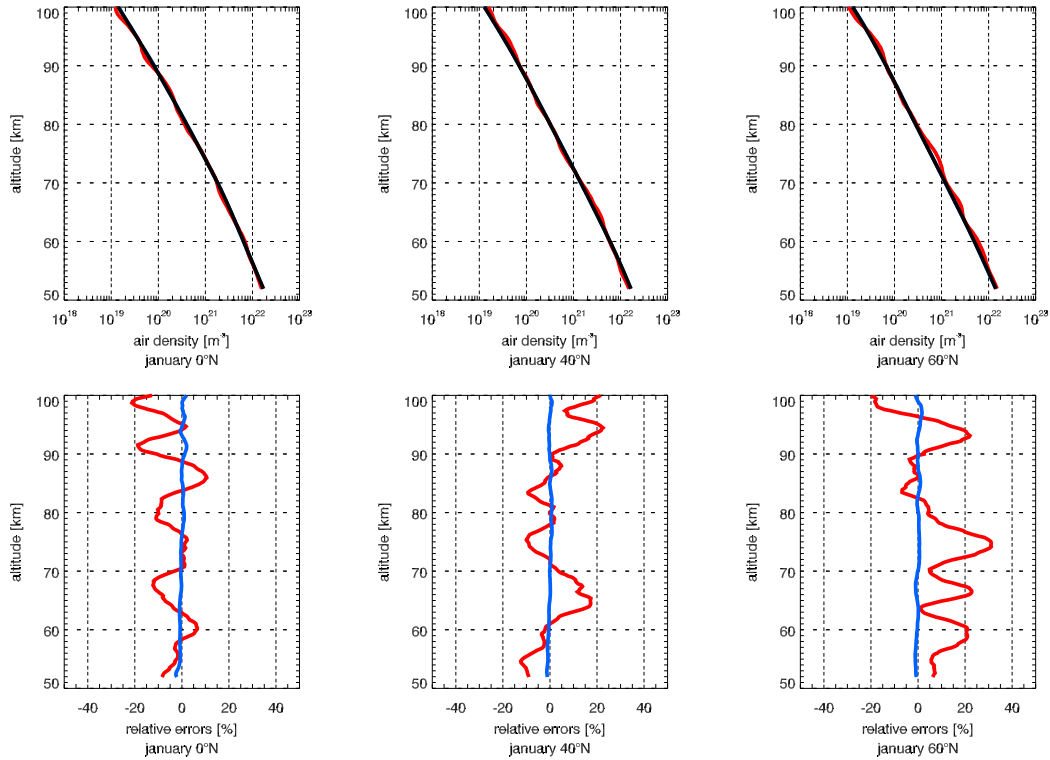
Figure 6.2. Simulated single air density profiles resulting from the SMAS processing system (upper panel) for three different latitudes (Equator, 40 deg north, 60 deg north) for January. The air densities were calculated from the CIRA-86 model (January). The solid black lines correspond to the 'true' reference profiles and the red lines to the *a priori* profiles. The blue lines denote the retrieved air density profiles after eight iterations. The lower panels show the related departure of the *a priori* air density profiles (red lines) and the retrieved air density profiles (blue lines) from the 'true' profiles, respectively.

oxygen number density, the influence of noise is very small, therefore the inversion is very stable up to a top altitude of about 100 km.

6.1.1 Statistical Errors of Ozone and Molecular Oxygen Density Profiles

Three single events were selected in the Section above, the resulting ozone and molecular oxygen profiles, and theirs corresponding errors, have been illustrated in Figs. 6.1 and 6.2. Here, a more substantial error analysis is performed for four different months (January, March, July, and October) and three different latitudes (Equator, 40 deg north, and 60 deg north). The statistical analysis is realised by choosing 30 randomly initiated profiles calculated for one and the same occultation location. An example of an ensemble of 30 randomly initiated ozone (upper panel) and molecular oxygen (converted into air density, lower panel) density profiles is shown in Fig. 6.3. The bias profile $\hat{\mathbf{b}}$ (Eq. 5.49) and the bias $\pm$ standard deviation profiles $\hat{\mathbf{b}} \pm \hat{\mathbf{s}}$ (Eq. 5.50) are illustrated in Fig. 6.4.

The bias profiles in Fig. 6.4 show errors almost always lying below 2% for all height levels between 50 km and 70 km. Between 70 km and 80 km the profiles tend to have biases up to about 5%, and above the biases can accrue up to 10%, which reflects the low signal response at high altitudes in the Jacobian matrix. Due to the lower signal, the

a priori date have more effect on the retrieved profiles. The standard deviations of the shown profiles are below 1% for altitudes up to 70 km. Between 70 km and 80 km, the standard deviations increases to about 2%, above deviations greater than 5% can occur.

The molecular oxygen (air density) error profiles are illustrated in Fig. 6.5. The error is almost always lying below 1% for altitudes up to about 100 km. Only for lower altitudes ($\sim$50 km) the error increases due to the signal becoming smaller. Here the bias error can reach up to $\sim$2%. A similar performance results for the standard deviation profile, which lies between 55 km and 100 km at < 2%. Only at the lower boundary of the transmission data, the standard deviation can increase up to $\sim$4%.
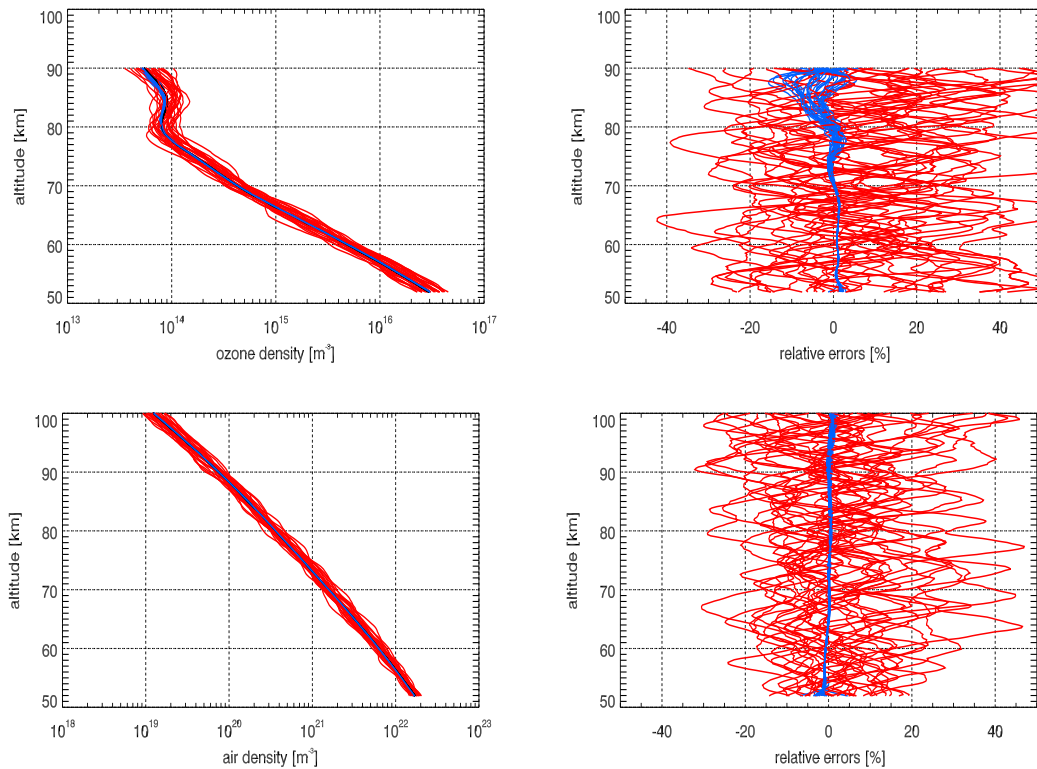
Figure 6.3. Ensemble of ozone (upper panel) and molecular oxygen (lower panel) profiles. The ensemble consists of 30 randomly initiated profiles for one and the same occultation location. The black lines (almost not visible) denote the 'true' reference profiles. The blue lines denote the retrieved single ozone and molecular oxygen profiles, respectively, and the red ones the *a priori* ozone profiles. While the left panels show the profiles directly, the right panels show the related relative errors; the departure of the *a priori* profiles (red lines) and the retrieved profiles (blue lines) from the 'true' profiles, respectively.

According to these results, the SMAS processing system well accomplishes the requirements defined in Section 4.1.2. The statistical analysis demonstrates the robust mode of operation of the chosen retrieval process. Figures 6.3, 6.4, and 6.5 clearly point out the basic capability of the SMAS processing system for accurate ozone and air density retrieval in the mesosphere.
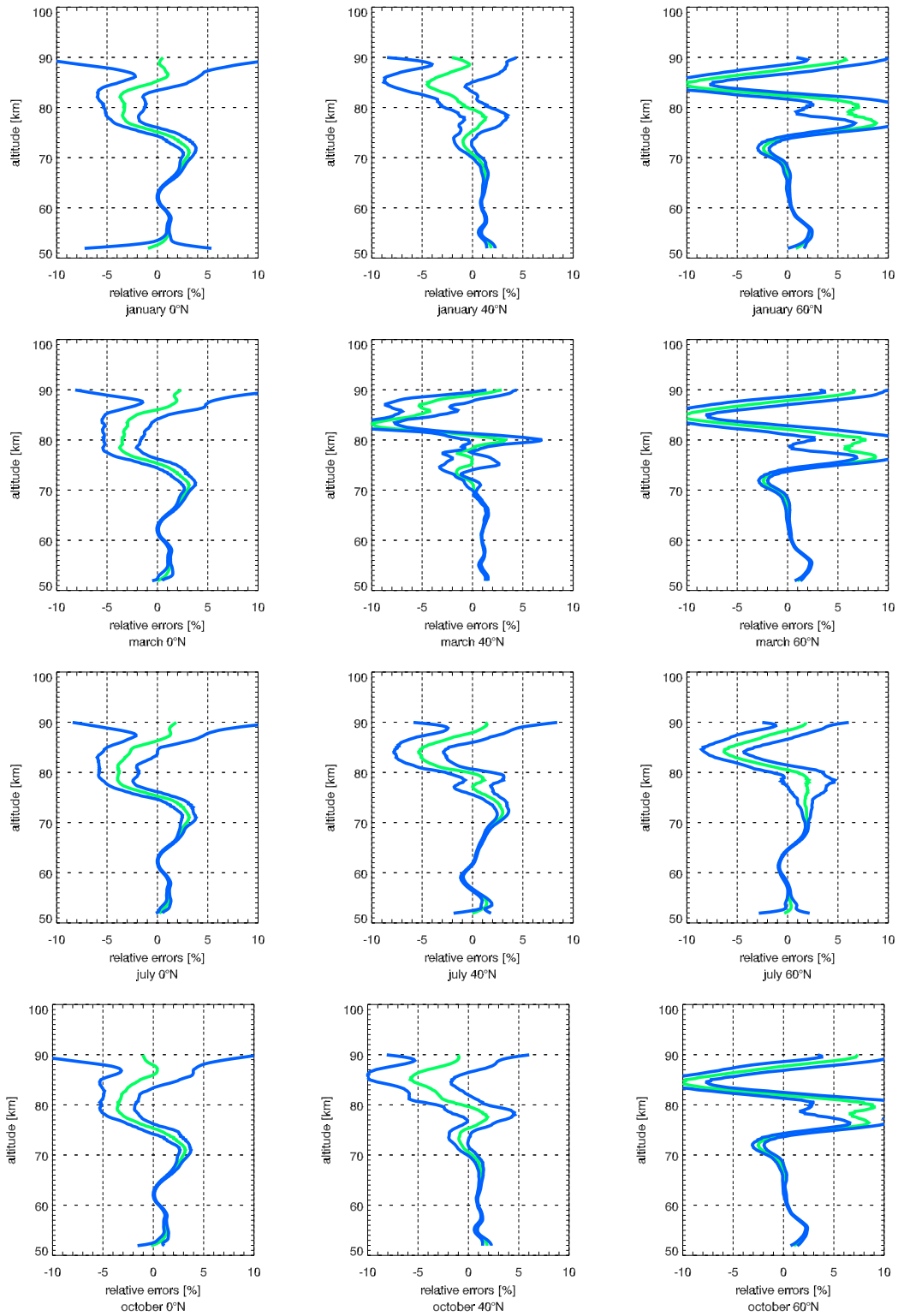
Figure 6.4. Statistical errors for simulated ozone profiles with 30 profiles contributing, for four different months (January, March, July, and October), and three latitudes (Equator, 40 deg north, and 60 deg north). The green lines are the bias profiles and the enveloping blue lines are the bias ± standard deviation. A measurement error of 0.3% in the transmission data was assumed.

110
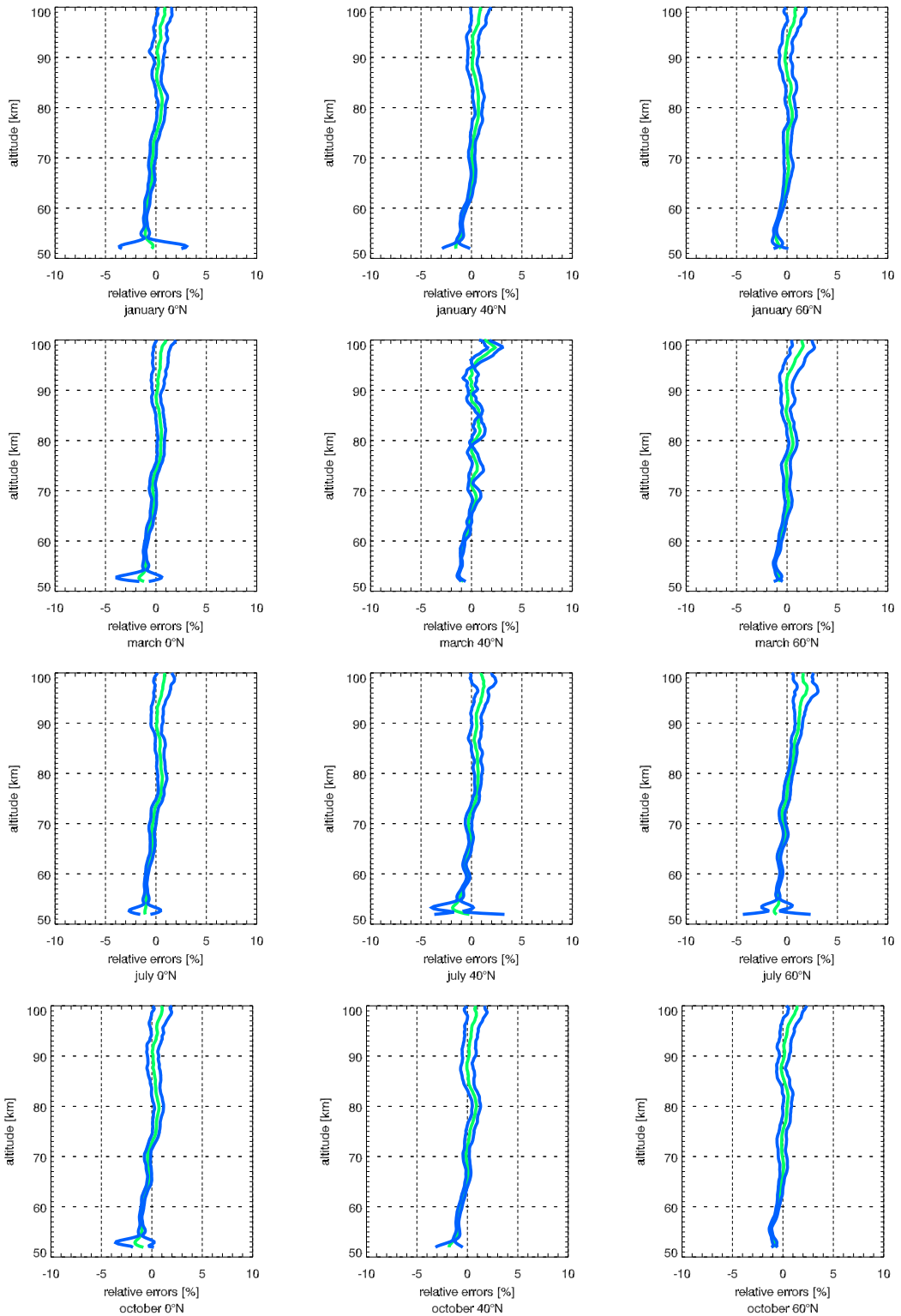
Figure 6.5. Statistical errors for simulated air density profiles with 30 profiles contributing, with same conditions (including the same measurement error) as described for Fig. 6.4. The green lines are the bias profiles and the enveloping blue lines are the bias ± standard deviation.

111

6.2 Temperature Profiles Retrieval Performance

This Section discusses the retrieval performance of a single temperature profile derived from the air density profile via a pressure profile. As in the previous Section, three latitudes for January, for the northern hemisphere were processed. The retrieval routines follow the BLUE inversion scheme (described in Section 5.24) to produce the molecular oxygen columnar content N_{O_2} (spectral inversion), combined with the Abel inversion of the columnar content to obtain vertical density profiles n_{O_2} of molecular oxygen (spatial inversion). As described in Section 5.5.5, the partial pressure p_{O_2} of molecular oxygen and the total atmospheric pressure p result from the hydrostatic equation given by Eq. 5.39. The retrieval of the temperature profile $T(z)$ from the pressure (and density) profile requires the use of the ideal gas law as described by Eq. 5.43. The full chain is:

$$T_{ch}(z) \rightarrow N_{O_2}(z) \rightarrow n_{O_2}(z) \rightarrow p_{O_2}(z), p(z) \rightarrow T(z) \ . \qquad (6.1)$$

Figure 6.6. Simulated single temperature profiles resulting from the SMAS processing system (upper panel) for three different latitudes (Equator, 40 deg north, and 60 deg north) for January. The solid black lines correspond to the 'true' reference profiles and the red lines to the *a priori* profiles. The blue lines denote the retrieved temperature profiles after eight iterations. The departure of the *a priori* temperature profiles (red lines) and retrieved temperature profiles (blue lines) from the 'true' profiles, respectively, is shown in the lower panels. A measurement error of 0.3% in the transmission data was assumed.

The resulting single temperature profiles are illustrated in Fig. 6.6, from this plot follows that an accurate profile of the temperature can be obtained with the SMAS sensor

concept, analogous to the density profiles of molecular oxygen, up to an altitude of about 100 km.

No significant bias of the retrieved temperature from residual errors in the discretisation of the Abel integral (the numerical solution of the Abel transform), the spectral inversion procedure, and the numerical solution of the hydrostatic integral is observed. The vertical resolution of the profiles is about 2 km. For the error characterisation of the *a priori* temperature profiles, a linearly increasing error profile starting from 10 K at 50 km height up to 20 K at 100 km was used. The temperature was calculated from the CIRA-86 model. As Fig. 6.6 quantitatively shows, the error of the retrieved temperature profile is less than ±2.5 K for the height region up to an altitude of about 100 km.

6.2.1 Statistical Errors of Temperature Profiles

The same three latitudes and four months used in Section 6.1.1 were used for the SMAS temperature statistical performance analysis. The *a priori* information was taken from the CIRA-86 model. In Fig. 6.7, an ensemble of 30 randomly initiated temperature profiles is illustrated (left panel). The red lines denote the *a priori*, the blue lines the retrieved temperature profiles, respectively. The right panel shows the related relative (ideal case/*a priori*) errors, the linearly with altitude increasing error in the *a priori* profiles is well visibly in this plot.
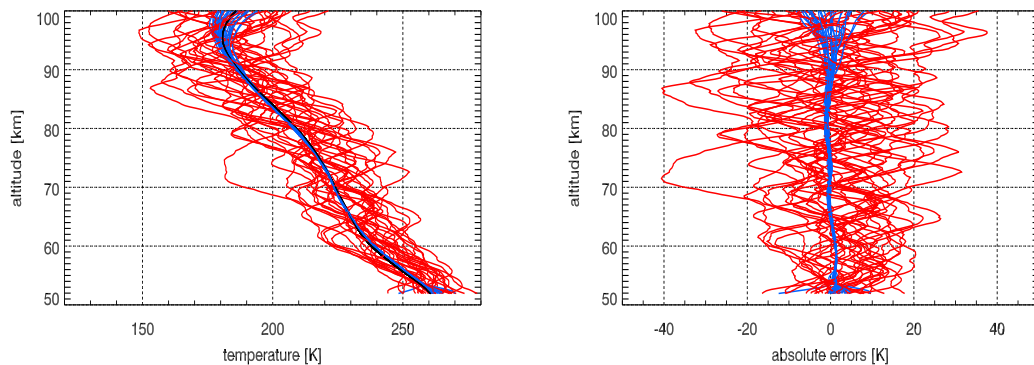
Figure 6.7. Simulated temperature ensemble (left panel) and related relative errors (right panel). The ensemble consists of 30 randomly initiated profiles for one and the same occultation location. The black line (almost not visible, left panel) denotes the 'true' reference profile. The blue lines refer the retrieved single temperature profiles and the red ones to the *a priori* temperature profiles. While the left panel shows the profiles directly, the right panel shows the related relative errors; the departure of the *a priori* profiles (red lines) and retrieved profiles (blue lines) from the 'true' profile, respectively.

In Fig. 6.8 the statistical temperature errors for an ensemble of profiles are shown for four different months (January, March, July, and October) and three latitudes (Equator, 40 deg north, and 60 deg north). The bias profiles show errors almost always below 2 K for the height range between 55 km and 100 km; only for regions below 55 km the errors increase up to ∼3 K. The standard deviation in the height region between 55 km and 90 km is below 2 K, for higher altitudes above 90 km it can increase up to 5 K due to the low signal response in the Jacobian matrix. For regions below 55 km, the standard deviation can increase similarly as for higher altitudes (∼5 K). In summary, a good estimation of the temperature profile over the entire mesosphere can be done with the SMAS sensor concept, in line with the SMAS requirements.
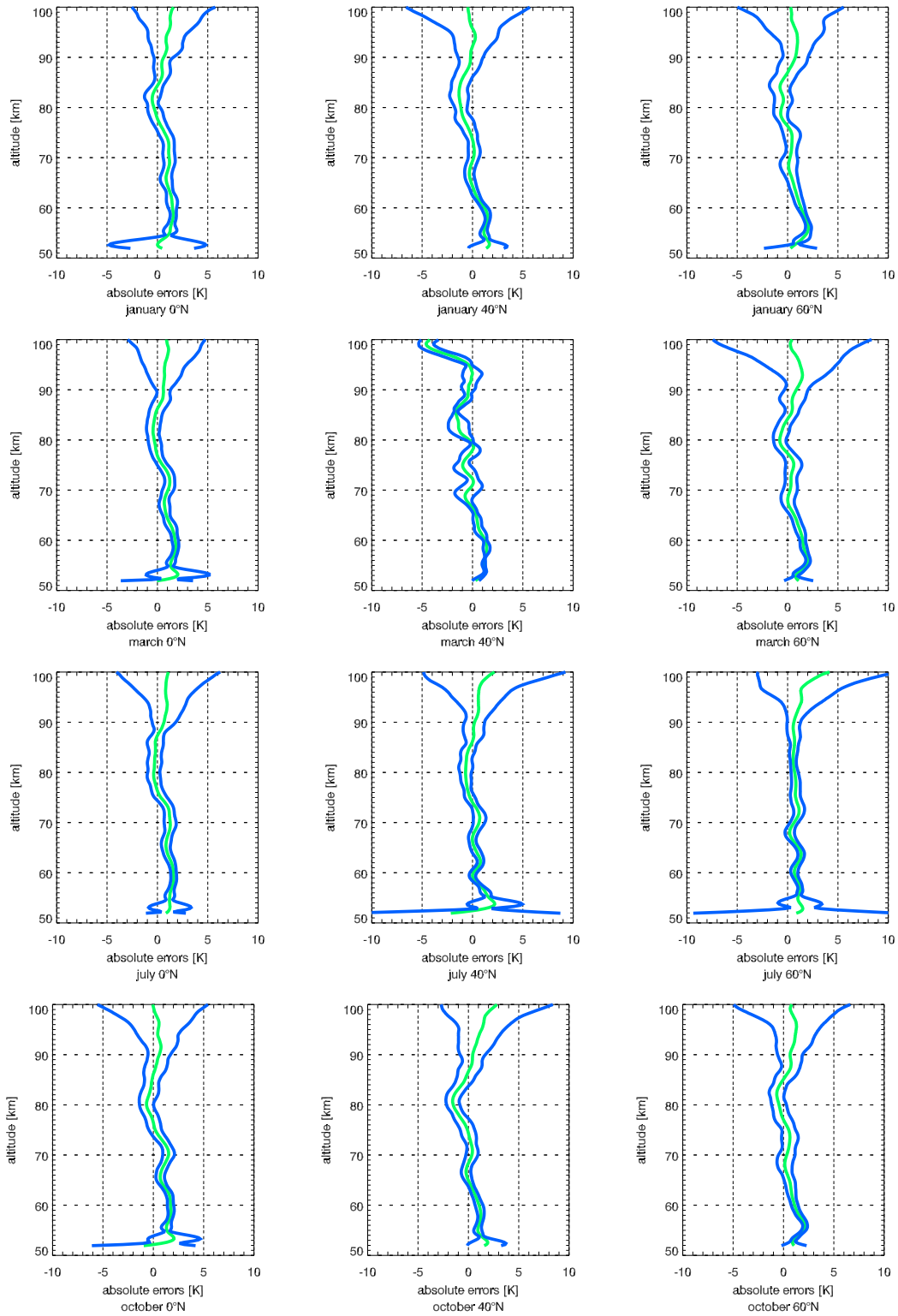
Figure 6.8. Statistical errors for simulated temperature profiles with 30 profiles contributing, with same conditions (same measurement errors) as described for Fig. 6.4. The green lines are the bias profiles and the enveloping blue lines are the bias ± standard deviation.

114

6.3 Global-mean Results for Ozone, Air, and Temperature Profiles

In this Section the overall, average values of the statistical errors of the regarded ensembles of density profiles of ozone, air (air density profiles are in general more meaningful for atmospheric investigations than molecular oxygen profiles), and temperature are illustrated. The performance analysis (as described in Section 5.6) again includes profiles of four different months (January, March, July, and October) and three different latitudes (Equator, 40 deg north, and 60 deg north). From this set of 12 ensembles in total, the global-mean values of the bias profiles and bias ± standard deviation profiles were calculated for two different cases of measurements error, for (1) standard UV silicon diodes, and (2) more precise UV diamond diodes. The first case corresponds to a measurement error of 0.3%, as already used for all previous performance analysis results shown, the latter case corresponds to a reduced measurement error of 0.1%.
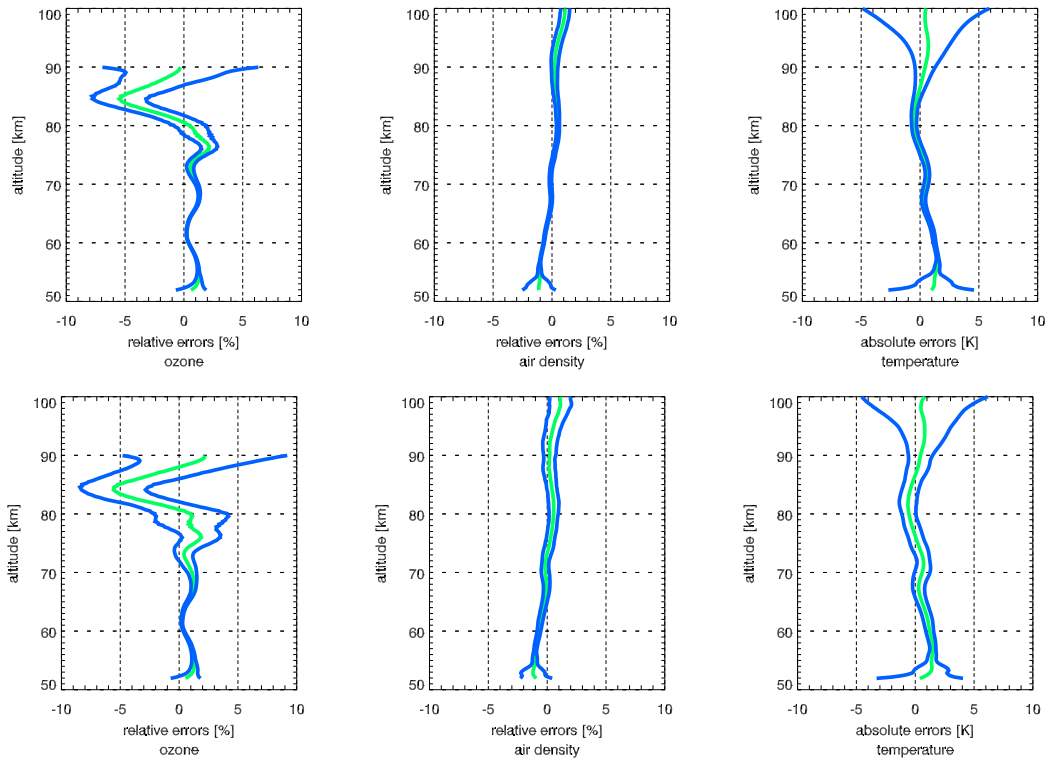
Figure 6.9. Global-mean results of the statistical performance analysis for two different cases of assumed measurement errors for ozone (left panels), air density (middle panels), and temperature (right panels). The upper panels illustrate 0.1%, the lower panels 0.3% measurement error, respectively. The green lines are bias profiles and the enveloping blue lines are the biases ± standard deviations of the full set of profiles.

Figure 6.9 shows that for ozone the global-mean bias lies below 2% up to an altitude of about 80 km, above it increases up to 5% for both measurement error cases. For temperature, the resulting global-mean bias lies below 2 K for the complete height range of interest for both cases. The global-mean air density bias behaves similarly for both cases, it lies below 2%. Considering the global-mean standard deviations, the magnitude

115

increases, as is to be expected for increasing measurement error, as Fig. 6.9 instructively shows.

In summary, the resulting global-mean bias profiles are essentially identical for both measurement error cases and fulfil the requirements laid out for the SMAS sensor concept. The standard deviation increases with increasing measurement error but it is still within the SMAS requirements in almost the entire domain of interest also for the standard UV silicon diode 0.3% errors.

Summary and Conclusions

In this thesis a new concept of solar occultation measurements was analysed, allowing to retrieve vertical profiles of temperature and ozone throughout the mesosphere. An end-to-end performance analysis for both atmospheric parameters was carried, out based on an implementation of adequate retrieval techniques.

The Sun Monitor and Atmospheric Sounder (SMAS) solar occultation sensor concept enabled the retrieval of the atmospheric key parameters temperature and ozone (along with air density and others), furnishing a good estimation of the atmospheric state in the mesosphere. The measured limb normalised intensity (transmission) data can be related to height profiles of the major absorbing species, which are for the mesosphere, in the regarded middle ultraviolet wavelength region, just molecular oxygen and ozone. Molecular oxygen density profiles can, in turn, be converted to pressure and temperature profiles. These data are of major importance for atmospheric analysis and process studies as well as for middle atmosphere modeling and climate change monitoring. This thesis demonstrated for SMAS the feasibility of the concept.

In the first Chapter a detailed discussion on relevant atmospheric physics was given. It illustrated the composition and structure of the atmosphere, especially the middle atmosphere, and gave an introduction to ozone physics and chemistry. The subsequent second Chapter dealt with details on atmospheric and solar radiation, including the connection between radiative transfer to the concept of absorption, emission, and scattering processes. An important part of this Chapter focused on the complex molecular oxygen ultraviolet absorption system, including the Schumann-Runge and Herzberg absorption system. The third Chapter gave an introduction to techniques of atmospheric remote sensing and especially details on solar occultation, the method of key interest were discussed. In the fourth Chapter a concise description of the SMAS sensor concept, including of the payload of a potential satellite and of the instrument characteristics, was presented. The fifth Chapter gave a detailed description of the end-to-end SMAS data processing system developed and of the error analysis setup. The final Chapter six introduced and discussed retrieval performance analysis results on the ozone and temperature retrieval for the SMAS sensor concept.

The SMAS sensor measures radiation coming from the Sun in the middle ultraviolet wavelength band (185 nm to 250 nm used). The measured normalised intensities at selected wavelengths in the Schumann-Runge bands and Herzberg continuum (molecular oxygen absorption) as well as in the Hartley band (ozone absorption) can be inverted into ozone and temperature profiles by the use of the developed SMAS processing system.

The forward model strongly influences physics-based retrieval algorithms. Therefore a realistic forward model representing the physical state of the atmosphere was designed and implemented, adequately simulating the solar radiation measured by a spaceborne sensor

above the top of the atmosphere. The forward model algorithm needs to be not only accurate but also fast, due to the needed high spectral resolution of the Schumann-Runge wavelength channels. Several forward model approximations were developed and carefully evaluated in the retrieval process. An approximation with piecewise spectral integration, to effectively reduce the number of basic forward model runs, was found the preferable choice. An integral over the line of sight, connecting the Sun with the SMAS instrument, was carried out by considering the absorptive atmospheric constituents (basically ozone and molecular oxygen) as well as including the refractive behaviour of the bulk air.

An optimal estimation approach to solve the inverse problem was used. The input for this were simulated measurements (superposed with noise) and *a priori* (first guess) temperature and density profiles, complimented by statistical models of the uncertainties (error covariance matrices) of the *a priori* and measurement information. The moderately non-linear radiative transfer problem was solved by the use of a Best Linear Unbiased Estimator (BLUE) algorithm, in form of an iterative inversion algorithm employing a Taylor series expansion about the first guess profile, and stopping after minimisation of a cost function. For the SMAS processing system, a number of eight iterations to safely reach convergence was found adequate.

For the SMAS performance analysis, a small set of ten wavelength channels was selected to cover the ozone and molecular oxygen absorption bands for limb transmissions over the entire mesosphere, providing maximum possible information from the measurements. According to the ACLISCOPE satellite mission requirements (the mission concept where SMAS was proposed), the SMAS measurements should provide information on temperature profiles in the mesosphere with an accuracy < 2 K at a vertical resolution of ∼2 km.

The performance analysis for the temperature profile retrieval revealed excellent performance throughout the mesosphere from 50 km up to 100 km. Similarly, the ozone retrieval showed excellent performance in the height range from 50 km to 80-90 km. An error analysis was performed for both, temperature and ozone, from which error statistics were shown for four different months (January, March, July, and October) and three different (low, mid, high) latitudes (Equator, 40 deg north, and 60 deg north). In this analyses, the climatological background model CIRA-86 was used to supply *a priori* temperature and molecular oxygen information. The ozone *a priori* information was derived from AFGL-TR-86 data (FASCODE model).

The performance analysis results for temperature showed that the temperature profiles can be retrieved to < 2 K accuracy at heights from 55 km to 100 km at ∼2 km vertical resolution. The ozone profiles were found to be retrievable to < 5% accuracy at ∼2 km height resolution from 50 km to 80 km and to < 10% accuracy at heights up to 90 km. The performance fulfils the ACLISCOPE satellite mission requirements completely. The adapted measurement error superposed on the simulated transmission data was 0.3% at 10 Hz sampling rate, following the SMAS receiver/detector measurement accuracy specification of the ACLISCOPE satellite mission for standard silicon detector diodes. Comparative simulations were also performed for a 0.1% (instead of 0.3%) measurement error (diamond detector diodes) but already the 0.3% error results were found satisfactory and thus used as baseline assumption.

In summary, the developed SMAS processing system was found capable of robustly producing mesospheric data within the required accuracy, given realistic noise levels on the data. Also, a very important feature is the self-calibrating nature of the SMAS occultation

data, wherefore the retrieved profiles will exhibit very low (if any) residual biases and the effects of instrument degradation over time can be essentially neglected.

The SMAS sensor concept thus bears great capability to monitor mesospheric temperature and ozone and to produce long-term stable data with high vertical resolution and accuracy. This would be a much needed dataset for climate change monitoring and research.

A Inverse Problem Theory

Qualitative Classification of Inverse Problems

Inverse problems are usually solved by maximising a cost function term for the forward model, which provides a linear solution of the problem. Prior information of various kinds has to be considered as well. Generally linear problems provides a cost function which is quadratic in the state vector, so that the equations to be solved are then linear. A non-linear problem shows mostly a non-linear forward model, if the forward model is linear, a prior information constrains the problem and it follows non-linearity. Also any non-Gaussian probability density function (*pdf*) as prior information produces non-linear problems. A qualitative classification about the linearity of inverse problems can be done as follows [*Rodgers* (2000)]:

Linear: if the forward model function is given by $\mathbf{y} = \mathbf{Kx}$ and any *a priori* knowledge is Gaussian.

Nearly linear: non-linear problems, but linearisation about some prior state is possible. These problems are linear to the accuracy of the measurements, or to the required accuracy of the solution within the common range of variation of the state.

Moderately non-linear: these are problems where linearisation is adequate for error analysis, but not for finding a solution.

Grossly non-linear: problems which are non-linear within the range of their errors.

Tab. A.1 gives a short overview about inverse problems and their classifications.

The Bayesian Approach

The Bayesian approach is based directly on Bayes' theorem and is more general than classical estimators. Bayes theorem defines how the measurement *pdf* maps into state space, and combines with prior information. The mechanism for doing this approach requires to assume that the parameter is a random variable with a known prior probability density function. The Bayesian approach is the method to solve by noise perturbed inverse problems. Thereby prior information is quantified as a probability density function over the state space. On the other hand, imperfect measurement can be quantified by a *pdf* over the measurement space according to the forward model $\mathbf{y} = \mathbf{F}(\mathbf{x}) + \epsilon$.

Probability density is a scalar-valued function, for this approach a function of the state vector or measurement vector and can be summarised as follows:

A of full rank rank($\mathbf{A}$) = min(m, n)			**A** is rank deficient rank($\mathbf{A}$) < min(m, n)
m>n rank($\mathbf{A}$) = n	m=n rank($\mathbf{A}$) = $m = n$	m<n rank($\mathbf{A}$) = m	m, n unordered rank($\mathbf{A}$) < min(m, n)
$\mathbf{Ax} = \mathbf{y}$: over-determined	$\mathbf{Ax} = \mathbf{y}$: even-determined	$\mathbf{Ax} = \mathbf{y}$: under-determined	$\mathbf{Ax} = \mathbf{y}$: under- or mixed-determined
$\nexists \mathbf{A}^{-1}$	$\exists \mathbf{A}^{-1}$	$\nexists \mathbf{A}^{-1}$	$\nexists \mathbf{A}^{-1}$
$\mathbf{A}^{-g} = (\mathbf{A}^T\mathbf{A})^{-1}\mathbf{A}^T$	$\mathbf{A}^{-g} = \mathbf{A}^{-1}$	$\mathbf{A}^{-g} = \mathbf{A}^T(\mathbf{A}\mathbf{A}^T)^{-1}$	$\mathbf{A}^{-g} = \mathbf{V}\mathbf{\Lambda}^{-g}\mathbf{U}^T$
$\mathbf{x} = \mathbf{A}^{-g}\mathbf{y}$ least-squares solution	$\mathbf{x} = \mathbf{A}^{-1}\mathbf{y}$ exact solution	$\mathbf{x} = \mathbf{A}^{-g}\mathbf{y}$ min norm solution	$\mathbf{x} = \mathbf{A}^{-g}\mathbf{y}$ least-squares - min norm solution

Table A.1. Short overview about inverse problems and their classifications, where m is the number of measurements in the measurement vector $\mathbf{y}$, n is the number of state elements in the state vector $\mathbf{x}$, $\mathbf{A}^{-g}$ is the generalised inverse, and $\mathbf{A}^{-1}$ and $\mathbf{A}^{-T}$ are the inverse and transpose matrix, respectively (cf., e.g. [*Rodgers* (2000)]).

$P(\mathbf{x})$ can be defined as the prior *pdf* of the state $\mathbf{x}$. $P(\mathbf{x})\,\mathrm{d}\mathbf{x}$ is the probability before the measurement that state $\mathbf{x}$ lies in the multidimensional volume $(\mathbf{x},\, \mathbf{x} + \mathrm{d}\mathbf{x})$. Its normalised and thus applies $\int P(\mathbf{x})\,\mathrm{d}\mathbf{x} = 1$. The $P(\mathbf{x})$ is prior in the sense that it does not take into account any information about $\mathbf{y}$.

$P(\mathbf{y})$ designates the prior *pdf* of the measurement. This is the probability density function before the data have been measured (and acts as a normalising constant).

$P(\mathbf{x}, \mathbf{y})$ can be defined as the joint prior *pdf* of $\mathbf{x}$ and $\mathbf{y}$. This means that $P(\mathbf{x}, \mathbf{y})\,\mathrm{d}\mathbf{x}\,\mathrm{d}\mathbf{y}$ is the probability that $\mathbf{x}$ lies in $(\mathbf{x},\, \mathbf{x} + \mathrm{d}\mathbf{x})$ and $\mathbf{y}$ lies in $(\mathbf{y},\, \mathbf{y} + \mathrm{d}\mathbf{y})$.

$P(\mathbf{y}|\mathbf{x})$ refer to the conditional *pdf* of $\mathbf{y}$ given $\mathbf{x}$. This refers to the uncertainty in the data and means that $P(\mathbf{y}|\mathbf{x})\,\mathrm{d}\mathbf{y}$ is the probability that $\mathbf{y}$ lies in $(\mathbf{y},\, \mathbf{y} + \mathrm{d}\mathbf{y})$ when $\mathbf{x}$ has a given value.

$P(\mathbf{x}|\mathbf{y})$ refers to the *pdf* of $\mathbf{x}$ after the data have been measured. This means that $P(\mathbf{x}|\mathbf{y})\,\mathrm{d}\mathbf{x}$ is the probability that $\mathbf{x}$ lies in $(\mathbf{x},\, \mathbf{x} + \mathrm{d}\mathbf{x})$ when $\mathbf{y}$ has a given value. This is the quantity that is of interest for solving the inverse problem.

In the Bayesian approach, the prior probability density $P(\mathbf{x})$ can be defined by the integral over all values of $\mathbf{y}$, thus follows

$$P(\mathbf{x}) = \int_{-\infty}^{\infty} P(\mathbf{x}, \mathbf{y})\,\mathrm{d}\mathbf{y} \ . \tag{A.1}$$

Likewise $P(\mathbf{y})$ can be found be integrating over all values of $\mathbf{x}$. The conditional *pdf* $P(\mathbf{y}|\mathbf{x})$ is proportional to the values of $P(\mathbf{y}, \mathbf{x})$ as a function of $\mathbf{y}$ for a given value of $\mathbf{x}$. The constant of proportionality prepossess $\int P(\mathbf{y}|\mathbf{x})\,\mathrm{d}\mathbf{y} = 1$ and $P(\mathbf{y}, \mathbf{x})$ can be divided by the integral along the line as

$$P(\mathbf{y}|\mathbf{x}) = \frac{P(\mathbf{x}, \mathbf{y})}{\int P(\mathbf{x}, \mathbf{y})\,\mathrm{d}\mathbf{y}} \ . \tag{A.2}$$

Inserting Eq. A.1 for the integral in the equation above furnish

$$P(\mathbf{y}|\mathbf{x}) = \frac{P(\mathbf{x}, \mathbf{y})}{P(\mathbf{x})} \tag{A.3}$$

and it applies by the use of the same arguments that $P(\mathbf{x}|\mathbf{y}) = P(\mathbf{x}, \mathbf{y})/P(\mathbf{y})$. The elimination of $P(\mathbf{x}, \mathbf{y})$ between the two equations leads to Bayes's theorem as a relation between the two different conditional probability densities and can be written as

$$P(\mathbf{x}|\mathbf{y}) = \frac{P(\mathbf{y}|\mathbf{x})\, P(\mathbf{x})}{P(\mathbf{y})} \quad , \tag{A.4}$$

where $P(\mathbf{x}|\mathbf{y})$ is the posterior *pdf* of the state when the measurement is given. $P(\mathbf{y}|\mathbf{x})$ describes the information of $\mathbf{y}$ that would be obtained if the state were $\mathbf{x}$. To calculate $P(\mathbf{y}|\mathbf{x})$ requires only the knowledge of the forward model and the statistical description of the measurement. The evidence $P(\mathbf{y})$ accords to a scaling constant, independent of $\mathbf{x}$ and is needed to ensure that $P(\mathbf{x}|\mathbf{y})$ integrates to one.

The conceptional approach to solve inverse problems defined by Bayes' theorem can be summarised as:

- Prior information is expressed as probability density function *pdf* and is known before the measuring procedure starts.
- A forward model describes the measurement procedure and maps the state space into the measurement space.
- With Bayes' theorem a formalism exists to invert this mapping and calculate a posterior *pdf* by updating the prior *pdf* with the measurement *pdf*.

A detailed discussion about the Bayesian approach for atmospheric remote sounding can be found in [*Rodgers* (1976), *Rodgers* (1990), *Rodgers* (2000)], which provided the basis for this summary description.

List of Tables

List of Figures

References

[*ACRI S.A. et al.* (1998)] ACRI S.A., et al., GOMOS High Level Algorithms Definition Document, *Tech. Rep.*, ACRI S. A., France, Finnish Meteorol. Institute, Service d'Aronomie du CNRS, and Institut d'Aronomie Spatiale de Bruxelles, 1998, http://envisat.esa.int/support-docs/.

[*Anderson et al.* (1995)] Anderson, G., F. Kneizys, J. Chetwynd, J. Wang, M. Hoke, L. Rothman, L. Kimball, and R. McClatchey, FASCODE/MODTRAN/LOWTRAN: Past/Present/Future, *18th Ann. Rev. Conf. on Atm. Transmission Models*, 1995.

[*Andrews* (2000)] Andrews, D., *An Introduction to Atmospheric Physics*, Cambridge University Press, 2000.

[*Atreya* (1981)] Atreya, S., Measurement of Minor Species (H_2, Cl, O_3, NO) in the Earth's Atmosphere by the Occultation Technique, *Adv. Space Res.*, pp. 127–141, 1981.

[*Atreya et al.* (1984)] Atreya, S., J. H. W. Jr., T. M. Donahue, A. F. Nagy, and J. C. McConnell, *Theory, Measurements, and Models of the Upper Atmosphere and Ionosphere of Saturn*, Univ. of Ariz. Press, Tucson, 1984.

[*Bates and Nicolet* (1950)] Bates, D., and M. Nicolet, Atmospheric Hydrogen, *Publ. Astron. Soc. Pacific*, *62*, 106, 1950.

[*Bertaux et al.* (1986)] Bertaux, J., et al., Atmospheric Ozone: Assemssment of Our Understanding ot the Process Controlling Its Present Distribution and Change, *Tech. Rep.*, NASA, Washington, DC, 1986, rep. 16.

[*Beyerle et al.* (2005)] Beyerle, G., T. Schmidt, G. Michalak, S. Heise, J. Wickert, and C. Reigber, Atmospheric Profiling utilising the Zero Difference Technique, *Geophys. Res. Lett.*, *32*, 13,806, 2005.

[*Bowman and Krueger* (1985)] Bowman, K., and A. Krueger, A Global Climatology of Total Ozone from the Nimbus 7 Total Ozone Mapping Spectrometer, *J. Geophys. Res.*, *90*, 7967, 1985.

[*Brasseur and Solomon* (1984)] Brasseur, G., and S. Solomon, *Aeronomy of the Middle Atmosphere*, D. Reidel Publishing Company, 1984.

[*Brasseur et al.* (1999)] Brasseur, G., J. Orlando, and G. Tyndall (Eds.), *Atmospheric Chemistry and Global Change*, Atmospheric and Space Science Series, Oxford Science Publications, 1999.

[*Bray et al.* (1984)] Bray, R., R. Loughhead, and C. Durrant, *The Solar Granulation*, Cambridge University Press, 1984.

[*Brown and Hwang* (1997)] Brown, R., and P. Hwang (Eds.), *Introduction to Random Signal and Applied Kalman Filtering*, John Wiley and Sons, 1997.

[*Chapman* (1930)] Chapman, S., A Theory of Upper Atmospheric Ozone, *Mem. R. Meteorol. Soc.*, *3*, 103–125, 1930.

[*Cheung et al.* (1986)] Cheung, A., K. Yoshino, W. Parkinson, S. Guberman, and D. Freeman, Absorption Cross Section Measurements of Oxygen in the Wavelegnth Region 195-241 nm of the Herzberg Continuum, *Planet. Space Sci.*, *34*, 1007–1021, 1986.

[*Chu et al.* (1989)] Chu, W. P., M. McCormick, J. Lenoble, C. Brogniez, and P. Pruvost, SAGE II Inversion Algorithm, *J. Geophys. Res.*, *94*, 8339–8351, 1989.

[*CIRA-86* (1990)] CIRA-86, COSPAR International Reference Atmosphere: 1986, *Adv. Space Res.*, *10*, 1990.

[*Coulson* (1975)] Coulson, K., *Solar and Terrestrial Radiation*, Academic Press, Inc, 1975.

[*Council* (1994)] Council, N. R., *Solar Influences on Global Change*, NAP, 1994.

[*Crutzen* (1970)] Crutzen, P., The Influence of Nitrogen Oxides on Atmospheric Ozone Content, *Q. J. R. Meteorol. Soc.*, *96*, 320–325, 1970.

[*D.G. Andrews* (1987)] D.G. Andrews, C. L., J.R. Holton, *Middle Atmosphere Dynamics*, Academic Press, Inc, 1987.

[*Dunkerton* (1978)] Dunkerton, T., On the Mean Meridional Mass Motions of the Stratosphere and Mesosphere, *J. Atmos. Sci.*, *35*, 2325, 1978.

[*Edlen* (1953)] Edlen, B., The Dispersion of Standard Air, *J. Opt. Soc. Am.*, *43*, 339–345, 1953.

[*Elachi* (1987)] Elachi, C., *Introduction to the Physics and Techniques of Remote Sensing*, Wiley Series in Remote Sensing, John Wiley and Sons, 1987.

[*ESA-SP-1196(7)* (1996)] ESA-SP-1196(7), Atmospheric Profiling Mission, *ESA/ESTEC, Noordwijk, The Nederlands*, *7*, 58, 1996.

[*ESA-SP-1227* (1998)] ESA-SP-1227, The Earth Explorer Programme: The Science and research Element of ESA's Future Earth Observation Programme, *ESA/ESTEC, Noordwijk, The Nederlands*, 1998.

[*Farman et al.* (1985)] Farman, J., B. Gardiner, and J. Shanklin, Large Losses of Total Ozone in Antarctica Reveal Seasonal ClO_x/NO_x interaction, *Nature*, *315*, 207, 1985.

[*Farmer* (1987)] Farmer, C., High Resolution IR Spectroscopy of the Sun and the Earth's Atmosphere from Space, *Mikrochim. Acta*, *3*, 189, 1987.

[*Fels et al.* (1980)] Fels, S., J. Mahlman, M. Schwarzkopf, and R. Sinclair, Stratospheric Sensitivity to Pertubations in Ozone and Carbon Dioxide: Radiative and Dynamical Response, *Geophys. Res. Lett.*, *7*, 565, 1980.

[*Fjeldbo et al.* (1971)] Fjeldbo, G., V. Eshleman, and A. Kliore, The Neutral Atmosphere of Venus as Studied with the Mariner V Radio Occultation Experiments, *Astronomical J.*, *76*, 123–140, 1971.

[*Fleming et al.* (1988)] Fleming, E., S. Chandra, M. Schoeberl, and J. Barnett, Monthly-mean Climatology of Temperature, Wind, Geopotential Height, and Pressure for 0-120 km, *Tech. Rep.*, Technical Report NASA TM-100697, Goddard Space Flight Center, Greenbelt, MD, 1988.

[*Frohlich* (1977)] Frohlich, C., Contempoaray Measures of the Solar Constant, in *The Solar Output and Its Variation*, edited by O. White, University of Colorado Press, 1977.

[*Fussen* (1998)] Fussen, D., A Critical Analysis of the Stratospheric Aerosol and Gas Experiment II Spectral Inversion Algorithm, *J. Geophys. Res.*, *103*, 8455, 1998.

[*Fussen et al.* (1998)] Fussen, D., E. Arjis, D. Nevejans, F. van Hellemont, C. Brogniez, and J. Lenoble, Validation of the ORA Spatial Inversion Algorithm with Respect to the Stratospheric Aerosol and Gas Experiment II Data, *App. Opt.*, *37*, 3121, 1998.

[*Gadsen* (1997)] Gadsen, M., The Secular Change in Noctilucent Cloud Occurence: Study of a 31-year Sequence to Clarify the Causes, *Adv. Space Res.*, *20*, 2097–2100, 1997.

[*Gadsen and Schroder* (1989)] Gadsen, M., and W. Schroder, *Noctilucent Clouds*, Springer Verlag, 1989.

[*Geller* (1983)] Geller, M., Dynamics of the Middle Atmosphere, *Space Science Rev.*, *34*, 359, 1983.

[*Gershenfeld* (1999)] Gershenfeld, N., *The Nature of Mathematical Modeling*, Cambridge University Press, 1999.

[*Gobiet and Kirchengast* (2002)] Gobiet, A., and G. Kirchengast, Sensitivity of atmospheric profiles retrieved from GNSS occultation data to ionospheric residual and high-altitude initialization errors, *Tech. Rep.*, ESA/ESTEC No. 1/2002, 2002, IGAM, Univ. of Graz, Austria, 58 pp.

[*Gobiet and Kirchengast* (2004)] Gobiet, A., and G. Kirchengast, Advancements of Global Navigation Satellite System Radio Occultation Retrieval in the Upper Stratosphere for Optimal Climate Monitoring Utility, *J. Geophys. Res.*, *109*, D24,110, 2004.

[*GRAS-SAG* (1998)] GRAS-SAG, The GRAS Instrument on Metop, *Tech. Rep.*, Rep. of the GRAS-SAG, 1998, version 1.2.

[*Hall and Anderson* (1991)] Hall, L., and G. Anderson, High Resolution Solar Spectrum between 200 and 310 nm, *J. Geophys. Res.*, *96*, 12,927–12,931, 1991.

[*Hall et al.* (1985)] Hall, L., L. Heroux, and H. Hinteregger, *Solar Ultraviolet Irradiance Chapter 2*, Air Force Geophysics Laboratory, 1985.

[*Hays and Roble* (1968a)] Hays, P., and R. Roble, Stellar Spectra and Atmospheric Composition, *J. of Atmos. Sci.*, *25*, 1142, 1968a.

[*Hays and Roble* (1968b)] Hays, P., and R. Roble, Atmospheric properties from the inversion of planetary occultation data, *Planetary Space Sci.*, *16*, 1197–1198, 1968b.

[*Hays and Roble* (1973)] Hays, P., and R. Roble, Stellar Occultations of Molecular Oxygen in the Lower Thermosphere, *Planetary Space Sci.*, *21*, 273–279, 1973.

[*Hedin* (1991)] Hedin, A., Extension of the MSIS Thermosphere Model into the Middle and Lower Atmosphere, *J. Geophys. Res.*, *96*, 1159, 1991.

[*Hinteregger* (1962)] Hinteregger, H., Absorption Spectrometric Analysis of the Upper Atmosphere in the EUV Region, *J. Atmos. Sci.*, *19*, 351–368, 1962.

[*Houghton* (1985)] Houghton, H., *Physical Meteorology*, MIT, Cambridge, 1985.

[*Houghton et al.* (1984)] Houghton, J., F. Taylor, and C. Rodgers, *Remote Sounding of Atmospheres*, Cambridge Planetary Science Series, Cambridge University Press, 1984.

[*Houghton et al.* (2001)] Houghton, J., et al. (Eds.), *Climate Change 2001: The Scientific Basis*, Cambridge University Press, 2001, contribution of Working Group I to the Third Assessment Report of the IPCC.

[*Hoyt and Schatten* (1997)] Hoyt, D., and K. Schatten (Eds.), *The Role of the Sun in Climate Change*, Oxford University Press, New York, 1997.

[*Huffmann* (1992)] Huffmann, R., *Atmospheric Ultraviolet Remote Sensing*, Academic Press, Inc, 1992.

[*Johnston* (1971)] Johnston, J., Reduction of stratospheric Ozone by Nitrogen Ozone Catalysts from supersonic Transport Exhaust, *Science*, *173*, 517, 1971.

[*Kiehl and Solomon* (1986)] Kiehl, J., and S. Solomon, On the Radiative Bilance of the Stratosphere, *J. Atmos. Sci.*, *43*, 1525–1534, 1986.

[*Kirchengast* (1998)] Kirchengast, G., End-to-end GNSS Occultation Performance Simulator Overview and Exemplary Applications, *Wiss. Ber. No. 2/1998*, 1998, Institute for Geophysics, Astrophysics and Meteorology, Univ. of Graz, Austria.

[*Kirchengast et al.* (2002)] Kirchengast, G., J. Fritzer, and J. Ramsauer, End-to-end GNSS Occultation Performance Simulator Version 4 (EGOPS4) Software User Manual (Overview and Reference Manual), *Tech. Rep.*, Technical Report ESA/ESTEC-3/2002, University of Graz, Austria, 2002, IGAM, Univ. of Graz, Austria, 472 pp.

[*Kirchengast et al.* (2004)] Kirchengast, G., J. Fritzer, M. Schwaerz, S. Schweiter, and L. Kornblueh, The Atmospheric and Climate Explorer Mission ACE+: Scientific Algorithms and Performance Overview, *Tech. Rep.*, IGAM, 2004.

[*Kirchengast et al.* (1998)] Kirchengast, G., et al., ACLISCOPE-Atmosphere and Climate Sensors Constellation Performance Explorer (ESA Earth Explorer Opportunity mission proposal), *Wiss. Ber. No. 3/1998, 3*, 60, 1998, Institute for Geophysics, Astrophysics and Meteorology, Univ. of Graz, Austria.

[*Kliore et al.* (1965)] Kliore, A., G. Fjeldbo, B. Seidel, D. Sweetnam, T. Sesplaukis, and P. Woiceshyn, Occultation Experiment: Results of the First Direct Measurement of Mars' Atmosphere and Ionosphere, *Science, 149*, 1243–1248, 1965.

[*Kramer* (2002)] Kramer, H., *Observation of the Earth and Its Environment*, Springer Verlag, 2002.

[*Kursinski et al.* (1997)] Kursinski, E., G. Hajj, J. Schofield, R. Linfield, and K. Hardy, Observing the Earth's Atmosphere with Radio Occultation Measurements using GPS, *J. Geophys. Res., 102*, 23,429–23,465, 1997.

[*Lang and Pucker* (1998)] Lang, C., and N. Pucker, *Mathematische Methoden in der Physik*, Spektrum Akademischer Verlag GmbH, 1998.

[*Lean* (1987)] Lean, J., Solar Ultraviolet Irradiance Variations: A Review, *J. Geophys. Res., 92*, 839–868, 1987.

[*Lean* (1991)] Lean, J., Variations in the Sun's Radiative Output, *Rev. Geophys., 29*, 505–535, 1991.

[*Lean et al.* (1982)] Lean, J., O. White, W. Llivingston, D. Heath, R. Donnelly, and A. Skumanisch, A Three-Component Model of the Variability of the Solar Ultraviolet Flux: 145-200 nm, *J. Geophys. Res., 87*, 1037, 1982.

[*Lumpe et al.* (1991)] Lumpe, J., C. Chang, and D. J. Strickland, Atmospheric Constituent Density Profiles from full Disk Solar Occultation Experiments, *Journal of Quantum Spectroscopy Radiative Transfer, 46*, 483–506, 1991.

[*Maybeck* (1979)] Maybeck, P., *Stochastic Models, Estimation and Control, Volume I*, Academic Press, New York, 1979.

[*Maybeck* (1982)] Maybeck, P., *Stochastic Models, Estimation and Control, Volume II*, Academic Press, New York, 1982.

[*McCormick* (1987)] McCormick, M., SAGE II: An Overview, *Adv. Space Res., 7*, (3)219–(3)226, 1987.

[*McCormick et al.* (1979)] McCormick, M., P. Hamill, T. Pepin, W. Chu, T. Swissler, and L. McMaster, Satellite Studies of Stratospheric Aerosol, *Bull. of the Amer. Met. Soc., 60*, 1979.

[*McCormick et al.* (1989)] McCormick, M., J. Zawodny, R. Veiga, J. Larson, and P. Wang, An Overview of SAGE I and II Ozone Measurements, *Planetary Space Sci., 37*, 1567, 1989.

[*McCormick et al.* (1981)] McCormick, M., et al., High-Latitude Stratospheric Aerosol Measuremed by SAM II Satellite System in 1978-1979, *Science*, pp. 328–331, 1981.

[*Melbourne et al.* (1994)] Melbourne, W., E. Davis, C. Duncan, G. Hajj, K. Hary, E. Kursinski, T. Meehan, and L. Young, The Application of Spaceborne GPS to Atmospheric Limb Sounding and Global Change Monitoring, *Tech. Rep.*, Jet Propulsion Laboratory, Pasadena, California, 1994.

[*Minschwaner and Starke* (2000)] Minschwaner, K., and V. Starke, Photodissociation of Nitric Oxide in the Middle and Upper Atmosphere, *Physical Chemistry of Earth Manuscript, Department of Physics, New Mexico Institute of Mining and Technology, Socorro, New Mexico, ST9.2-022*, 22, 2000.

[*Minschwaner et al.* (1992)] Minschwaner, K., G. Anderson, L. Hall, and K. Yoshino, Polynomial Coefficients for Calculations, *J. Geophys. Res.*, *10*, 10,103–10,108, 1992.

[*Mitter* (1993)] Mitter, H., *Quantentheorie*, B.I. Hochschultaschenbuch, 1993.

[*Molina and Molina* (1986)] Molina, L., and M. Molina, Absolute Absorption Cross Section of Ozone on the 185- to 350 nm Wavelength Range, *J. Geophys. Res.*, *91*, 14,501–14,508, 1986.

[*Molina and Rowland* (1974)] Molina, M., and F. Rowland, Stratospheric Sink for Chlorofluoromethanes: Chlorine Atomcatalyzed Destruction of Ozone, *Nature*, *249*, 810–812, 1974.

[*Mursuly and Ulrich* (1998)] Mursuly, K., and T. Ulrich, A new Method to Determine the Solar Cycle Length, *Geophys. Res. Lett.*, *25*, 1837–1840, 1998.

[*Murtagh* (1988)] Murtagh, D., The Schumann-Runge System: New Calculations of Photodissociation Cross Section, *Planet. Space Sci.*, *36*, 819–828, 1988.

[*Neske et al.* (1997)] Neske, E., E. Schmidtke, and H. Wolf, Development of high sensitivity EUV silicon diodes, *Report FIPM Freiburg, Germany*, 1997.

[*Nicolet and Peetermans* (1980)] Nicolet, M., and W. Peetermans, Atmospheric Absorption in the O_2 S-R Band Spectral Range and Photodissociation Rates in the Stratosphere and Mesosphere, *Planet. Space Sci.*, *36*, 85–103, 1980.

[*Nicolet et al.* (1988a)] Nicolet, M., S. Cieslik, and R. Kennes, Aeronomic Problems of O_2 Photodissociation-IV. The Various Parameters for the Herzberg Continuum, *Planet. Space Sci.*, *36*, 1069–1076, 1988a.

[*Nicolet et al.* (1988b)] Nicolet, M., S. Cieslik, and R. Kennes, Aeronomic Problems of O_2 Photodissociation-II. Theoretical Absorption Cross Sections of the S-R Bands at 79 K, *Planet. Space Sci.*, *36*, 1039–1058, 1988b.

[*Nicolet et al.* (1989)] Nicolet, M., S. Cieslik, and R. Kennes, Aeronomic Problems of O_2 Photo Dissociation- V. Predissociation in the S-R Bands of Oxygen, *Planet. Space Sci.*, *37*, 427 – 458, 1989.

[*Oceanic et al.* (1976)] Oceanic, N., N. A. Atmospheric Administration, and U. G. P. O. Space Administration, U.S. Airforce, *U.S Standard Atmosphere*, NOAA, Washington D.C., 1976.

[*Peixoto and Ooort* (1992)] Peixoto, J., and A. Ooort, *Physics of Climate*, American Institute of Physics, 1992.

[*Pepin and McCormick* (1976)] Pepin, T., and M. McCormick, Stratospheric Aerosol Measurement Experiment MA-007, *Tech. Rep.*, NASA TM X-58173, 1976.

[*Pollack and McKay* (1985)] Pollack, J., and C. McKay, The Impact of Polar Stratospheric Clouds on the Heating Rates of the Winter Polar Stratosphere, *J. Atmos. Sci.*, *42*, 245–262, 1985.

[*Press* (1993)] Press, C., *Handbook of Chemistry and Physics*, vol. 74, CRC press, 1993.

[*Rees* (2001)] Rees, W., *Physical Principles of Remote Sensing*, Cambridge University Press, 2001.

[*Rehrl* (2000)] Rehrl, C., Mesospheric Temperature and Ozone Sounding Based on Solar Occultation Data, Master's thesis, IGAM, Univ. of Graz, Austria, 2000.

[*Rehrl and Kirchengast* (2004)] Rehrl, C., and G. Kirchengast, Mesospheric Temperature and Ozone Sounding by the SMAS Solar Occultation Sensor, in *Occultations for Probing Atmosphere and Climate*, edited by G. Kirchengast, U. Foelsche, and A. Steiner, pp. 333 – 342, Springer Verlag, 2004.

[*Retscher* (2004)] Retscher, C., Stratospheric Ozone and Temperature Sounding by the Envisat/GOMOS Stellar Occultation Sensor, (Ph.D. thesis), *Wiss. Ber. No. 23/2004*, 2004, IGAM, Univ. of Graz, Austria.

[*Retscher et al.* (2004a)] Retscher, C., G. Kirchengast, A. Gobiet, and A. Hauchecorne, Stratospheric Temperature and Ozone Sounding with Envisat/GOMOS Stellar Occultation, in *Occultations for Probing Atmosphere and Climate*, edited by G. Kirchengast, U. Foelsche, and A. Steiner, pp. 299 – 308, Springer Verlag, 2004a.

[*Retscher et al.* (2004b)] Retscher, C., C. Rehrl, A. Gobiet, and G. Kirchengast, Stellar Occultation Algorithm and Validation for GOMOS on Envisat and a Performance Analysis for the Complementary Solar Occultation Concept SMAS, *Tech. Rep.*, Wiss. Ber. No. 2/2004, IGAM, Univ. of Graz, Austria, 2004b.

[*Rieder and Kirchengast* (2001a)] Rieder, M., and G. Kirchengast, Error Analysis for Mesospheric Temperature Profiling by Absorptive Occultation Sensors, *Ann. Geophys.*, *19*, 71–81, 2001a.

[*Rieder and Kirchengast* (2001b)] Rieder, M., and G. Kirchengast, Error Analysis and Characterization of Atmospheric Profiles Retrieved from GNSS Occultation Data, *J. Geophys. Res.*, pp. 31,755–31,770, 2001b.

[*Risbeth and Garriott* (1969)] Risbeth, H., and O. Garriott, *Indroduction to Ionospheric Physics*, Academic Press, Inc, 1969.

[*Roble and Hays* (1972)] Roble, R., and P. Hays, A Technique for Recovering the Vertical Number Density Profile of Atmospheric Gases from Planetary Occultation Data, *Planet. Space Sci.*, *20*, 1727–1744, 1972.

[*Roble and Norton* (1972)] Roble, R., and R. Norton, Thermospheric Molecular Oxygen from Solar EUV Occultation Measurements., *J. Geophys. Res.*, *77*, 3524, 1972.

[*Rodgers* (1976)] Rodgers, C., Retrieval of Atmospheric Temperature and Composition from Remote Measurements of Thermal Radiation, *Rev. Geophys.*, *14*, 609–624, 1976.

[*Rodgers* (1990)] Rodgers, C., Characterization and Error Analysis of Profiles Retrieved From Remote Sensing Measurements, *J. Geophys. Res.*, *95*, 5587–5595, 1990.

[*Rodgers* (2000)] Rodgers, C., *Inverse Methods for Atmospheric Remote Sounding: Theory and Practice*, World Scientific, Singapore, 2000.

[*Roeckner et al.* (2004)] Roeckner, E., et al., The Atmospheric General Circulation Model ECHAM5, *Tech. Rep.*, MPIM Hamburg, 2004.

[*Roscoe et al.* (1994)] Roscoe, H., et al., Using Stars for Remote Sensing of the Earth's Stratosphere, *App. Opt.*, *33*, 7126–7131, 1994.

[*Rottman* (1990)] Rottman, G., Recent Advances in VUV Observations of the Sun, *Physica Scripta*, *T31*, 199–207, 1990.

[*Rowland and Molina* (1975)] Rowland, F., and M. Molina, Chlorofluoromethanes in the Environment, *Rev. Geophys.*, *13*, 1–35, 1975.

[*Russel et al.* (1993)] Russel, J., et al., The Halogen Occultation Experiment, *J. Geophys. Res.*, *98*, 10,777, 1993.

[*Russell et al.* (1995)] Russell, G., J. Miller, and D. Rind, A Coupled Atmosphere-Ocean Model for Transient Climate Change Studies, *Atmos.-Ocean*, *33*, 683–730, 1995.

[*Salby* (1995)] Salby, M., *Fundamentals of Atmospheric Physics*, Academic Press, Inc, 1995.

[*Schmidtke et al.* (1991)] Schmidtke, G., H. Doll, C. Wita, and S. Chakrabarti, Solar Euv/UV and Equatorial Airglow Measurements from San Marco-5 , *J. Atm. Terr. Phys.*, *53*, 781–785, 1991.

[*Schmidtke et al.* (2000)] Schmidtke, G., F. Wienhold, J. Anders, B. Galuska, U. Klocke, M. Knothe, and W. Riedel, The Solar Package on ISS: SOL-ACES, *Phys. Chem. of Earth*, *25*, 473–476, 2000.

[*Schwärz* (2004)] Schwärz, M., Joint Temperature, Humidity, Ozone, and Sea Surface Temperature Retrieval from Infrared Atmospheric Sounding Interferometer Data, Ph.D. thesis, IGAM, Univ. of Graz, Austria, 2004.

[*Seinfeld and Pandis* (1998)] Seinfeld, J., and S. Pandis, *Atmospheric Chemistry and Physics*, Wiley-Interscience, 1998.

[*Smith and Hunten* (1990)] Smith, G., and D. Hunten, Study of Planetary Atmospheres by Absorptive Occultations, *Rev. Geophys.*, *28*, 117–143, 1990.

[*Steiner et al.* (1999)] Steiner, A., G. Kirchengast, and H. Ladreiter, Inversion, error analysis, and validation of GPS/MET occultation data, *Ann. Geophys.*, *17*, 122–138, 1999.

[*Stix* (1989)] Stix, M., *The Sun, An Indroduction*, Springer Verlag, 1989.

[*Storch and Zwiers* (1999)] Storch, H., and F. Zwiers, *Statistical Analysis in Climate Research*, Cambridge University Press, 1999.

[*Syndergaard* (1999)] Syndergaard, S., Retrieval Analysis and Methodologies in Atmospheric Limb Sounding Using GNSS Radio Occultation Technique, Ph.D. thesis, Niels Bohr Institute for Astronomy, Physics and Geophysics, University of Copenhagen, 1999.

[*Tarayre and Massonnet* (1996)] Tarayre, H., and D. Massonnet, Atmospheric Propagation Heterogeneities revealed by ERS-1, *Geophys. Res. Lett.*, *9*, 989–992, 1996.

[*Thomas* (1984)] Thomas, G., Solar Mesospheric Explorer Measurements of Polar Mesospheric Clouds, *J. Atm. Terr. Phys.*, *46*, 819, 1984.

[*Thomas* (1991)] Thomas, G., Mesospheric Clouds and the Physics of the Mesopause Region, *Rev. Geophys.*, *29*, 553–575, 1991.

[*Thomas and Stamnes* (1999)] Thomas, G., and K. Stamnes (Eds.), *Radiative Transfer in the Atmosphere and Ocean*, Atmospheric and Space Science Series, Cambridge University Press, 1999.

[*TR8350* (2002)] TR8350, N. T. R., Department of Defense World Geodetic System 1984, Its Definition and Relationships With Local Geodetic Systems, *Tech. Rep.*, National Geospatial-Intelligence Agency, 2002.

[*Trakhovsky et al.* (1989a)] Trakhovsky, E., A. Ben-Shalom, U. Oppenheim, A. Devir, L. Balfour, and M. Engel, Contribution of Oxygen to Attenuation in the Solar Blind UV Spectral Region, *Appl. Opt.*, *28*, 1588–1591, 1989a.

[*Trakhovsky et al.* (1989b)] Trakhovsky, E., A. Ben-Shalom, and A. Devir, Measurements of Tropospheric Attenuation in the Solar Blind UV Spectral Region and Comparison with LOWTRAN 7 Code, *SPIE*, *1158*, 357–365, 1989b.

[*Wallace and Hobbs* (1977)] Wallace, J., and P. Hobbs, *Atmospheric Science: An Introductory Survey*, Academic Press, Inc, 1977.

[*Wang et al.* (1992)] Wang, P.-H., M. McCormick, W. Chu, J. Lenoble, R. Nagatani, M. Chanin, R. Barnes, F. Schmidlin, and M. Rowland, SAGE II Stratospheric Density and Temperature Retrieval Experiment, *J. Geophys. Res.*, *97*, 843–863, 1992.

[*Ward and Herman* (1998)] Ward, D., and B. Herman, Refractive Sounding by Use of Satellite Solar Occultation Measurements Including an Assessment of its Usefulness to the SAGE Program, *App. Opt.*, *37*, 1998.

[*Weisz* (2001)] Weisz, E., Temperature Profiling by the Infrared Atmospheric Sounding Interferometer (IASI): Advanced Retrieval Algorithm and Performance Analysis, *Wiss. Ber. No. 2/2001*, 2001, IGAM, Univ. of Graz, Austria.

[*White* (1970)] White, O., *The Solar Output and Its Variation*, Colorado Associated University Press, 1970.

[*Wickert et al.* (2005a)] Wickert, J., G. Beyerle, R. Knig, S. Heise, L. Grunwaldt, G. Michalak, C. Reigber, and T. Schmidt, GPS Radio Occultation with CHAMP and GRACE: A First Look at a New and Promising Satellite Configuration Global Atmospheric Sounding, *Ann. Geophys.*, *23*, 653–658, 2005a.

[*Wickert et al.* (2005b)] Wickert, J., T. Schmidt, G. Beyerle, S. Heise, and C. Reigber, Global Atmospheric Sounding with GPS Radio Occultation aboard CHAMP, in *Observation of the Earth System from Space*, edited by J. Flury, R. Rummel, C. Reigber, M. Rothacher, G. Boedecker, and U. Schreiber, pp. 55–67, SP, 2005b.

[*Yoshino et al.* (1988)] Yoshino, K., A. Cheung, J. Resmond, W. Parkinson, D. Freeman, and S. Guberman, Improved Absorption Cross Section of O_2 in the Wavelength Region 205-240 nm of the Herzberg Continuum, *Planet. Space Sci.*, *36*, 1469–1475, 1988.

[*Yoshino et al.* (1992)] Yoshino, K., J. Resmond, A. Cheung, D. Freeman, and W. Parkinson, High Resolution Absorption Cross Sections in the Transmission Window Region of the S-R Bands and Herzberg Continuum of Molecular Oxygen, *Planet. Space Sci.*, *40*, 185–192, 1992.

Abstract:

This study develops and demonstrates the performance of a realistic forward model and retrieval algorithm for ozone and temperature sounding by the Sun Monitor and Atmospheric Sounder (SMAS) instrument. The SMAS sensor concept employs the solar occultation technique and is primarily aiming at mesospheric profiles. The SMAS sensor provides self calibrating normalised intensity data. This work focused on occultation data between 185 nm and 250 nm to compute transmission data for an ozone and temperature retrieval algorithm in the mesosphere. A processing system is presented and used to calculate atmospheric profiles from the solar radiation. This includes a mathematical description of the measurement as well as the retrieval. The retrieval was performed with an optimal estimation technique by incorporation of *a priori* (first guess) data. The moderately non-linear radiative transfer problem was solved by a Best Linear Unbiased Estimator (BLUE) algorithm. An end-to-end retrieval performance analysis was carried out for the developed retrieval processing system, which was found to yield mesospheric temperature and ozone profiles with <2 K and <5% accuracy, respectively, at ~2 km vertical resolution. These very encouraging results for mesospheric temperature and ozone sounding fulfil the target requirements laid out for the SMAS occultation sensor concept. They promise a new quality level of much needed global atmospheric profiling of the mesosphere in the context of climate change monitoring and research.

Zum Inhalt:

In dieser Arbeit werden ein realistisches Vorwärtsmodell und ein dazugehöriger Retrieval-Algorithmus für Temperatur- und Ozonbestimmung mit Hilfe eines sogenannten Sun Monitor and Atmospheric Sounder (SMAS) Instrumentes vorgestellt. Das SMAS Sensor Konzept verwendet die Sonnenokkultationsmethode und erzeugt primär Dichte- und Temperaturprofile im Höhenbereich der Mesosphäre. Der SMAS Sensor liefert selbst-kalibrierte normierte Intensitätsdaten. Für das Ozon- und Temperatur-Retrieval werden in dieser Arbeit primär Intensitätsdaten im Wellenlängenbereich zwischen 185 nm und 250 nm verwendet. Ein zugehöriges Datenverarbeitungssystem zur Berechnung der gewünschten atmosphärischen Dichte- und Temperaturprofile aus diesen solaren Intensitätsdaten wird vorgestellt. Das bedeutet eine mathematische Beschreibung des Messvorganges und Retrievals. Das Retrieval basiert auf der sogenannten "optimal estimation" Methode. Die Input-Daten zur Erzeugung dieser simulierten Messwerte (überlagert mit realistischen Messfehlern) sind sogenannte a priori (geschätzte) Temperatur- und Dichteprofile. Das resultierende moderat nicht lineare Strahlungstransferproblem wurde mit Hilfe eines Best Linear Unbiased Estimator (BLUE) iterativen Inversions-Algorithmus gelöst. Eine End-to-End Retrieval Analyse wurde durchgeführt, welche Temperatur- und Ozonprofile mit einer Genauigkeit <2 K beziehungsweise <5% bei einer vertikalen Höhenauflösung von ~2 km lieferte. Diese sehr ermutigenden Ergebnisse erfüllen zur Gänze die an das SMAS Sensor Konzept gestellten Anforderungen und versprechen eine neue Qualität an globalen mesosphärischen Daten zur Beobachtung und Erforschung von Klimaänderungen.